Structural health monitoring by Fiber Optic Polarimetric sensors (FOPS) and Fiber Bragg Grating (FBG)

Maheshwari, Muneesh

2016

Maheshwari, M. (2016). Structural health monitoring by Fiber Optic Polarimetric sensors (FOPS) and Fiber Bragg Grating (FBG). Doctoral thesis, Nanyang Technological University, Singapore.

https://hdl.handle.net/10356/68018

https://doi.org/10.32657/10356/68018

STRUCTURAL HEALTH MONITORING BY FIBER OPTIC POLARIMETRIC SENSORS (FOPS) AND FIBER BRAGG GRATING (FBG)

MUNEESH MAHESHWARI

SCHOOL OF MECHANICAL AND AEROSPACE ENGINEERING

2016

STRUCTURAL HEALTH MONITORING BY FIBER OPTIC POLARIMETRIC SENSORS (FOPS) AND FIBER BRAGG GRATING (FBG)

Submitted by

MUNEESH MAHESHWARI

Under the supervision of

PROF. ANAND KRISHNA ASUNDI

PROF. SWEE CHUAN TJIN

A thesis submitted to the Nanyang Technological University
in fulfillment of the requirement for the degree of
Doctor of Philosophy

SCHOOL OF MECHANICAL AND AEROSPACE ENGINEERING

2016

Acknowledgement

I would like to express my deepest gratitude to my supervisor Prof. Anand Krishna Asundi. I thank him for evoking confidence in me which helped to do research in a graceful manner. I sincerely appreciate him for being encouraging and patient with me. His constructive suggestions helped me take decisions in the right direction. His expertise and ideas inspired me to put my best in research. I cannot thank him enough for letting me work under his supervision.

I am fortunate to have Prof. Swee Chuan Tjin as my co- supervisor. His guidance and unbeatable support has been of great importance during my research. His knowledge in the field helped me get better and brighter results every time. His ideas bring freshness to research. It was such a pleasure working with him. I feel blessed to be a part of his research group. I would like to extend my sincere gratitude to Assoc. Prof. Murukeshan for his help and support. He was always there whenever I needed him.

I am thankful and acknowledge the technicians of Mechanics and Materials lab, Mr. Koh and Mr. Tan for their help and support. I would like to thank my seniors, Dr. Kapil Dev and Dr. Ravi Kumar for helping me out whenever required. Also, I would like to thank my friends and batchmates Dhiman, Neha, Moumita, Nishtha, Anant, Achyut, and Ratheesh for being there for me in my ups and downs. I am immensely grateful to my parents, lovely sister, and beloved wife for being a constant source of inspiration.

Special thanks to the Optics and Photonics Society of Singapore (OPSS), the international society for optics and photonics (SPIE), and School of Mechanical and Aerospace Engineering (MAE) of Nanyang Technological University (NTU) for their financial support which helped me attend some of very important conferences.

Last but not the least; I would like to express my sincere gratitude to God for giving me an opportunity to work in this beautiful atmosphere of NTU and contribute to science and technology.

Table of Contents

Abstract

Structural health monitoring (SHM) techniques using smart materials are on the rise to meet the ever ending demand due to increased construction and manufacturing activities worldwide. The civil-structural components such as slabs, beams and columns and aero-components such as wings are constantly subjected to some or the other forms of external loading. SHM is one of the most important issues as it prevents overloading, serious damages, also averts risks. A number of methods utilizing different concepts and techniques have already been proposed, but online structural health monitoring is very difficult and ineffective with classical method. The Fiber Optic Sensor (FOS) technologies facilitate real time non-destructive health monitoring of different mechanical and civil structures. These FOS techniques play a very important role in assessing the performance of different engineering structures when they are in operation. The most widely investigated and implemented fiber optic sensors for SHM are Fiber Bragg grating (FBG) and Fiber Optic Polarimetric sensor (FOPS). If the light from a broadband source is launched into the FBG, a very sharp wavelength peak (FWHM ≈ 0.1-0.2 nm) will be reflected back by the FBG or in other words an FBG works as a wavelength filter. This reflected peak shifts if strain, temperature, pressure etc. changes in the FBG. The measurement done by the FBG is very accurate, but it can be used for point measurement only. Thus FBG can monitor local region of the structure. Moreover, the interrogation system of FBG is too bulky and expensive to be used for field applications. In FOPS, polarization maintaining (PM) fiber or high birefringent fiber (Hi-Bi) is used as a sensor. The polarization or the phase of light coming out of FOPS changes if external load or pressure is applied to FOPS. Since the entire FOPS sensor is sensitive, the external perturbations cause a lot of noise in the output signal. Demodulation of the change in the polarization of the light coming out of FOPS signifies the changes in the entire structure with no knowledge of specific location. Therefore, FOPS provides information for global SHM. Location of loading point or damage in the structure is unknown at best in the previous studies. The objective of this research work is to do a combine local and global SHM to find out the location of damage using minimum instrumentation.

FBGs have been used to measure load, pressure, temperature etc. FBG can be designed to measure liquid pressures also as shown in the work. Resin pressure distribution of a curing laminate is a key parameter that controls the strength, stiffness and void nucleation of the cured part. It is vital to monitor and control the resin movement of the curing laminate to optimize its quality with any manufacturing process. In this research work, a device consisting of a fiber Bragg grating (FBG) is designed which is capable of measuring in-situ resin pressure. This device uses the principle of differential pressure in liquids. This stable and reliable sensor is quite useful especially for high temperature and low or zero bleed curing of composite laminates, such as out of autoclave curing. In other words, the SHM of curing composites can be performed using FBG sensors proposed in this work.

The Fiber Optic Polarimetric Sensor (FOPS) is nothing but a polarization maintaining (PM) fiber which is capable of monitoring damage in structures at global level. However the system is not capable of identifying damage location and crack size, which would further assist in the assessment of the severity of damage. Also, the output signal from FOPS is very noisy because of the fact that the whole fiber is sensitive and picks up unwanted signals from its surroundings. In this research work, a new design of FOPS has been put forward. The output of this design is very stable as only a specific part of FOPS is sensitive. This reduces noise and only the part being monitored can be independently assessed. Theoretical validation of this design is presented. This design is then implemented to locate and estimate the size of a crack in a cantilever thus providing local SHM as well. Damage investigation in a fixed-fixed beam has also been done using this FOPS design.

Further, in this research work, it is shown that an FBG written on the Polarization Maintaining (PM) fiber can be used for both global and local SHM simultaneously. Thus, local and global information both are obtained from a single fiber. This reduces costs and complexities. Two PM-FBGs have been multiplexed in a certain way to form a new design of sensor which gives improved information on damaged location in beam structures. Further, by proper multiplexing the PM-FBGs it is possible to predict the damage location in two dimensional structures like, plates too. The damage site in an aluminum plate has been located using this multiplexed sensing array.

FBG can monitor the local region surrounding itself using optical spectrum analyzer (OSA), thus providing local SHM only. In this research work, a wavelength shifted chirped FBG (CFBG) interrogation system has been presented. This is an intensity based interrogation system which can measure positive/negative strain and temperature simultaneously. This sensor design abrogates the need for OSA. It also allows the use of simple LEDs as light source. Altogether, this design substantially brings down the cost of interrogation system. This interrogation design is simple and compact with a strain sensitivity of around $5\mu\varepsilon$. Additionally, since this system is intensity based, it can measure the frequencies of fundamental vibrations of any structure which provide the global SHM of the structure. Thus, this system can perform local and global SHM.

List of Figures

List of Tables

List of Symbols

ϕ	Phase difference between fast and slow polarization modes
$\Delta\beta$	Difference in propagation constant between fast and slow modes
l	Length of polarization maintaining (PM) fiber
l_b	Beat length of PM fiber
Λ	Grating period of FBG
f_n	Frequency of nth fundamental mode
EI	Stiffness of the structure
R	Radius of curvature
M	Bending moment
ε	Strain
c	Distance of the outermost fiber from the neutral axis
Λ_ε	FOPS strain sensitivity
Λ_p	FOPS load sensitivity
ω_n	Angular frequency of nth fundamental mode
λ_B	Bragg wavelength
$\lambda_{B,f}$	Bragg wavelength of fast mode
$\lambda_{B,s}$	Bragg wavelength of slow mode
n_{eff}	Effective refractive index
n_1	Refractive index along the fast axis
n_2	Refractive index along the slow axis
θ	Angle of polarization
M	Mueller matrix
S	Stokes vector

I_f	Intensity of fast mode of polarization
I_s	Intensity of slow mode of polarization
ε_c	Axial strain
d	Cavity length between the two mirrors
λ	Wavelength
m	Number of fringes
α	Wavelength-strain sensitive factor
β	Wavelength-temperature sensitive factor
S	State of polarization
D_1, D_2	Voltages from diodes
n	Number of mode of vibration
L	Length of cantilever
h	Height of cantilever
a	Size of the crack
h	Height of the cantilever
K	Spring stiffness
p_ε	Strain optic coefficient
p_e	Photo elastic constant of fiber
α_s	Coefficient of thermal expansion of silica fiber
ξ	Thermo-optic co-efficient
θ	Polarization angle
P	Load
I	Light intensity
ΔT	Change in temperature
P_l	Liquid pressure

A_f	Cross sectional area of fiber
A_r	Cross sectional area of silicon rubber
E	Elastic coefficient
ρ_l	Liquid density
g	Gravitational constant
H	Height of water column
L_f	Length of fiber
L_r	Length of rubber
PZT	Piezoelectric transducer

List of Acronyms

CFBG	Chirped fiber Bragg grating
CFRP	Carbon Fiber Reinforced Plastic
DDF	Dynamic damage factor
EFPI	Extrinsic Fabry–Perot interferometer
FBG	Fiber Bragg grating
FDM	Frequency-division multiplexing
FFPI	Fiber optic Fabry-Perot interferometer
FOCS	Fiber Optic Curvature Sensor
FOPS	Fiber optic polarimetric sensor
FOS	Fiber optic sensors
FP	Fabry–Perot
Hi-Bi	High birefringent
LPG	Long period grating
MMF	Multimode fiber
OSA	Optical Spectrum analyzer
OTDR	Optical Time Domain Reflectometry
PBS	Polarizing beam splitter
PM	Polarization Maintaining
PM-FBG	Fiber Bragg grating on PM fiber
PMMA	Poly methyl methacrylate
SDF	Static damage factor
SDM	Spatial-division multiplexing
SHM	Structural health monitoring

SMF	Single mode fiber
SOP	State of polarization
TDM	Time-division multiplexing
WDM	Wavelength-division multiplexing

CHAPTER – 1 Introduction

1.1 Theoretical background

Structural health monitoring (SHM) means to have a check on the health of engineering structures so that the risk of catastrophic failure of those structures might be avoided. SHM of mechanical and civil structures like, buildings, bridges, aircrafts, blades of wind turbines etc. has always been a topic of discussion in research. Different smart materials are being used to perform SHM of these structures. Smart materials are the latest generation elements surpassing the capabilities of traditional structural and functional materials which can achieve an effective alternate to traditional SHM techniques [1]. Smart materials can be categorized as active or passive. Active smart materials are those materials which possess the capacity to modify their geometrical or material properties under the application of light, heat, electric or magnetic field, thereby acquiring an inherent capacity to transduce energy whether they are attached to host structure or not [2, 3]. Piezoelectric sensors, acoustic emission, ultrasonic etc. are active smart materials as they actuate and also sense the reactions [4-14]. These techniques are efficient, but real time monitoring is not possible with them. On the other hand smart, but passive materials, like fiber optic sensors (FOS) can only sense the reactions on the structure without having the ability to actuate [15-20]. Some FOS techniques facilitate global health monitoring of structures and some provide the local health monitoring aspects.

1.2 Fiber Optic Sensors (FOS) in structural health monitoring

Fiber Optic Sensors have been very popular and advantageous for health monitoring purposes. These sensors are based on different phenomena which involve changes in intensity, polarization, wavelength or the phase of light. The FOS facilitate with real time non-destructive health monitoring of different Engineering structures. FOS have significant advantages over the conventional sensors. These include immunity to electromagnetic interference, electrically passive, long term stability, light weight, multiplexing capabilities, ease of installation and durability. Also, these sensors have very small diameter, so they can be easily embedded into any mechanical structure

like, aircraft wings, blades of wind turbines, composite structures etc. without disturbing their structural integrity. Also, it can be operated at a temperature as high as 900°C or at as low as 4K. Some of the fiber optic sensors are; Extrinsic Fabry-Perot interferometric (EFPI) sensors [21-23], Fiber optic polarimetric sensors (FOPS) [24-26], Fiber optic curvature sensors (FOCS) [27-30], Fiber Bragg grating (FBG) [31-34] etc. In this project, the capabilities of FOPS and FBG for SHM have been discussed. FOPS provides with global SHM while FBG is known for local SHM. It has also been explored that how a single fiber can discern information from FOPS and FBG both, using only one decoding system to get a complete picture (global + local) of damage scenario.

1.2.1 Fiber Optic Polarimetric Sensors (FOPS)

Polarization maintaining (PM) fibers like, bow-tie fiber of panda fiber are employed as a main sensing component in FOPS. These PM fibers have fixed fast and slow axes throughout its length. Therefore, the light coming out of these PM fibers has fixed state of polarization, but when an external force or disturbance is applied to the fiber, the length/geometry of the core of the fiber changes, as a result the polarization of the light coming out of the fiber changes [24, 35].

Polarized light always has two modes of polarization. In normal medium both the modes travel with the same velocity, therefore, there is no phase difference between both the modes of polarization. But in a birefringent medium (the core of polarization maintaining fiber), one mode (having the direction of polarization along the fast axis) moves faster than the other mode (having the direction of polarization along the slow axis). This difference in velocities introduces an additional phase between fast and slow polarization modes. In case of PM fiber, this additional phase is given by [36]:

$$\phi = \Delta\beta l \tag{1.1}$$

where l is the length of the PM fiber and $\Delta\beta$ $(= \beta_{fast} - \beta_{slow})$ is the difference in propagation constant between fast and slow modes. It is called the birefringence of the PM fiber. Hence clearly, there are two factors which can cause changes in the additional phase ϕ; one is the length of the fiber and another is birefringence ($\Delta\beta$). In FOPS, the change in the additional phase ϕ is due to change in the length or in other

words, it is due to the longitudinal strain which is produced due to the external load/disturbance in the core of the PM fiber.

FOPS can perform global SHM in two ways; one by static loading test and second by dynamic test of the structure under consideration [35, 36]. In static test, the strain in increased in the structure in steps by loading the structure continuously. The phase ϕ changes sinusoidally with increasing strain/load [36]. In case of any damage in the structure, the period of the sinusoidal phase cycle reduces. This is because the strain increases faster with the identical loads due to the presence of the damage in the structure.

In dynamic test, the structures are made to vibrate with their fundamental frequencies. Therefore, the phase of the light coming out of FOPS changes with the same frequencies and these frequencies are captured using oscilloscope. The natural frequencies of any structure depend on the stiffness of that particular structure and are given by:

$$\omega_n \propto \sqrt{EI} \qquad (1.2)$$

where EI is the stiffness of the structure. If there is any damage in the structure, its stiffness reduces and therefore its natural frequencies decrease.

Usually in static loading test, the PM fiber is bonded to the entire structure; therefore, the change in the phase is a result of longitudinal strain produced in the entire structure. Similarly, in dynamic test, the fundamental frequencies are the properties of the entire structure. Therefore, as of now, FOPS is capable of global SHM only.

1.2.2 Fiber Bragg Grating (FBG) Sensors

In FBG sensors, grating (periodic refractive index profile) is inscribed into the core of the fiber as shown in the Figure 1.1. An Excimer laser (248 nm) and phase masks are used to inscribe the grating. When light passes through a grating, a particular wavelength of light is reflected back. This wavelength depends on the distance between the consecutive grooves of the grating (grating period) and is called Bragg wavelength. The Bragg wavelength changes as the distance between the consecutive grooves changes [31, 37].
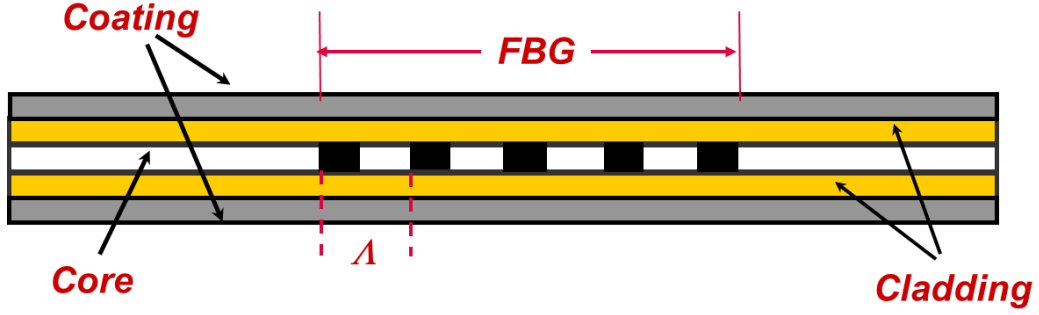
Figure 1.1: Refractive index profile of an FBG.

Bragg wavelength reflected back by FBG is given as:

$$\lambda_B = 2n_{eff}\Lambda \qquad (1.3)$$

where n_{eff} is the effective refractive index of the core of the fiber and Λ is the grating period of the FBG. The strain in terms of change in the Bragg wavelength is given by:

$$\varepsilon = \frac{\Delta\lambda_B}{\alpha} \qquad (1.4)$$

where $\Delta\lambda_B$ is the change in the Bragg wavelength and α is the wavelength-strain sensitive factor. In case of damage near the FBG, the strain increases in the region close to FBG and hence, the Bragg wavelength increases. Since FBG can monitor strain in the nearby region, it is suitable for local SHM only.

1.3 Objective and scope

The objective of this project is to stabilize the output signal of FOPS to get improved information on damage size and location in structures and also, to get combined information on global & local SHM of different structures with minimum optics and instrumentation.

To achieve the objective mentioned above, the following research scopes are presented in my study,

- To explore the scope of FBG for its highly accurate point measurement ability. It would be useful in places where monitoring at some crucial points is required.

- To immunize FOPS from unwanted external disturbances to get a very stable output signal. Although FOPS was qualitatively, a quantitative study for damage size and location is absolutely necessary.

- Although FOPS and FBG can perform global and local SHM independently, integration of FBG & FOPS both on a single fiber would make the sensing system compact and cost effective. It would be of great interest to explore this integrated FBG & FOPS system for complete (local + global) SHM of 1-D and 2-D structures.

- As of now, optical spectrum analyzer (OSA) which is a wavelength based system is used as an FBG interrogation system. There is a need for compact, robust and cost effective FBG interrogation system for field applications. An intensity based FBG interrogation system might provide the additional FOPS action. Thus, complete (local + global) SHM could be performed with a single and cost effective system.

1.4 Organization of report

The work presented in this thesis focuses on structural health monitoring (SHM) of different engineering structures using fiber optic polarimetric sensors (FOPS) and fiber Bragg grating (FBG) sensors. The main emphasis of this report is on how to get maximum information using these two fiber optic sensors to define the damage state in a structure with minimum instrumentation employed. The report is organized in 8 chapters as follows

Following a brief introduction of structural health monitoring (SHM) and fiber optic sensors, chapter 2 presents different techniques available for SHM of different structures. Chapter 2 also articulates how fiber optic sensors are better than other contemporary SHM techniques. Further, a literature review on different fiber optic sensors has been presented, highlighting their advantages and disadvantages. Finally, it has been concluded that FOPS and FBG sensors can provide necessary information to define the damage state in different structures. In chapter 3, a special purpose FBG sensor is developed for the in-situ measurement of resin pressure. Resin pressure or resin flow measurement is a very important of SHM of a curing composite laminate. The FBG sensor proposed in this chapter uses the principle of differential pressure in

liquids. Further, the stability and the reliability of the proposed FBG sensor have been proved. Finally, it has been concluded that this FBG sensor can be used effectively for the measurement of resin pressure in high temperature and low or zero bleed curing of composite laminates, such as out of autoclave curing.

In chapter 4, a new design of FOPS has been put forward for the purpose of structural health monitoring (SHM). The output of this FOPS is highly stable as compared to that of a normal FOPS system. In this design, only the central part of FOPS is sensitive, keeping the "leading-in" and "leading-out" parts insensitive. It allows SHM using FOPS that is sensitive only to the region of interest. This design is then implemented to locate and estimate the size of a crack in a cantilever. Unlike previous studies, the current approach considers the second vibrational mode along with the first vibrational mode to get a better understanding of the damage size and location. In this chapter, the location and sizing of a crack in a cantilever beam are studied theoretically and verified experimentally. An experimental study on cracks in Fixed-fixed beams has also been presented.

In chapter 5, a novel concept is proposed by which FBG and FOPS can be realized on a single fiber. According to this proposition an FBG written on a Polarizing Maintaining (PM) fiber can discern information from both FBG & FOPS sensors using only one decoding system. This reduces costs and complexities. Thus, it is proved that FBGs written on PM fiber (PM-FBGs) can be used for both, local and global SHM simultaneously. Further, a new design has been proposed which gives improved information on the damaged location in beam structures. In chapter 6, the scope of PM-FBGs is further investigated for the determination of crack location in two dimensional structures like, plates. The results demonstrate that the damage site can be located in two-dimensional structures using this multiplexed PM-FBG sensing array.

In chapter 7, a wavelength shifted chirped FBG (CFBG) sensing system has been demonstrated. This intensity based CFBG sensing system abrogates the need for optical spectrum analyzer (OSA) and presents a cost effective, compact and high resolution sensing module which can measure positive/negative strain and temperature simultaneously. This sensing module can perform dynamic FOPS measurement too,

thus giving FBG + FOPS data. In other words, the FBG and FOPS can again be realized on a single fiber using only one decoding system in this sensing module.

Chapter 8 concludes the entire work done in this thesis. A concrete discussion has been presented. Also, the future scope of the work presented in this report is also discussed in this chapter.

CHAPTER – 2 Literature Review and Motivation

2.1 Introduction

In this age of infrastructure, the world is full of beautifully engineered structures. These structures may be civil structures, like bridges, flyovers, tall buildings and towers etc. or mechanical structures like metal towers, vehicles etc. or composite structures like, the body of an aircraft, wings of wind turbine etc. The health of these structures is absolutely imperative because of a number of reasons. Several SHM techniques involving different smart materials are under investigation. Basically, smart materials help us to diagnose the severe damages in such structures. Few SHM techniques can perform local monitoring i.e. only a very specific region of a structure can be monitored. Few other SHM techniques can perform global monitoring i.e. the whole structure is monitored without specific knowledge of damage location and size. No smart material has been able to perform local and global SHM simultaneously so far. Different application areas where Structural Health monitoring (SHM) is required immensely have been indicated in Figure 2.1.
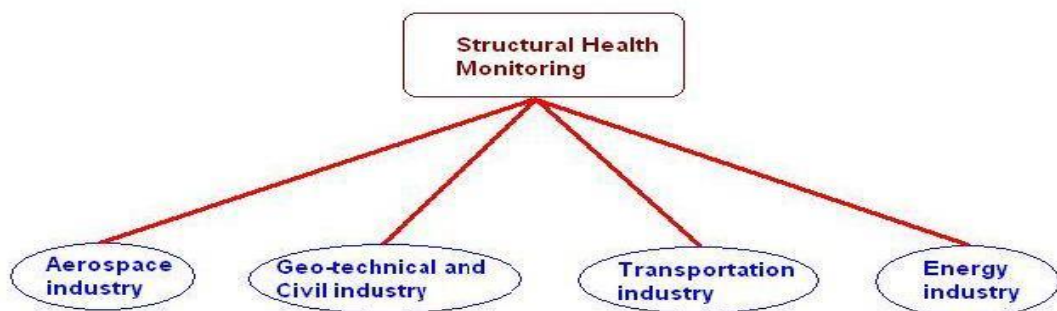
Figure 2.1: Different application areas of Structural Health Monitoring.

The aerospace industry is one of the major fields of application for SHM techniques. The flight environment is very harsh because of sudden changes in temperature, humidity, pressure, speed, loading conditions etc. Therefore, corrosion, delamination, cracks etc. happen. That is why, the SHM of an aircraft's wings, hull and the other important parts is essential. Since the good health of wings and hull ensure the safety of an aircraft, they are being monitored using different SHM technologies.

In Geo-technical and Civil industries, e.g. coal mining, gas pipelines, bridges and anchors etc. need a very effective SHM technique. Damages in all these structures happen quite often which usually causes heavy losses to the industries. The reasons for such damages could be natural calamities, harsh climate conditions etc. In Energy industry, the structures like, wind power station, wind turbines, power generators etc. have a deep requisite for SHM. In transportation, railway overhead contact lines get damaged very often; it increases the possibility of accident implying that their health monitoring is also essential.

2.2 Smart materials available for SHM in current trend

- Piezo-electric sensors
- Ultrasonic sensors
- Fiber Optic sensors (FOS)

2.2.1 Piezoelectric sensors

Piezoelectric materials are active smart materials as they actuate under electric field and also sense the reactions [4]. Piezoelectric sensors rely on the piezoelectric effect. In piezoelectric sensors, on the application of force the crystal lattices in the piezo material distort which in turn cause the reorientation of charges. This displacement of charges induces positive charge on one side and negative charge on the other side of the crystal. This induced surface charge is used to determine the pressure, acceleration, strain or force in piezo sensors [38, 39, 42 - 44].

The piezoelectric sensors can play a very important role in SHM industry.

Advantages of Piezoelectric sensors

- The piezoelectric materials are very sensitive to strain because of their high modulus of elasticity.
- The piezo materials are very rugged, have very high fundamental frequency and they show linearity over a wide amplitude range.
- Piezoelectric sensors are immune to electromagnetic radiation, allowing implementation in harsh environment.

Disadvantages of Piezoelectric sensors

- Piezoelectric sensors cannot be used for true static measurements. The dependence on conventional electronics is certainly a drawback. Piezo materials are not perfectly insulating and their internal resistance drops with time, resulting in a constant loss of charge. This in turn causes an inaccurate signal.

- Their internal resistance is dependent of temperature too. They are high impedance and can pick up stray voltages in the connecting wires.

- Embedment of piezo sensors into different structures is not possible, they can only be surface mounted.

- Real time and non-destructive SHM is not possible with piezo sensor.

Typical applications of piezoelectric sensors

Piezo sensors are used in consumer electronics like, disc drives, inkjet printers etc. In medical industry these sensors are used as disposable and they monitor foetal heart etc. In the military, they are used in depth sounders, guidance systems, hydrophones etc.

2.2.2 Ultrasonic sensors

Ultrasonic sensors are widely used for non-destructive testing and structural health monitoring. Ultrasonic guided waves can be used for long range inspection in elongated structures like, pipelines, railroad rails etc. [11]. Ultrasonic guided waves are suitable for structural health monitoring because of their good propagation capability. These sensors are highly sensitive to changes in structural properties [13].

Advantages of Ultrasonic sensors

- Ultrasonic sensors are highly sensitive to small defects.
- These sensors allow long range inspection.
- Ultrasonic waves cover the entire cross section of the waveguide.

Disadvantages of Ultrasonic sensors

- Data extraction and from these sensors is complex and time consuming because of the presence of multiple modes at any given frequency.

- Knowledge of complex phenomena like, mode attenuation is required to put the results in perspective.

- Complex signal processing is required to fully exploit the potential of these sensors.

Typical applications of ultrasonic sensors

Ultrasonic sensors are used for distance measurement, liquid level measurement and also for object detection. These sensors are also used to control the production process of printed circuit boards (PCBs) which are the indispensable feature of almost every machine available today.

2.2.3 Fiber Optic Sensors (FOS)

Fiber optic sensors are passive smart materials and they can only sense the reactions on the structure without the ability to actuate [15-20]. In fiber-optic sensors, information is primarily conveyed through a change in either phase or polarization or frequency or intensity of the input signal. The Fiber Optic Sensor (FOS) technologies are attractive in damage detection as they facilitate with real time non-destructive health monitoring of different mechanical and civil structures. FOS can be used for the measurement of strain, pressure, temperature, twist etc. [44-46].

Advantages of FOS

- FOS are not affected by any external electromagnetic field or high voltages. FOS are chemically inactive and have high temperature tolerance ($>1000^{o}$C). Therefore, FOS can be put in operation in chemically corrosive and harsh environmental conditions.

- As the diameter of fiber is very small (around 250 μm), FOS can be easily embedded into any engineering structures without disturbing its structural integrity.

- FOS are light weight, miniaturized, flexible and have low transmission losses. Therefore, FOS also have a long-range signal transmission or in other words FOS have remote sensing capabilities.

- Some of the FOS have multiplexing capabilities and several sensors can be put in series on a single fiber.

- Both global and local SHM can be performed by FOS.

Disadvantages of FOS

- FOS are made of glass and glass is brittle and fragile, so it is difficult to embed it in metallic structures. That is why FOS are surface mounted in case of metallic structures.
- Few FOS technologies are used for local SHM and few others are used for global SHM. Simultaneous global and local SHM has not been accomplished so far. Having been able to achieve this will make the system more informative, compact and cost effective.

2.3 Advantages of FOS over other contemporary sensors for SHM

As mentioned earlier, piezoelectric sensors cannot provide true measurements for a long duration as there occurs a significant charge loss over a certain period of time. But there is no such thing in FOS. Real time and non-destructive monitoring of a structure is not possible with piezoelectric sensors, but it can be performed easily with the FOS. FOS can be embedded into composite and ceramic structures, but the embedment of piezo sensors is not possible. Also multiplexing and remote sensing capabilities of FOS technologies give an extra credit to FOS over piezoelectric sensors.

The contribution of different FOS in the field of SHM is discussed in the following sections.

2.4 Fabry-Perot interferometer fiber optic sensors for SHM

The Fabry-Perot interferometer form of fiber-optic sensor which utilizes the multiple-beam interference has been demonstrated [21, 47 & 48]. The fiber-optic Fabry-Perot interferometer consists of a single mode fiber with dielectric coated high reflectance end faces. It has many attractive features as the interferometric fiber sensor.

2.4.1 Fiber optic Fabry-Perot interferometer (FFPI) for the measurement of temperature and mechanical vibrations

The temperature induces a phase shift in FFPI. The FFPI was inserted in a glass tube and it was heated and cooled. The number of interference fringes in the output of the

FFPI changes with temperature as shown in the Figure 2.2. One interference fringe corresponds to the change of $\lambda/2$ in the optical path length of FFPI [47]. By counting the number of fringes in the output of the FFPI the change in the temperature can be monitored as shown in the Figure 2.3.
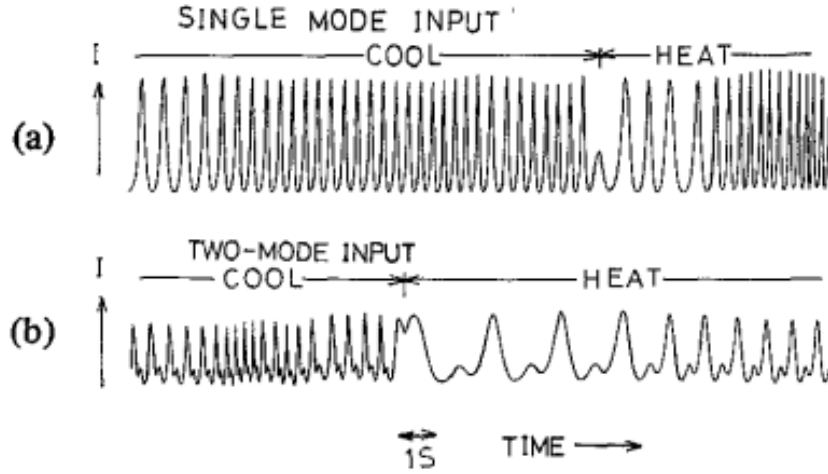
Figure 2.2: Output light intensity I of a 24 cm FFPI when it was heated or cooled; input light is (a) single mode and (b) two modes [47].
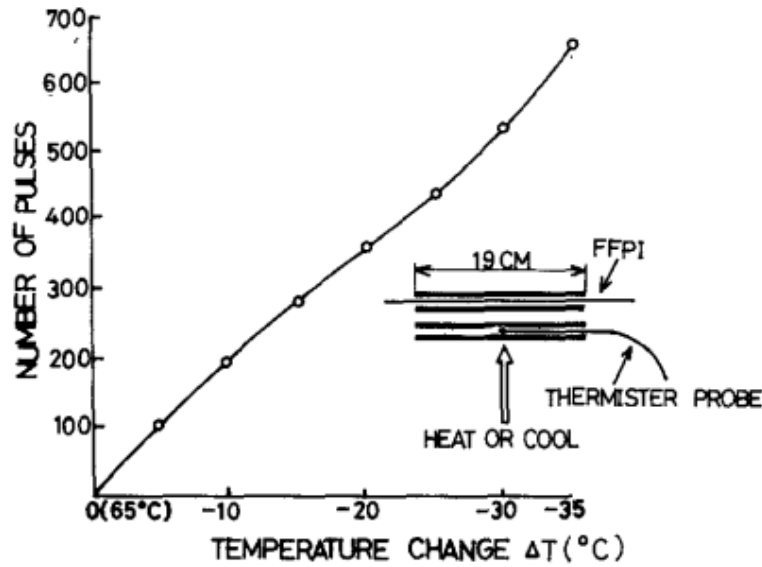
Figure 2.3: Number of interference fringes as a function change of temperature of a 19 cm length of FFPI [47].

FFPI is a reliable sensor for mechanical vibrations too. The FFPI of 10 m was put in a coil on an optical bench and then the bench was impacted. The output signal is shown in the Figure 2.4. This impact introduced a phase modulation of several π. Figures

12(a) and 12(b) correspond to the cases when the input light is the single mode and two modes respectively with an intensity ratio of 5:1 [47].
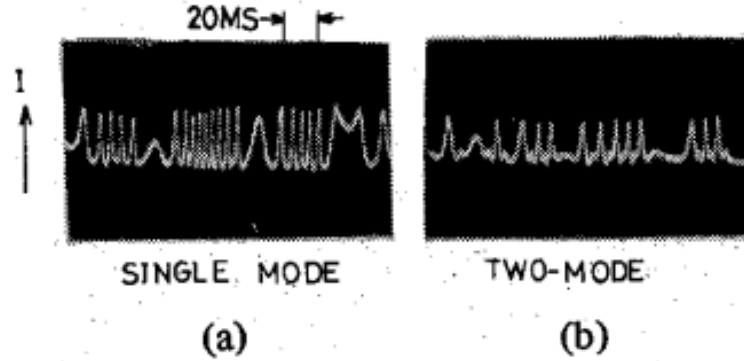
Figure 2.4: Output light intensity of a 10 m FFPI subject to mechanical vibrations induced by impact in cases that input light is (a) single mode and (b) two modes [47].

2.4.2 Extrinsic Fabry–Perot interferometer (EFPI) sensor
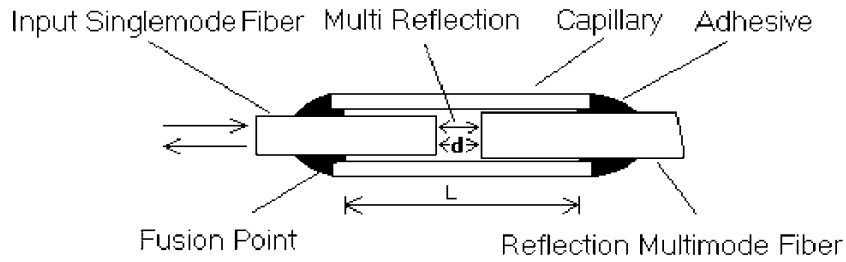
Figure 2.5: Schematic configuration of EFPI sensor [49].

In this EFPI sensor, two fibers (one single mode and one multi-mode) were used as the two reflectors. The schematic diagram of EFPI is shown in the Figure 2.5. The optical spectrum of EFPI with 50 μm cavity length is shown in the Figure 2.6. The cavity length 'd' between the two mirrors changes if any external load is applied. This cavity length can be determined using the optical spectrum of Fabry-Perot interferometer. The accurate cavity length can be measured by modulation in the optical spectrum. It is given by:

$$d = \frac{m\lambda_1\lambda_2}{2(\lambda_2 - \lambda_1)}$$

(2.1)
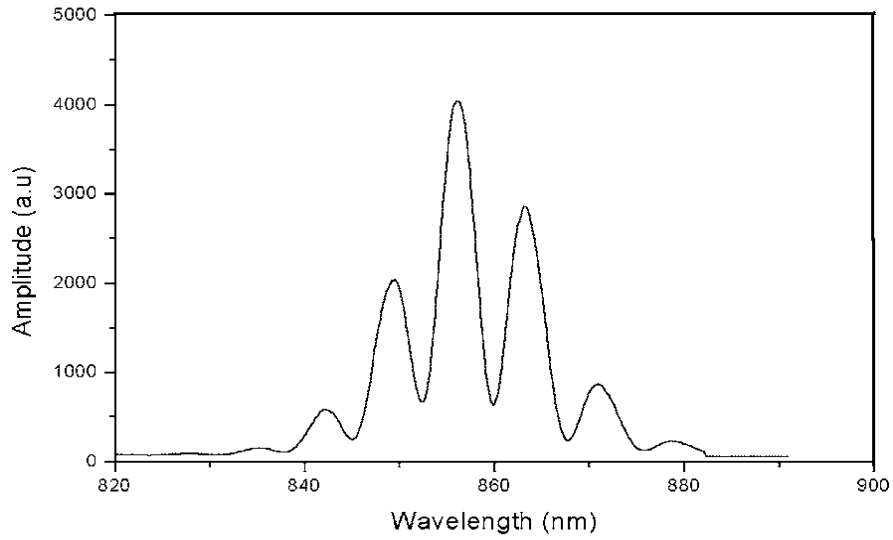
Figure 2.6: Optical spectrum of EFPI sensor with a 50 μm cavity length [49].

2.4.2.1 Extrinsic Fabry-Perot interferometer (EFPI) for damage monitoring

The EFPI was surface mounted on an aluminum plate and it was embedded into a CFRP composite laminate $(0)_{16}$ [50]. The cracks were made as shown in the Figure 2.7 and Figure 2.8.
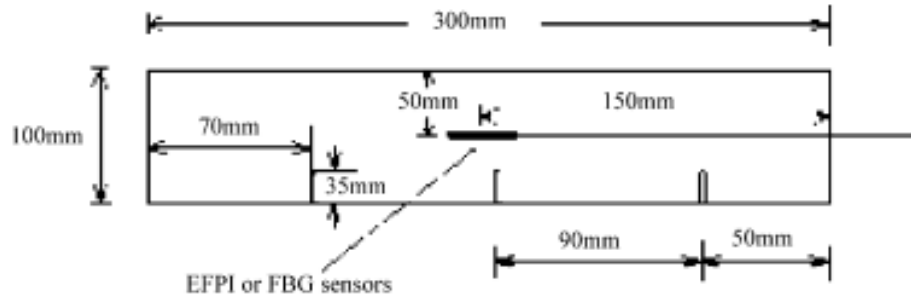
Figure 2.7: Diagrammatic illustration of aluminum plate with three cracks [50].
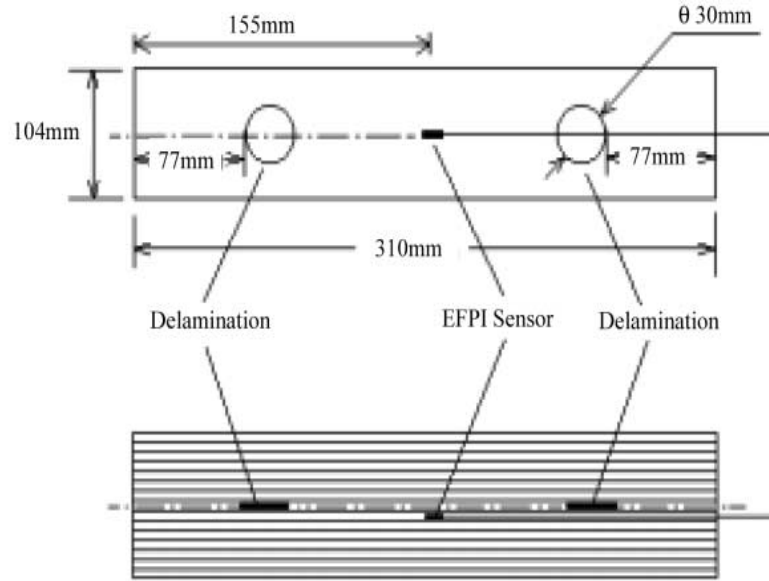
Figure 2.8: Diagrammatic illustration of CFRP composite laminate (0)16 with two damages. [50].

Three point bending tests were conducted to see the effect of cracks in both the cases. From Figure 2.9, it can be realized that due the presence of cracks the strain increased in both the aluminum beam and the CFRP composite laminate. Thus, EFPI sensors could be effectively used to investigate the structural damage.

(a)   (b)
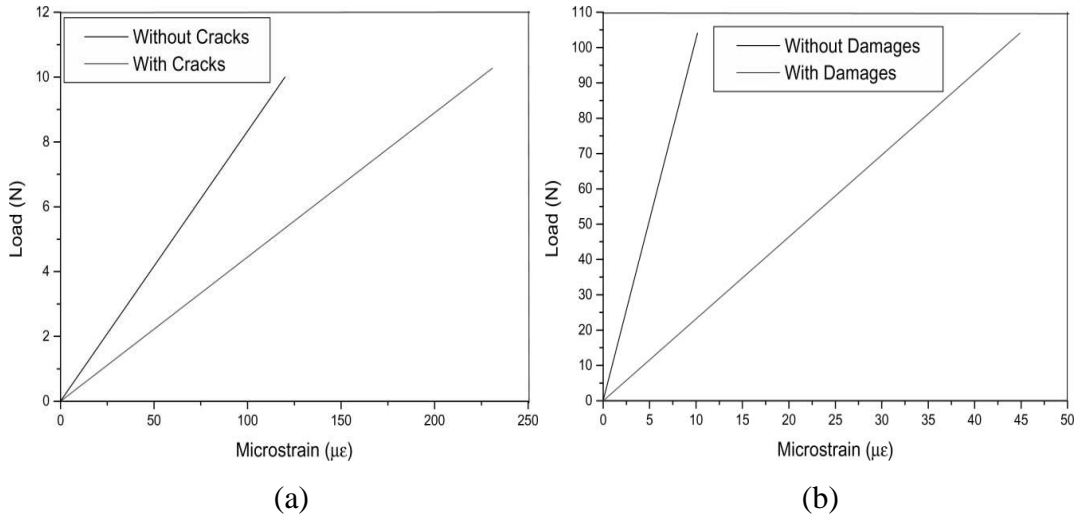
Figure 2.9: Results of 3-point bending test of (a) aluminum beam by using surface mounted EFPI and (b) CFRP composite laminate (0)16 by using embedded EFPI [50].

2.4.2.2 Extrinsic Fabry-Perot interferometer (EFPI) for the real-time cure monitoring of smart composite material

The performance of smart composite material can be improved if real-time cure monitoring of the composite material could be done. In 2002 it was done by embedding extrinsic Fabry-perot interferometer (EFPI) sensors in carbon/epoxy composite laminates as shown in Figure 2.10. First, the CFRP composite laminate was cured without any damage in it and then it was cured with a delamination as shown in the Figure 2.10. The results are shown in the Figure 2.11. From these curves (Figures 2.11(a) and (b)) all the three phases could be seen clearly. If the cure strains in the composite without and with damage are compared, it can be seen that the cure strain in the composite without damage is smaller than in that of with damage. It is because the shrinkage in the composite with damage is relatively larger. Hence, EFPI sensors are quite capable of monitoring the live strain in the composite laminate [49].
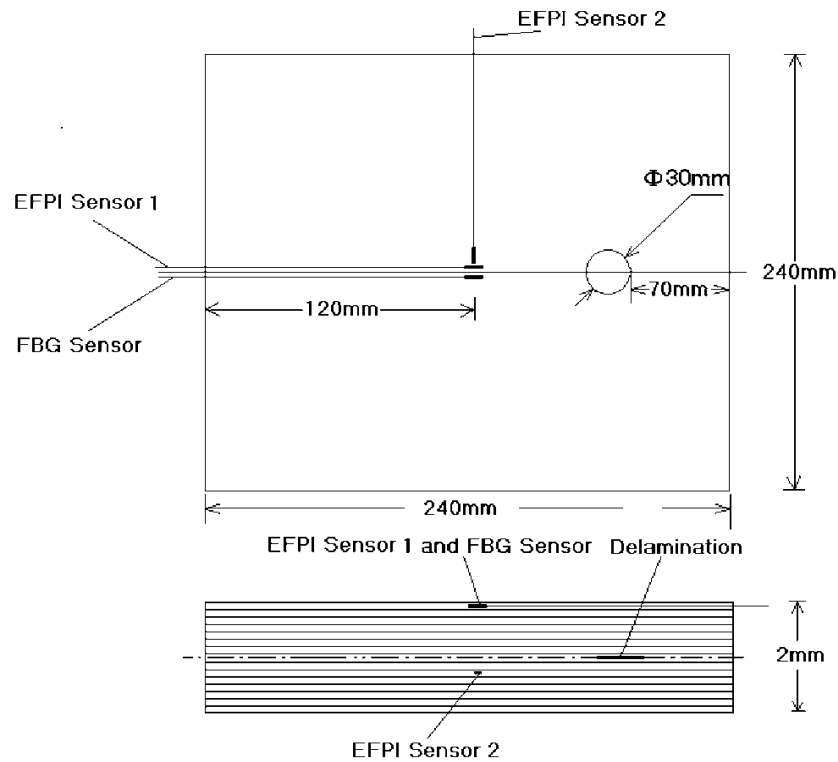
Figure 2.10: A schematic diagram of the CFRP composite specimen (04/904/904/04) with one delamination [49].

(a)   (b)
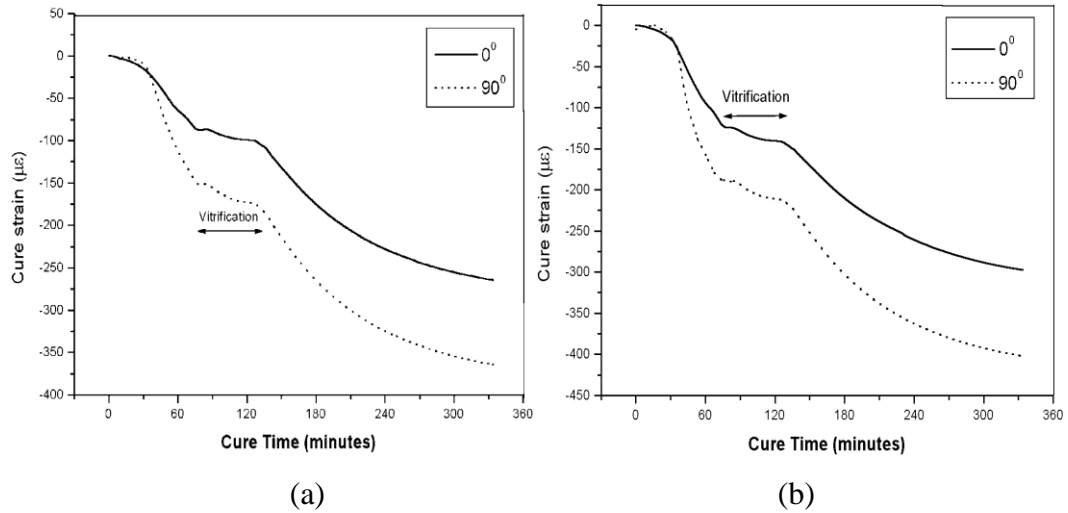
Figure 2.11: Cure monitoring curves of a CFRP composite laminate (04/904/904/04)
(a) without damage (b) with damage using EFPI sensors [49].

2.4.2.3 Stabilized EFPI sensor for damage monitoring by detecting acoustic emission

EFPI can also detect the fracture signals generated acoustic emission. In order to be able to do this, a phase compensating technique is necessary to maintain the phase. A phase stabilization control system was developed which is composed of a broadband light source, a fiber Fabry–Perot (FP) tunable filter and a control-circuit board [51].

A gold plated EFPI sensor was embedded in the cross-ply composite specimen and tensile loading was applied on the specimen. The tensile test of the composite specimen was carried out until it was fractured. Successive fracture signals were detected with the oscilloscope during the extension of the specimen. The strain was simultaneously measured. The stress–strain curve and the total amount of acoustic emission signals are presented in Figure 2.12. The failure occurred at about 1.6% strain. Sixty acoustic emissions were detected by EFPI before the final fracture [51]. Thus, fracture propagation in composite materials can be monitored through this stabilized EFPI sensor system by counting accumulated acoustic emission.
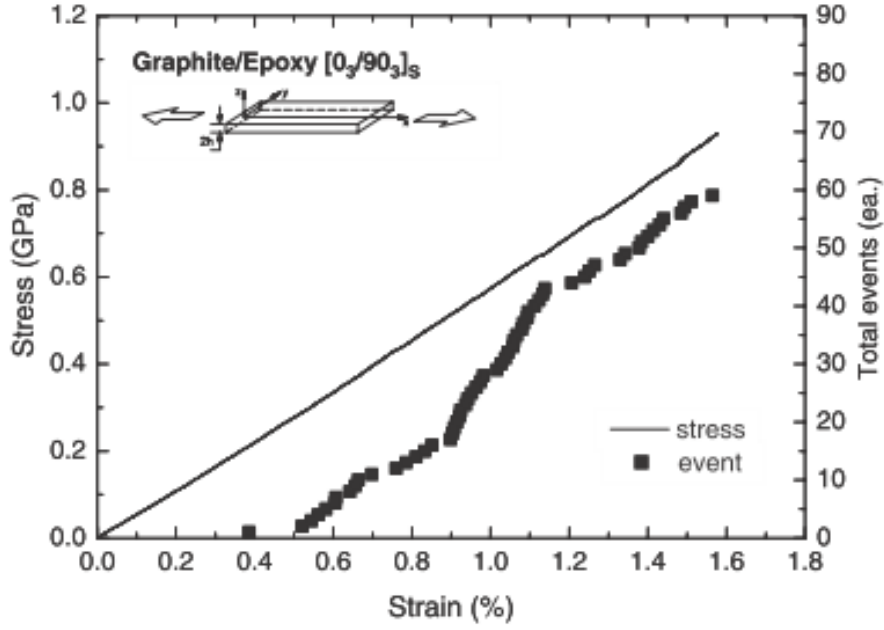
Figure 2.12: The stress–strain curve of the composite specimen Gr/Ep [0_3 / 90_3]$_S$ and an accumulated acoustic emission curve [51].

2.5 Fiber Optic Curvature Sensor (FOCS) for SHM

In FOCS, the fiber is attached to the structure. FOCS is based on the principle that the light transmission loss will increase with increase in bending or curvature of fiber (or structure) [53-55]. Reduction in the flexural stiffness of a structure due to damage causes corresponding increase in the curvature under identical loading conditions which will intern increase the light transmission loss in the fiber. The Fiber Optic Curvature Sensors (FOCS) provides a direct measure of the curvature in terms of intensity of the light coming out of the fiber. Thus, SHM can be performed by measuring the change in the curvature of a structure under identical loading conditions.

2.5.1 Fiber Optic Curvature Sensors (FOCS) for damage monitoring in beam structures

In FOCS, the modulation of light throughput is very linear to with the curvature [35]. The relation among the flexural stiffness (EI) and the bending moment (M) of a beam bent with a curvature (1/R) is given by [52].

$$\frac{1}{R} = \frac{M}{EI} \tag{2.2}$$

20

The overall damage in a structure is measured in terms of change in flexural stiffness of that structure. The moment (load) against curvature (i.e. the intensity of light coming out of fiber) must be plotted. The slope of this line determines the sensitivity of the sensor. The slop or the sensitivity of the sensor changes with damage [35].

The FOCS was bonded to the bottom of an aluminum beam of size $300 \times 100 \times 1.2$ mm^3 as shown in Figure 2.13. In this three point bending arrangement, the specimen beams were loaded increasingly. The Intensity of the light coming out of FOCS was recorded as a function of applied load. Figure 2.14 shows the static response of FOCS for different number of cracks at different locations. The output varies linearly with the load. The slopes of these curves are inversely proportional to the stiffness, hence higher damage resulting in larger slopes and indicating reduced stiffness [34]. It was proved that FOCS are capable of performing a static loading test for global SHM.
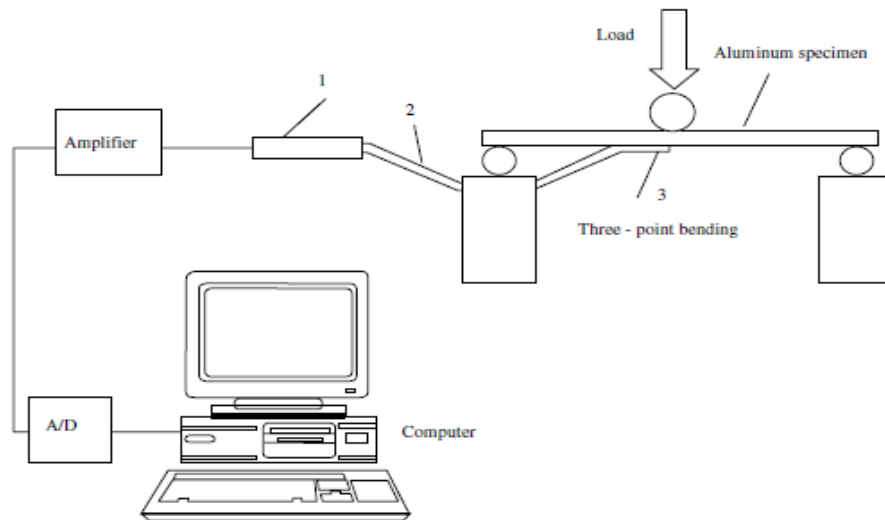
Figure 2.13: Schematic diagram of the FOCS for damage detection. 1 represents one LED with two detectors, 2 represents one plastic fiber loop laminated in latex and urethane (insensitive to curvature) and 3 represents the 2 mm treated zone [34].
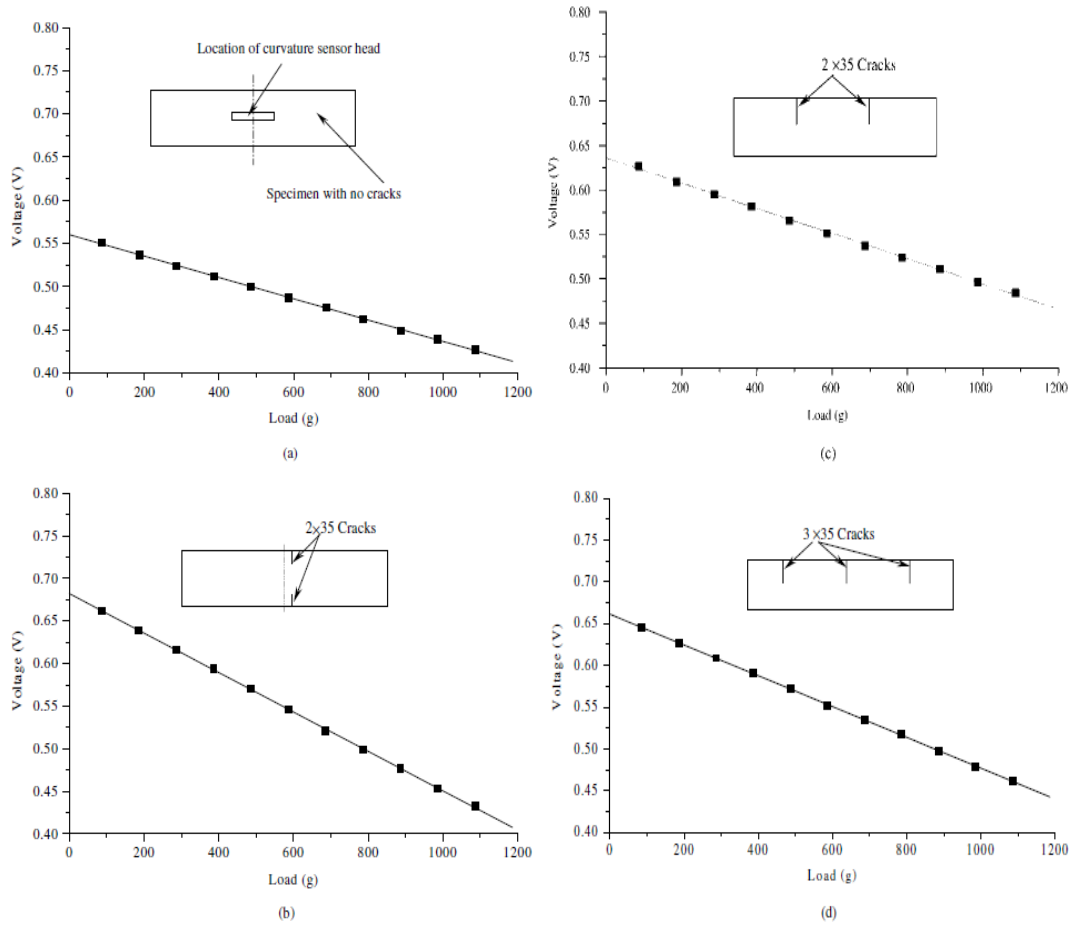
Figure 2.14: The static response of a specimen with various cracks: (a) no crack (b) two cracks (opposite sides) (c) specimen with two cracks (same side) and (d) three cracks [34].

2.5.2 Temperature and strain independent Fiber Optic Curvature Sensors (FOCS)

A different design of FOCS was proposed which could measure the true curvature independent of temperature and strain changes [56]. In this design, three fibers (SMF-MMF-SMF) were spliced in series as shown in Figure 2.15.

Figure 2.15: Curvature sensor configuration [51].

When the light propagates through input single mode fiber (SMF) and enters the multimode fiber (MMF), higher modes of MMF are excited and interference among different modes occurs. The optical power coupled into the output SMF depends on the amplitudes and relative phases of various modes of MMF at its output [56]. The transmitted output optical power has two wavelength loss bands (centered at λ_1 and λ_2) as shown in Figure 2.16. λ_1 and λ_2 are sensitive to curvature. The problem of temperature and strain cross-sensitivity is substantially eliminated. The curvature response for the measurement parameter, $\Delta(\lambda_2 - \lambda_1)$ is shown in the Figure 2.17. This sensor design possesses potential for SHM through curvature measurement.
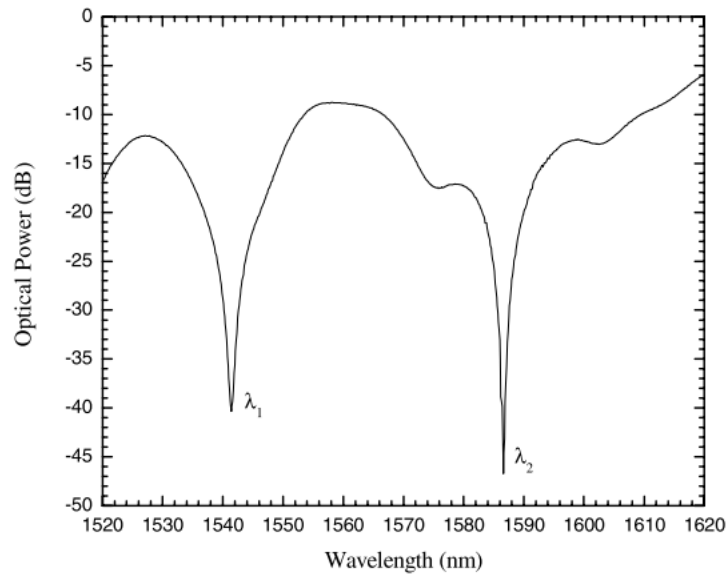
Figure 2.16: Optical spectrum of the SMF-MMF-SMF sensor design [56].
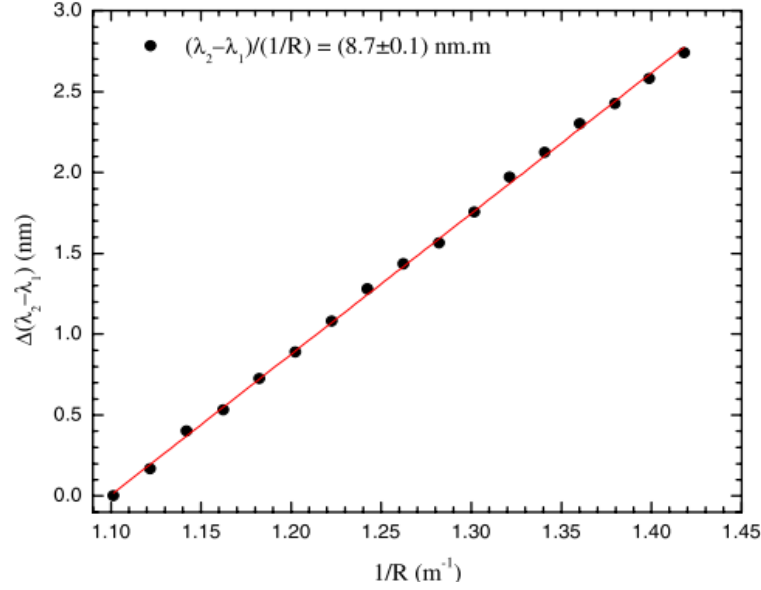
Figure 2.17: Curvature response for the measurement parameter, $\Delta(\lambda_2 - \lambda_1)$ [56].

2.6 Fiber Optic Polarimetric Sensors (FOPS) for SHM

Of the various fiber optic sensors available, FOPS has its own unique advantages [57]. In FOPS, a polarization maintaining (PM) fiber is used instead of normal single mode fiber. The phase or state of polarization (SOP) of output light is maintained, provided no strain is applied to the PM fiber. If the PM fiber experiences the longitudinal strain, the SOP of the light coming out of the PM fiber will change. SHM of structures is done by monitoring the change in SOP of output light.

2.6.1 Fiber Optic Polarimetric Sensors (FOPS) for global SHM by static test

SHM of beam structures was carried out by a static loading test using FOPS [35]. The schematic diagram of a FOPS system for static health monitoring is shown in thee Figure 2.18. The load P was applied at the center of the beam of length $2L$. The moment at the center of the beam is $M = PL$. The strain in the bottom layer is given by [58]

$$\varepsilon = (\frac{Lc}{EI})P \tag{2.3}$$

The phase of the light coming out of the PM fiber varies sinusoidally with increasing strain as described by equation (1.1). Therefore the intensities (D_1 and D_2) and hence the SOP varies sinusoidally with increasing load (P) [35]. If damage happens in the

beam, the flexural stiffness (EI) will go down and therefore, more strain (ε) will occur with identical load (P).

$$S = \frac{D_1 - D_2}{D_1 + D_2} \qquad (2.4)$$

This increased strain due to the damage results in a more rapid change in SOP and therefore, the period of SOP cycle reduces. Here the SOP is given by

D_1 and D_2 are the voltages measured by the detector 1 and detector 2 respectively (Figure 2.18). The FOPS (or PM fiber) was bonded to the bottom of an aluminum beam of size $300 \times 100 \times 1.2$ mm^3 as shown in Figure 2.18. In the three point bending arrangement shown in Figure 2.18, the specimen beams were increasingly loaded and the SOP was recorded as a function of applied load. Figures 2.19(a)–(e) give the static responses of the aluminum beams with different crack scenarios.
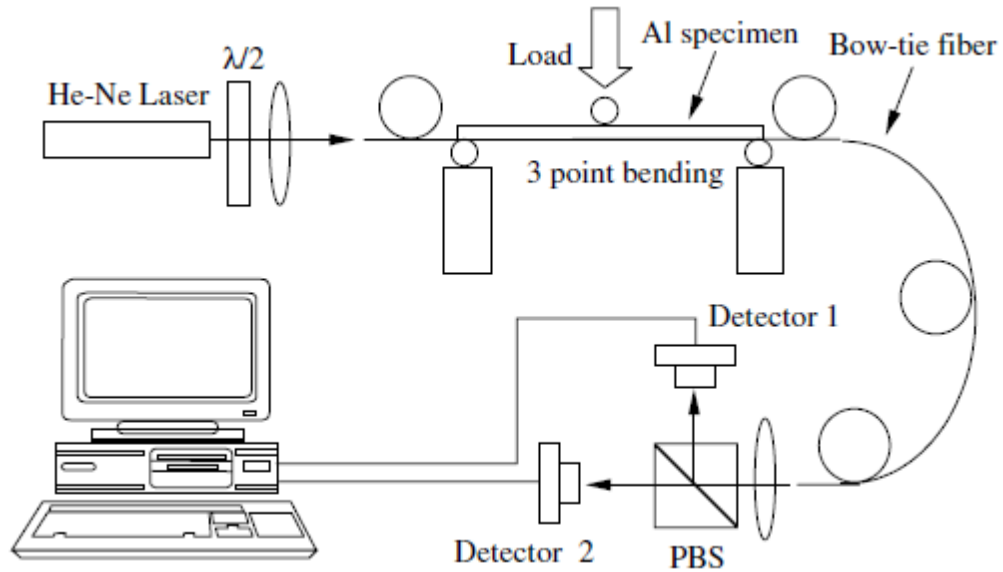
Figure 2.18: Schematic diagram of the experimental set-up for the static test [35].
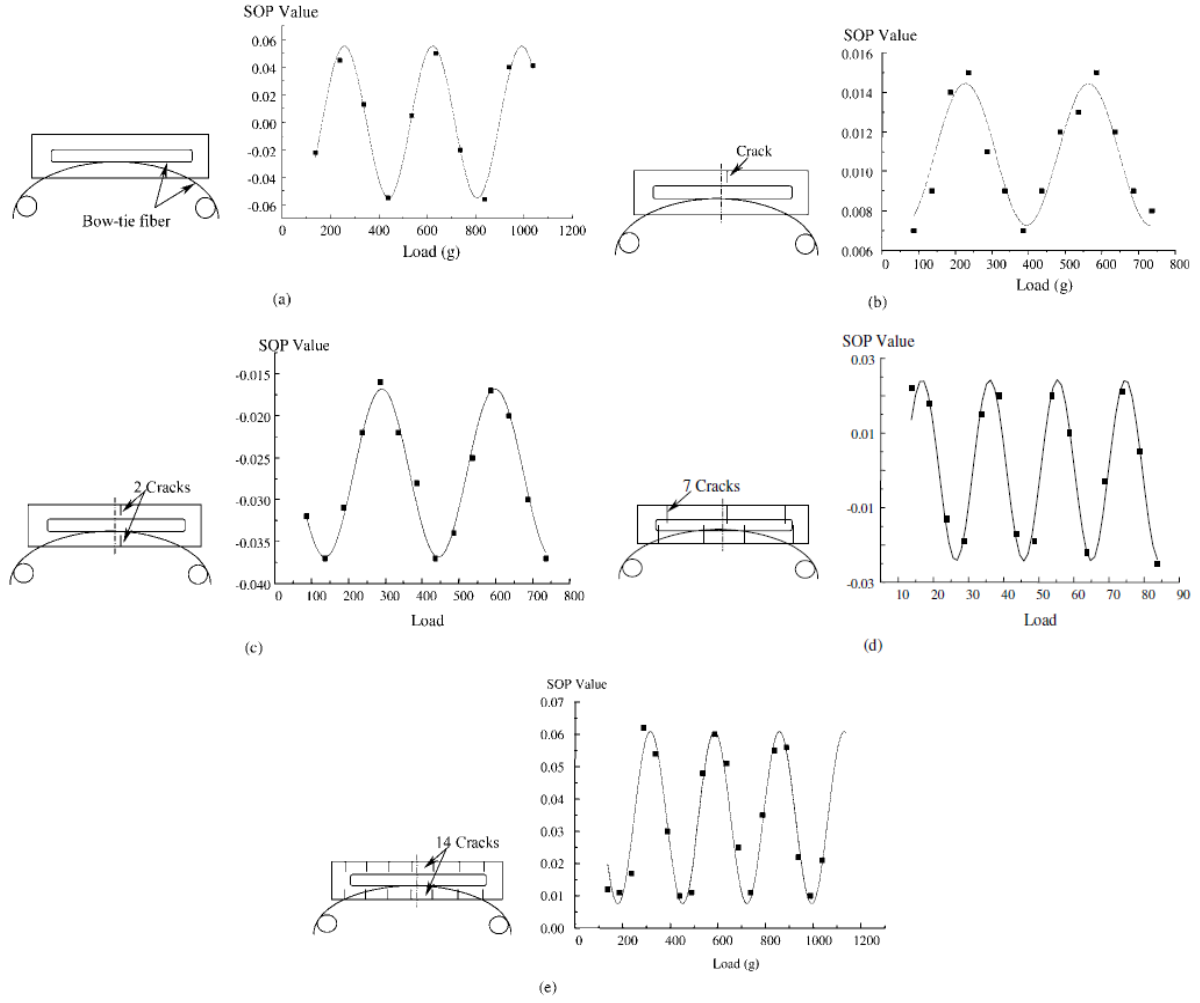
Figure 2.19: SOP cycles with (a) no cracks; (b) one crack of 30 mm ; (c) two cracks, each of 30 mm; (d) seven cracks, each of 40 mm; and (e) 14 cracks, each of 20 mm [35].

From Figure 2.19, it is clear that the period of SOP cycle reduces with both, the number of cracks and size of the cracks. A damage factor called static damage factor (SDF) was defined as [35]

$$SDF = \frac{(Load\ P, required\ for\ one\ SOP\ cycle)_{damaged}}{(Load\ P, required\ for\ one\ SOP\ cycle)_{undamaged}} \qquad (2.5)$$

Table 2.1 shows the SDF for increasing numbers of cracks and table 2.2 shows the effect of crack length on the SDF. From these tables, it was established that the effect of size of the cracks on SOP cycle period is more than the number of cracks. This experiment proved that FOPS are capable of performing static test for global health monitoring.

Table 2.1: Effect of the number of cracks on the load required to produce a phase change of 2π for FOPS [35].

Number of cracks	Load for a phase change of 2π (g)	Damage factor (SDF)
0	366.5	1
1 (30 mm)	336.2	0.92
2 (30 mm each)	308.2	0.84
14 (20 mm each)	271.4	0.74

Table 2.2: Effect of the crack length on the load required to produce a phase change of 2π for FOPS [35].

Number of cracks	Load for a phase change of 2π (g)	Damage factor (SDF)
0	366.5	1
7 (40 mm each)	193.1	0.53
14 (20 mm each)	271.4	0.74

2.6.2 Fiber Optic Polarimetric Sensors (FOPS) for global SHM by dynamic test

Every structure has fundamental modes of vibration, the frequencies of which depend on the dimensions and stiffness of that structure. As the structure gets damaged, its stiffness goes down and hence the frequencies of fundamental modes go down too. Utilizing this phenomenon, it was proved that FOPS could monitor the health of structures dynamically. The schematic diagram of FOPS for dynamic health monitoring is shown in the Figure 2.20. The frequency of nth mode for the specimen (cantilever) shown in the Figure 2.20 is given by [59]

$$\omega_n = [a \frac{(2n-1)\pi}{2}]^2 \sqrt{\frac{EI}{\rho A}} \qquad (2.6)$$

where EI is the stiffness, A is the cross section and ρ is the density of the specimen. For dynamic SHM, a factor called Damage Dynamic Factor (DDF) was proposed and it was defined as

$$DDF = [\frac{(\omega_n)_{damaged}}{(\omega_n)_{undamaged}}]^2 \qquad (2.7)$$
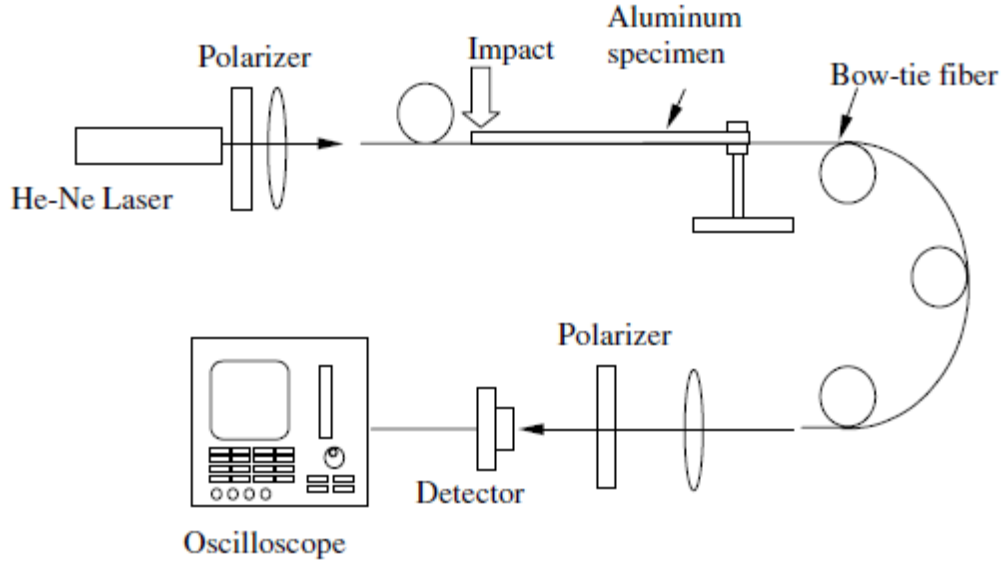
Figure 2.20: Experimental set-up for the dynamic test [35].

Fourier analysis of the dynamic signal of FOPS gives the frequency of first fundamental mode of the specimen beam along with the frequencies of its harmonics. Figures 2.21(a)–(e) show the oscillatory dynamic signal of FOPS for specimen beams with different number of cracks. Table 2.3 shows fundamental frequencies of first mode and the DDF for different numbers of cracks [35].

(a)

(b)

(c)

(d)

(e)
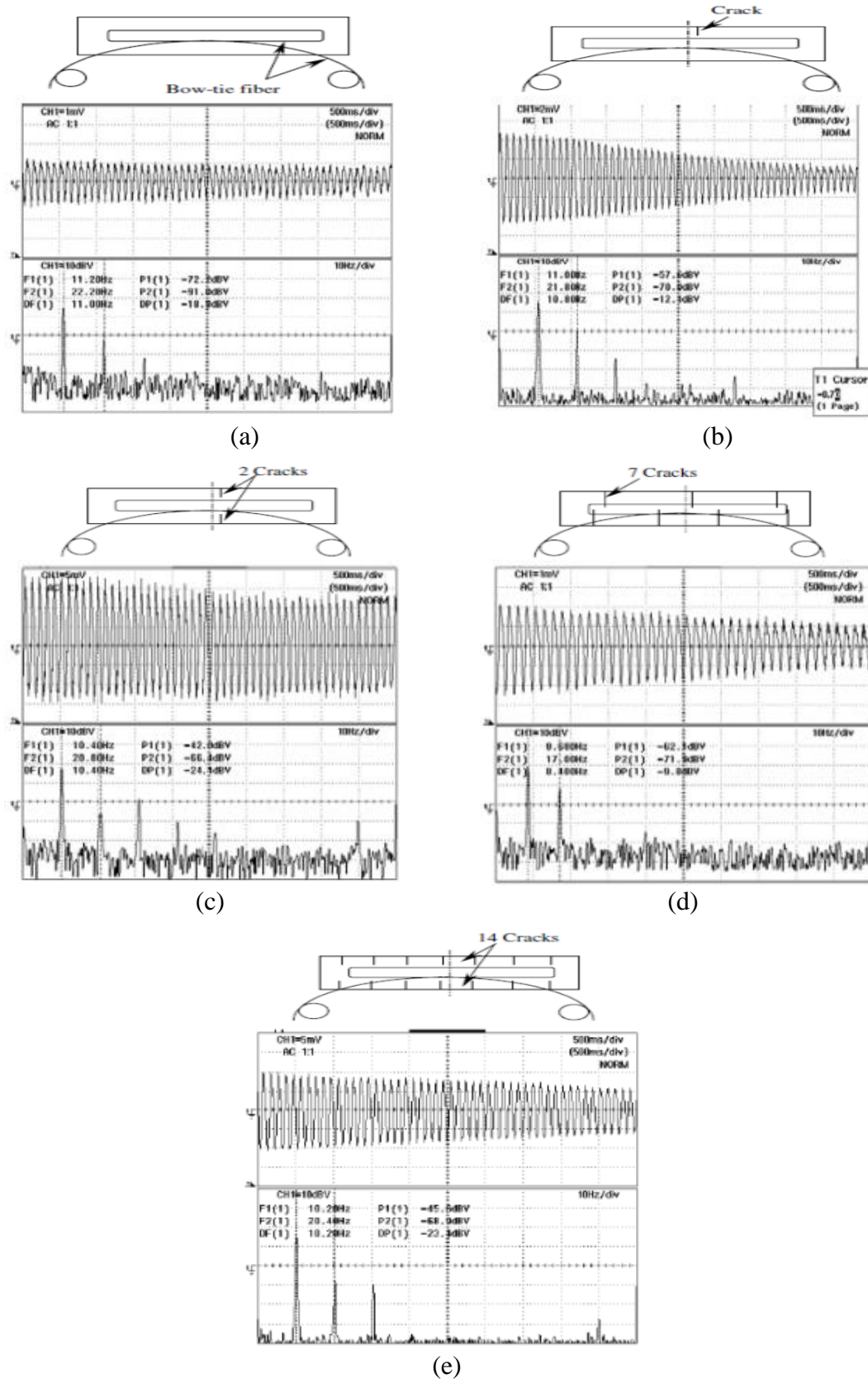
Figure 2.21: Dynamic test results for specimen beam with: (a) no cracks; (b) one crack of 35 mm; (c) two cracks, each of 35 mm; (d) seven cracks, each of 40 mm; and (e) 14 cracks, each 20 mm [35].

Table 2.3: Dynamic damage factor (DDF) calculated for different number of cracks
[35].

Number of cracks	f1 (Hz)	DDF
0	11.20	1
1 (30 mm)	11.00	0.96
2 (30 mm each)	10.40	0.86
7 (40 mm each)	8.600	0.59
14 (20 mm each)	10.20	0.83

It is evident that FOPS is suitable candidate for both static and dynamic global health monitoring. No FOPS method has been proposed for local health monitoring so far. Only knowing that there is damage without any specific details is not enough. Location and size of the damage are equally important.

2.6.3 Fiber Optic Polarimetric Sensors (FOPS) for the measurement of high pressure

A FOPS configuration for high pressure measurement was presented [60]. It is known that applying lateral compressive strain on PM or Hi-Bi fiber either cancels or on the other hand, increases the birefringence ($\Delta\beta$) of the PM fiber by changing the relative retardation of the two propagating orthogonal polarizations (fast and slow) modes. The output intensity of the sensor (I) observed at 45° from the fiber axis, changes sinusoidally with the change in the birefringence ($\Delta\beta$) [60]. The sinusoidal variation of output intensity (I) with increasing load for two different lengths of PM fiber (3mm and 40mm) is shown in the Figure 2.22. The normalized sensor's output as a function of pressure with computational error is shown in Figure 2.23. The computational error will be minimal only within the range of the nearly linear part of the characteristics, as shown in Figure 2.23.
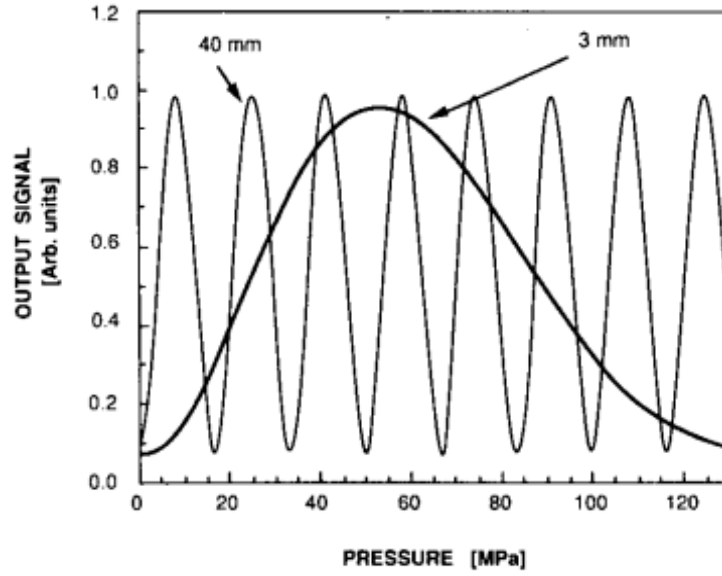
Figure 2.22: Detected sensor output (*I*) as a function of high pressure for two lengths
of a PM fiber [60].
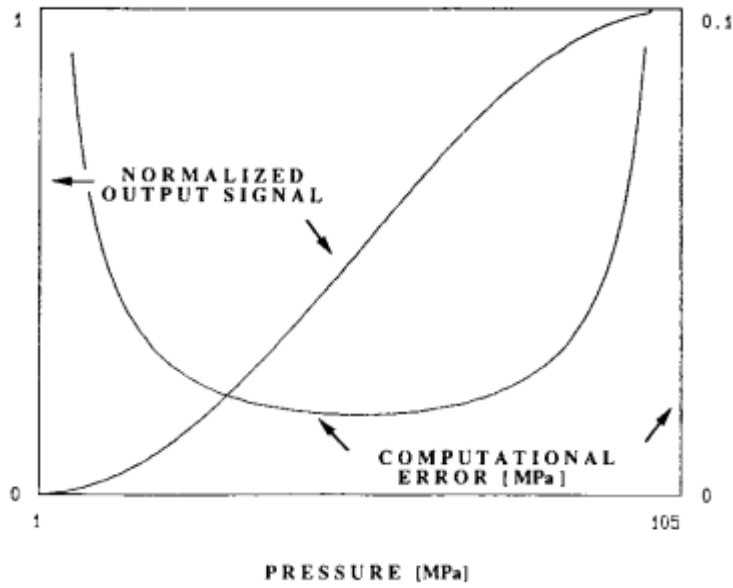
Figure 2.23: Computational error in pressure measurement [60].

2.7 Fiber Bragg grating (FBG) for SHM

Formation of FBGs was reported more than three decades ago [61], but intensive study
began only after when a controllable and effective method for their fabrication was
devised about two decades ago [62]. In recent years, there have been a number of
initiatives towards the development and deployment of FBG sensors for structural

engineering [63-65]. FBGs are suitable for local structural health monitoring or in other words, they can be used for spot strain measurement only [66].

2.7.1 FBG for damage monitoring by strain measurement

The real time non-destructive health monitoring techniques play a very important role in assessing the performance of different engineering structures when they are in operation. In 2002 Fiber Bragg grating (FBG) sensors were investigated for the real time health monitoring of aluminum plate and CFRP composite laminate [50]. FBGs were surface mounted on an aluminum plate and imbedded into a CFRP lamina. Loading test was carried out to calculate strain both the specimen as shown in the Figure 2.24. Further, the specimens were damaged and then again strain was calculated at different loads. The strain vs load plots are shown in the Figures 2.25(a) and (b) for both the specimen.
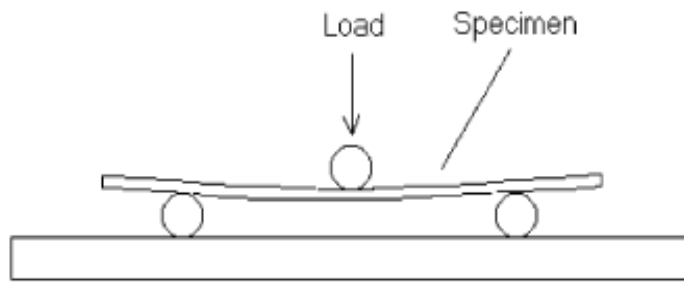
Figure 2.24: Experimental schematic diagram of three point bending test [50].

<center>(a)   (b)</center>
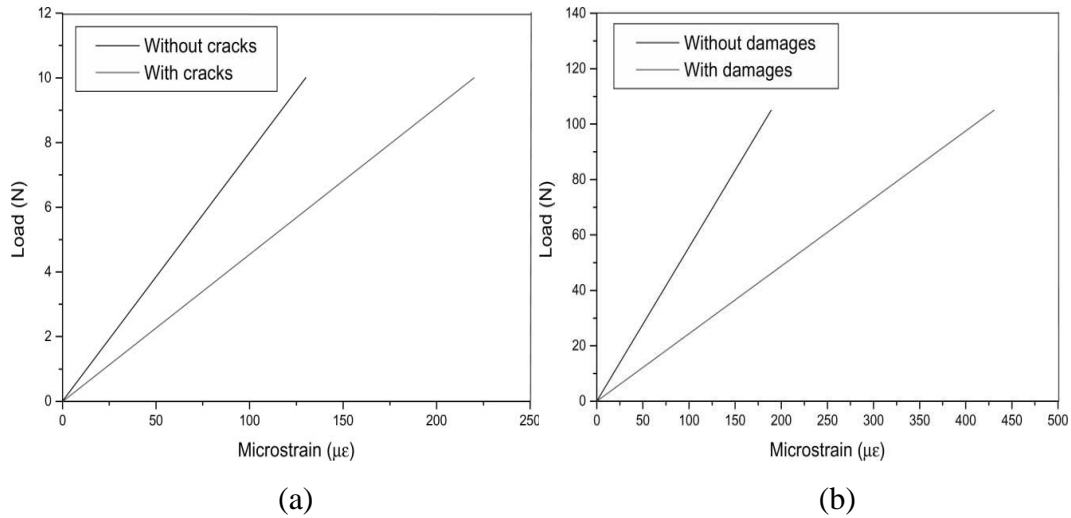
Figure 2.25: Results of 3-point bending test of (a) aluminum beam by using surface mounted FBG and (b) CFRP composite laminate (0)16 by using embedded FBG [50].

Now from Figure 2.25 it can be seen that the strain in undamaged aluminum beam and CFRP composite laminate is relatively much lower than it is in damaged aluminum beam and CFRP composite laminate respectively. Thus, FBG sensors could be effectively used to investigate the structural damage.

2.7.2 FBG for the real-time cure monitoring of smart composite material

The performance of smart composite material can be improved if real-time cure monitoring of the composite material could be done. It was done by embedding FBG sensors in carbon/epoxy composite laminates. First, the CFRP composite laminate was cured without any damage in it and then it was cured with a delamination. The results are shown in the Figure 2.26. From these curves (Figures 2.26) all the three phases could be seen clearly. If the cure strains in the composite without and with damage are compared, it can be seen that the cure strain in the composite without damage is smaller than in that of with damage. It is because the shrinkage in the composite with damage is relatively larger. Hence, FBG sensors are quite capable of monitoring the live strain in the composite laminate [49].
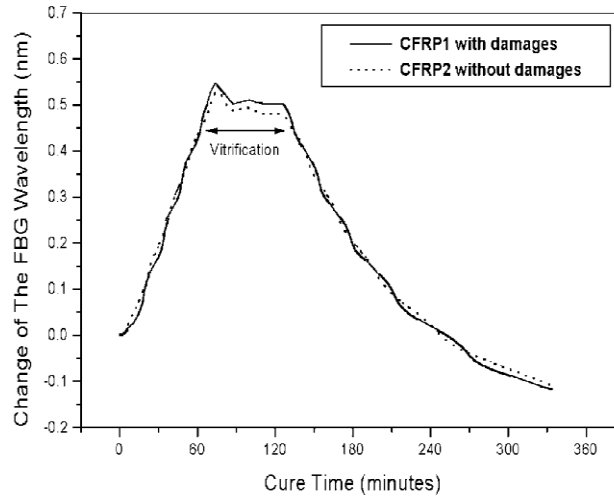
Figure 2.26: Cure monitoring curves of a CFRP composite laminate (04/904/904/04) with and without damage using FBG [49].

2.7.3 FBG multiplexing for SHM of large structures

A number of FBGs can be multiplexed in a single fiber. The feasibility of using these multiplexed FBG sensors for structural health monitoring was investigated in 2005. The multiplexed FBG sensors were installed on Hong Kong's landmark Tsing Ma Bridge (TMB). Forty FBG sensors were divided into three arrays and these arrays were installed on the hanger cable, rocker bearing and truss girders of the TMB as shown in the Figure 2.27 [67]. Conventional strain gauges were also installed along with FBG for the comparison purpose.
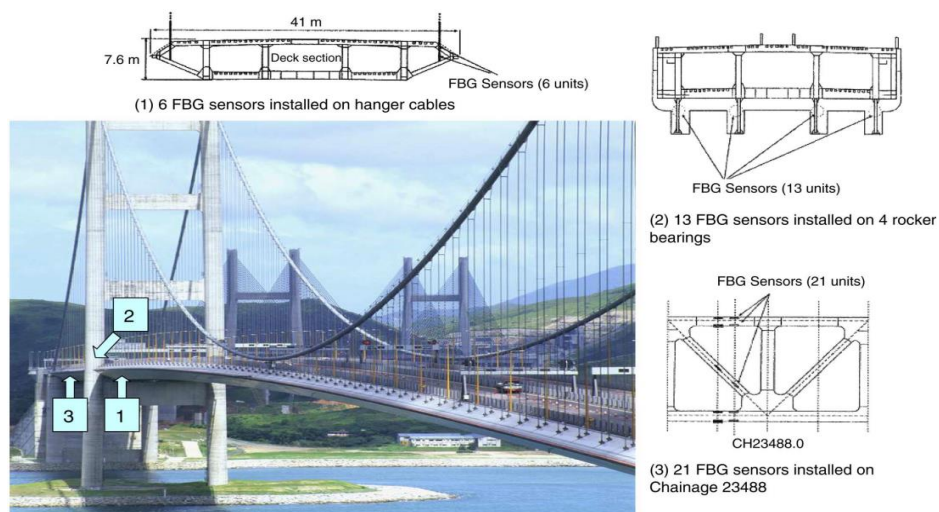
Figure 2.27: Forty FBG sensors installed on the Tsing Ma bridge to measure temperature and strain at (1) hanger cable, (2) rocker bearing and (3) truss girders of the section.

There are a number of interrogation techniques for multiplexed FBG system; time-division multiplexing (TDM), spatial-division multiplexing (SDM), frequency-division multiplexing (FDM) and wavelength-division multiplexing (WDM). In this study, a different high speed interrogation system (DEMINSYS) was used. This system was developed by TNO TPD [68]. This system can read the samples with a frequency of about 20 KHz and the detection limit for this system is less than 1 pm. The experimental setup for the FBG interrogation system is shown in the Figure 2.28.
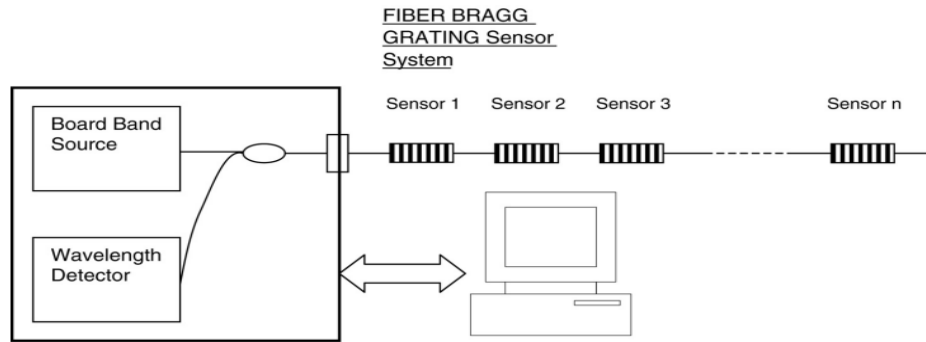
Figure 2.28: Experimental setup of the FBG interrogation system [67].

The change in the Bragg wavelength in response to strain and temperature is given by [67]:

$$\Delta\lambda_B = \alpha\Delta\varepsilon + \beta\Delta T \qquad (2.8)$$

where α, β are the wavelength-strain sensitive factor and wavelength-temperature sensitive factor, respectively; $\Delta\varepsilon$ is the change in axial strain and ΔT is the change in the temperature. Six FBGs were put on the hanger cables. A reference athermal packaged FBG sensor was also put on the hanger cable. The measured history of one of the FBG sensors along with the reference FBG sensor is shown in the Figure 2.29. It shows that the train passed at 307 s and 370 s and both the peaks can be clearly detected from the response. FBG sensors were mounted on rocker bearings too. The measurement history of one hour of both FBG and conventional strain gauge was compared (Figure 2.30).
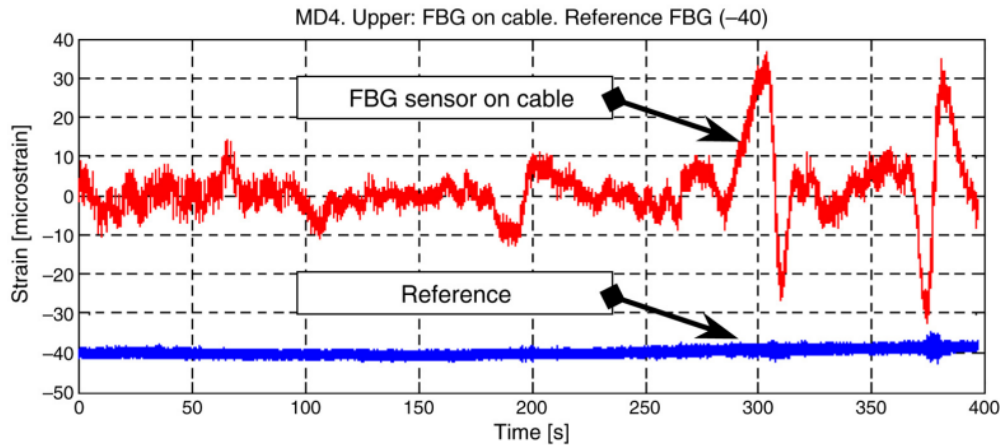
Figure 2.29: Hanger cable tension measurement history [67].
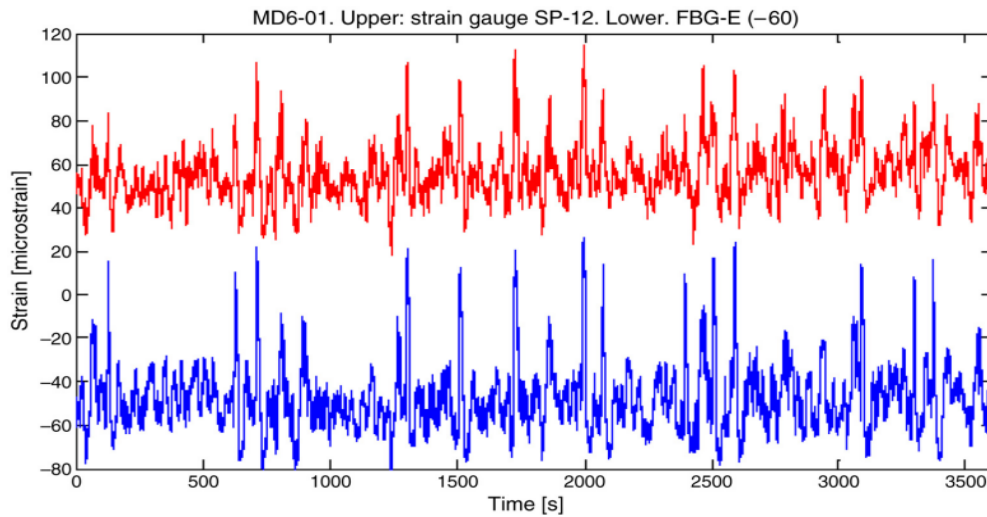
Figure 2.30: Comparison between FBG (lower) and conventional (upper) strain gauges installed on rocker bearings [67].

Though FBG and strain gauge both were not mounted at the same location, the responses from both the sensors are almost similar and the train passages can be clearly detected. 21 FBGs as an array were installed at different places of Chainage 23488 as shown in the Figure 2.31. The signal from FBG sensor is compared with the signal from strain gauge in the Figure 2.31. Thus, FBG sensors can clearly and accurately detect dynamic strain signals. The results from FBG are in excellent agreement with those of conventional strain gauges.
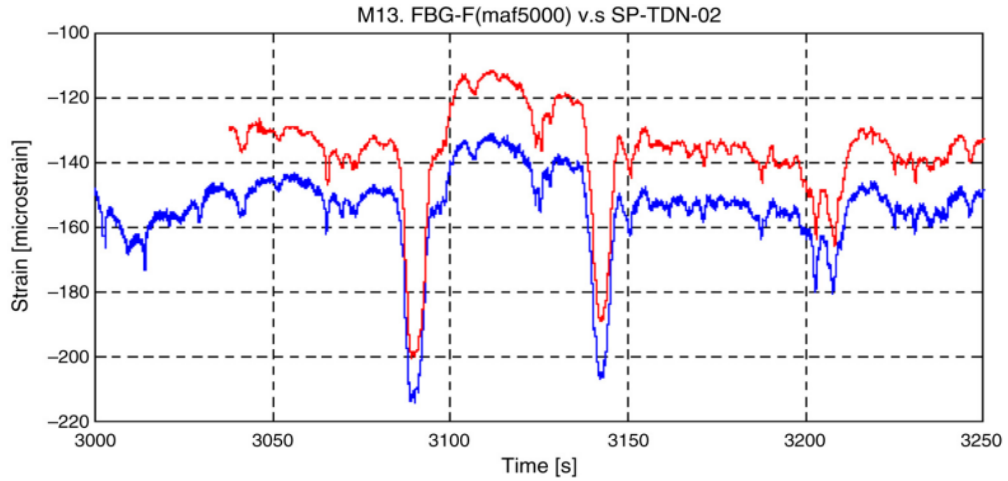
Figure 2.31: Comparison between FBG (upper) and conventional strain gauge (lower) histories [67].

A multiplexed network of FBG sensors was used for SHM of an X-38 aircraft. This FBG network was used for temperature measurement ranging from -40° to 190° and for strain measurement ranging from -0.1% to +0.3%. Thermal and mechanical loads were also monitored successfully [125].

2.7.4 FBG for remote SHM in areas with limited access

An automated FBG system was presented which featured an edge filter demodulation scheme with wavelength multiplexing and GSM based data transmission [69]. Four sensors were installed at various locations on the Northwest transepts of cathedral of Como as shown in Figure 2.32. These locations were chosen due to the presence of large cracks and areas that had already undergone repair. All the four sensors were surface mounted and each consists of two FBGs; one active FBG to measure displacement and second passive FBG to measure temperature. The temperature and displacements were monitored for a period of 8 months as shown in the Figure 2.33. The measurements were taken at about 4-6 weeks intervals.
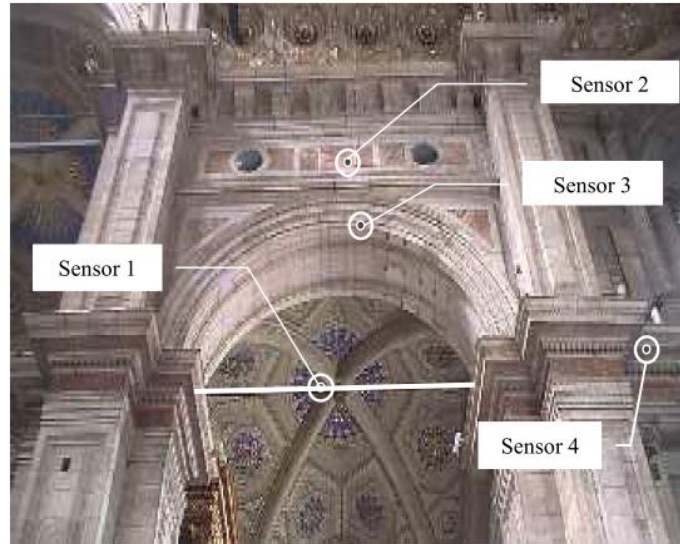
Figure 2.32: Location of the four sensors mounted on and around the test arch in the Northwest transepts of the cathedral [69].
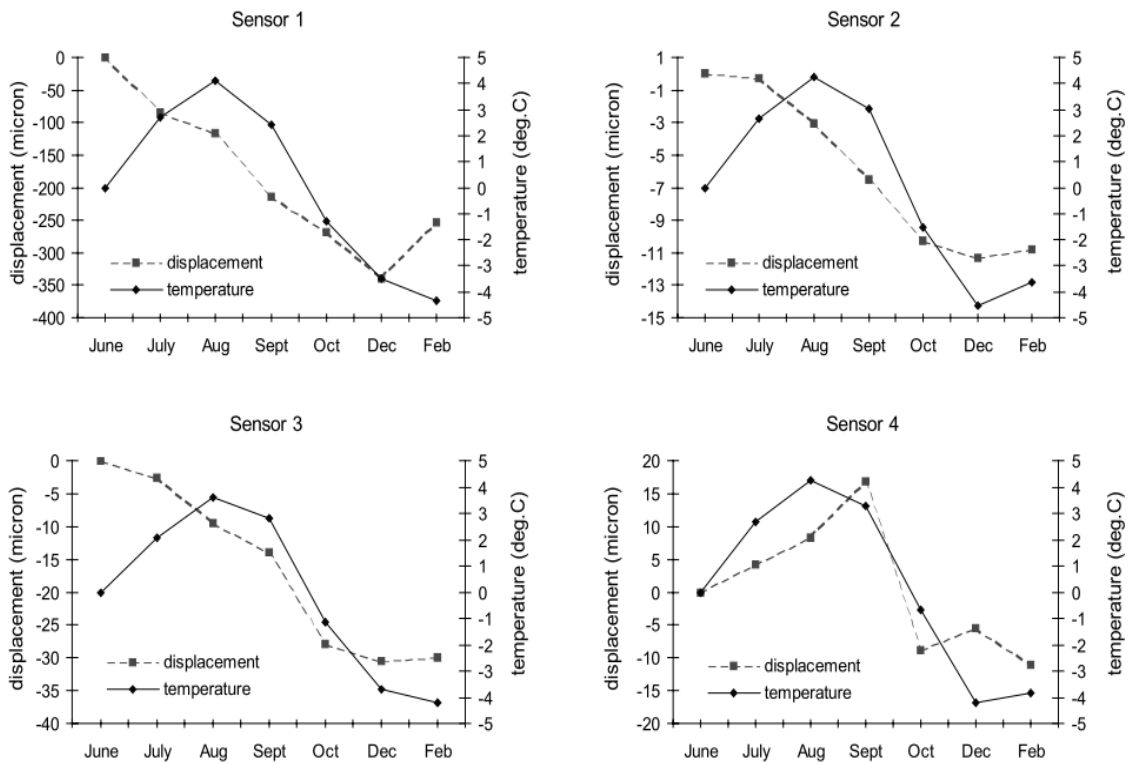
Figure 2.33: Temperature and displacement data from all sensors acquired over an 8-month period [69].

2.7.5 FBG for local health monitoring of tendons and ligaments in the knee

Fiber Bragg grating (FBG) sensors could also be used for measurement of strain in ligaments, tendons etc. There are some advantages that FBG provides over other

conventional sensors like, ease of implementation, low cost, increased accuracy etc. These sensors were used to monitor the strains in tendons and ligaments in different postures and locomotion. The elongation of an Achilles tendon specimen was monitored by the FBG displacement sensor and with a two-camera stereo vision sensor simultaneously. Both the sensors were mounted on the surface of a 10 cm section of a cadaver Achilles tendon by cyanoacrylate. Results are compared in Figure 2.34 [70].
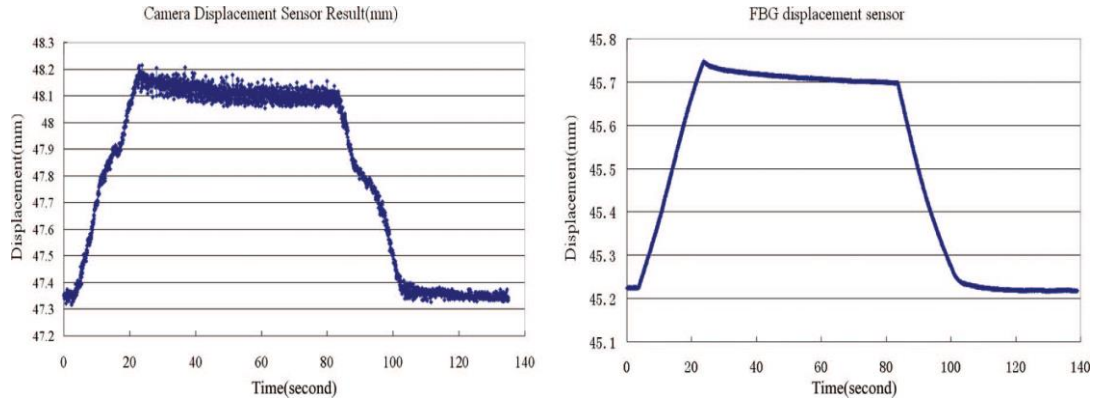
Figure 2.34: Comparison of measured tendon elongation of the FBG sensor and camera stereovision sensor [70].

Clearly, the noise is reduced to a great extent in the measurement by the FBG displacement sensor. It is visible too, that the FBG displacement sensor is more sensitive than the camera displacement sensor. The two FBG sensors were mounted on the medial and lateral collateral ligaments of a human cadaver using cyanoacrylate adhesive (Figure 2.35). A load of 40 N was applied to both the medial and the lateral compartments of the knee joint for approximately 15 seconds and after that the knee was returned to its original position. The deformation experienced in the inside and the outside ligaments are shown in the Figure 2.36. The Figures 2.36(a) and (b) clearly show that the deformation of the inside (medial) ligament is larger than the outside (lateral) ligament and the ligament strain is increased when joint loading is applied in horizontal posture.
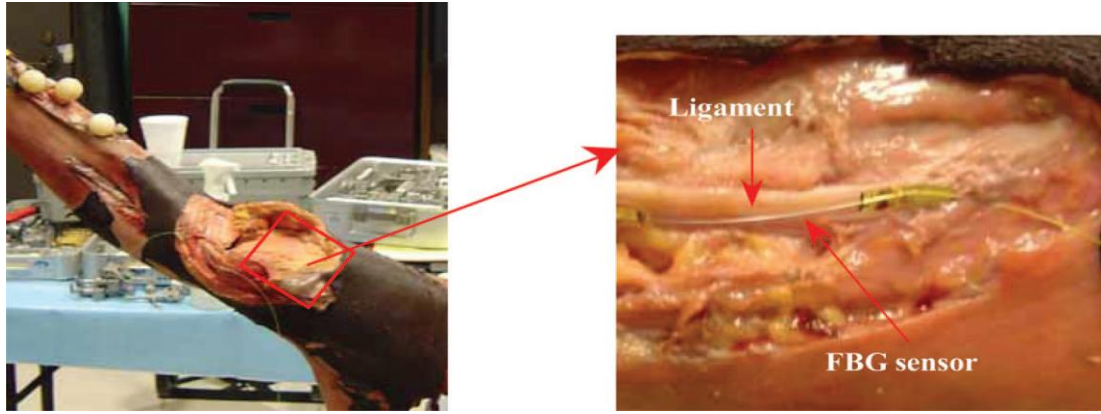
Figure 2.35: Specimen with surface-mounted FBG sensors in the ligaments [70].

(a)   (b)
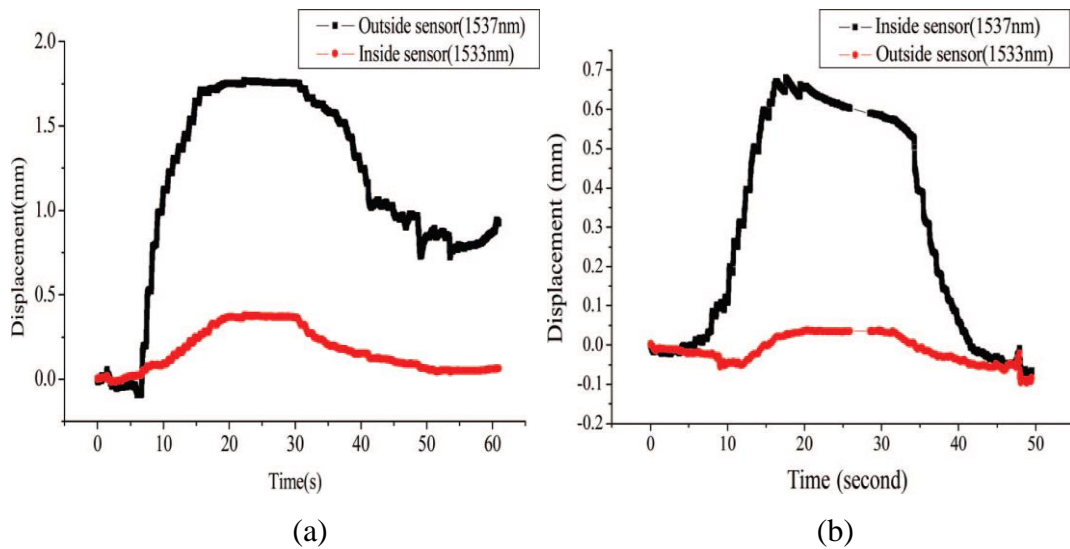
Figure 2.36: Results of FBG sensors when the specimen was in (a) horizontal position
(b) a vertical position [70].

2.7.6 FBG for health monitoring of prosthetic knee during surgery

In 2006, fiber Bragg grating (FBG) sensors were used for pressure mapping of a prosthetic knee joint and for pressure mapping during total knee arthroplasty. A chirp grating was used for the determination of the magnitude and location of load simultaneously. The chirp grating was embedded into the condylar grooves made of composite material. The sensor took the shape and curves of the condylar grooves in the tibial spacer. The embedded sensors were attached on both sides with a thin layer of silicon rubber (Figure 2.37). A mixture of PMMA was used to coat the whole sensor. Both grooves had 46 sub-gratings (23 each) acting as sensing points. The sub-gratings were spread in a matrix structure in each groove [71, 72]. The effects of different loading conditions on one condylar groove in the tibial spacer sensor are

40

shown in the Figure 2.38. The Figures 2.38(a)-(d) are MATLAB patterns generated from the measured wavelength shifts. Figures 2.38 (a) and (b) show that the spread of the force increases when the vertical loading is increased from 25 N to 55 N. Clearly, the spread of the force lies beyond the actual contact area which could not be seen with the existing sensor.
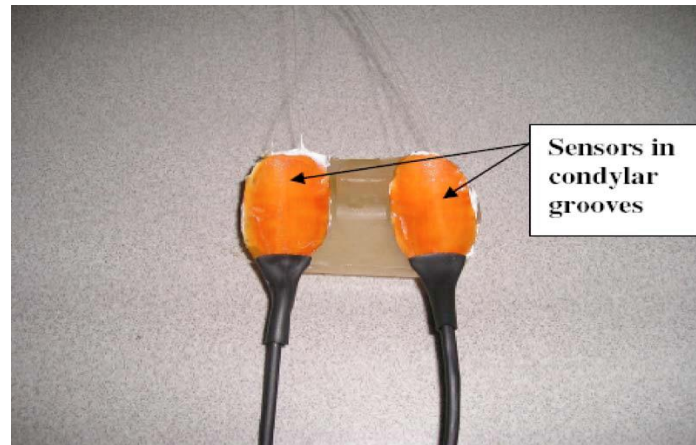
Figure 2.37: The two condylar grooves with embedded fiber gratings [72].
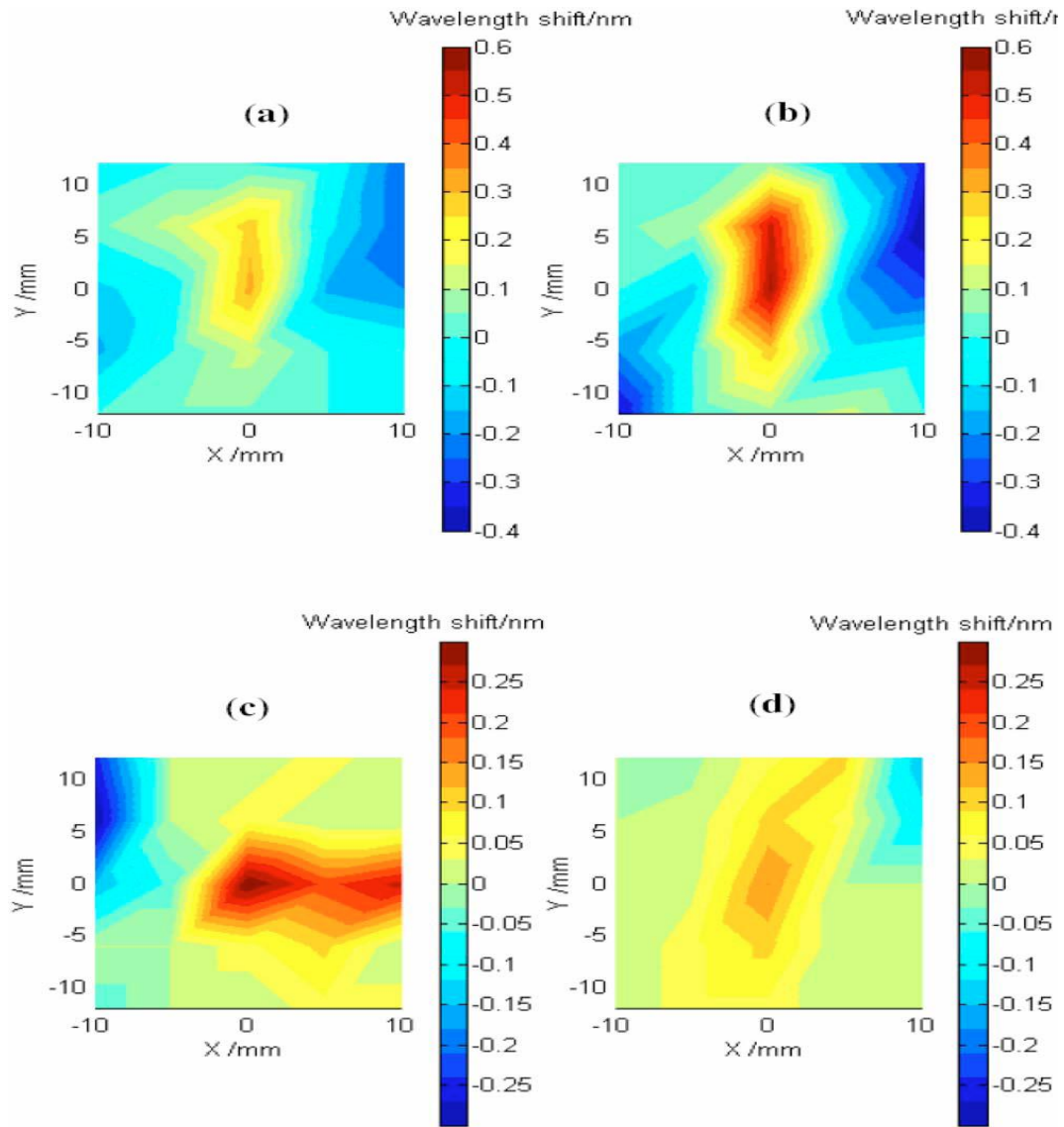
Figure 2.38: The spread of wavelength shifts at (a) 25 N of vertical loading; (b) 55 N of vertical load; (c) The loaded femoral implant being severely tilted towards the right edge; (d) The femoral implant axis being rotated by 5–10 deg. [71].

Also the sensor, made of fiber Bragg grating arrays, was embedded into the tibial spacer to study alignment and distribution of contact stress in extension and flexion of a cadaveric knee. The sensor was inserted in the knee as shown in the Figure 2.39. The pressure maps of one condyle at different angles are shown in the Figure 2.40. From Figure 2.40 it could be seen that at various angles of flexion (from 70° to 40°), the contact region changes. Figure 2.41 shows the pressure map for the medial and lateral condyles of a cadaveric knee. The pressure distribution is unequal in the condyles. From the pressure map it could be seen that the contact for the left condyle is towards the posterior edge, whereas, for the right condyle it is towards the center.

(a)   (b)
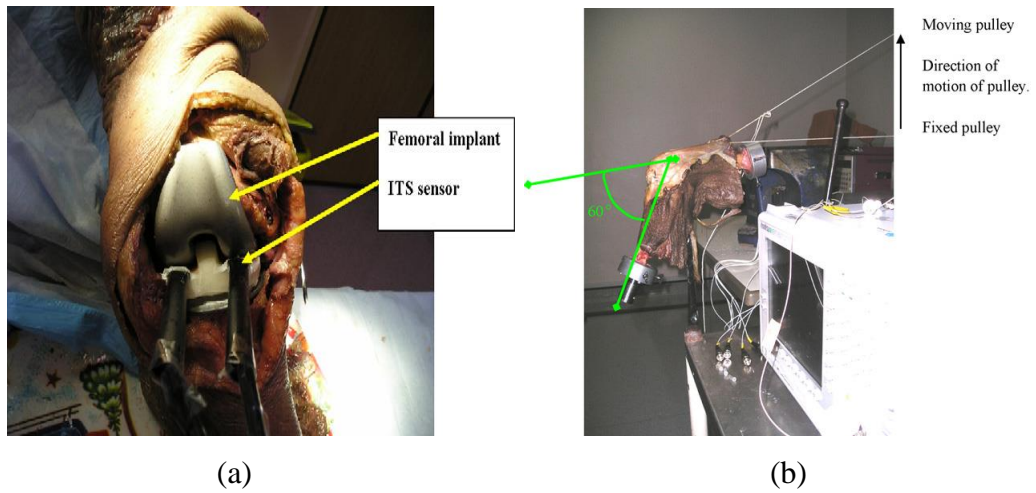
Figure 2.39: (a) A picture of the cadaveric knee joint with the fiber optic sensor inserted and (b) The picture shows a cadaveric knee setup at 60◦ flexion with the sensor sutured inside. The optical spectrum analyzer is in the foreground [72].
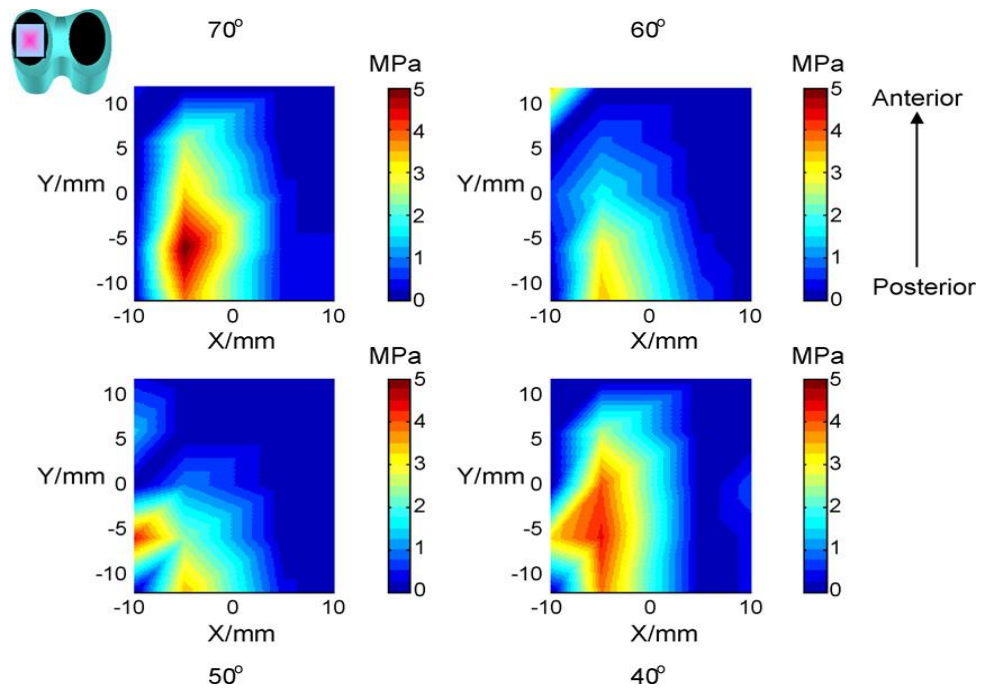
Figure 2.40: Pressure maps of one condyle at various angles of flexion: 70◦, 60◦, 50◦ and 40◦. The icon in the left corner denotes the actual region covered by the pressure map (rectangle) in the tibial spacer. The condylar regions are denoted by the ellipses.
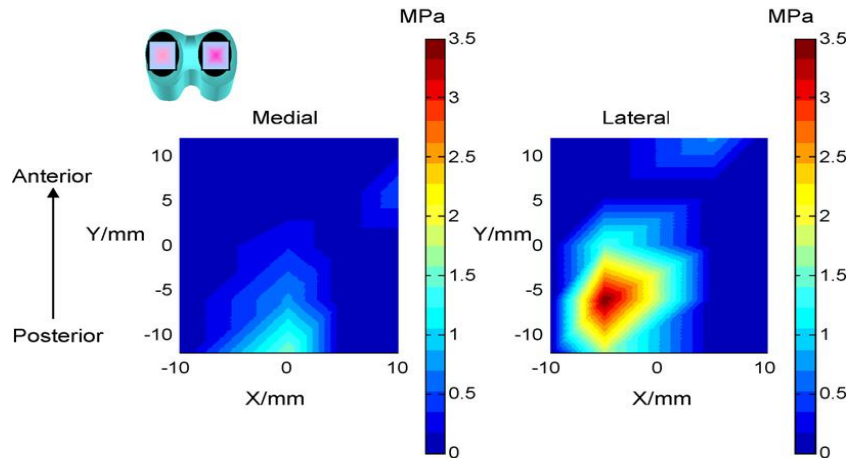
Figure 2.41: Pressure maps of the lateral and medial condyles of one knee in extension. The icon in the left corner denotes the actual region covered by the pressure map (rectangle) in both the grooves of the tibial spacer. The scale bar is in MPa [72].

2.8 Determination of crack location by FOS using Optical Time Domain Reflectometry (OTDR)

When light is launched into the fiber, a part of its intensity is always reflected. OTDR depends on this reflected light. It is possible to obtain the value of the light intensity along the whole fiber by measuring the time of flight of the returned pulses using the OTDR technique. OTDR utilizes the phenomenon of backscattering of light. Thus, it is possible to detect losses in the fiber and to locate these losses with quite good spatial resolution [73].

For the reliable detection and monitoring of cracks in concrete structure like, dam, a sensor was developed by the researchers at the Massachusetts Institute of Technology and Brown University. The sensor is based on a distributed optical fiber micro-bending sensor. An optical fiber was embedded in the concrete element in a ''zigzag'' shape as shown in the Figure 2.42. Using OTDR equipment, the light intensity distribution along the fiber was measured [73, 74].
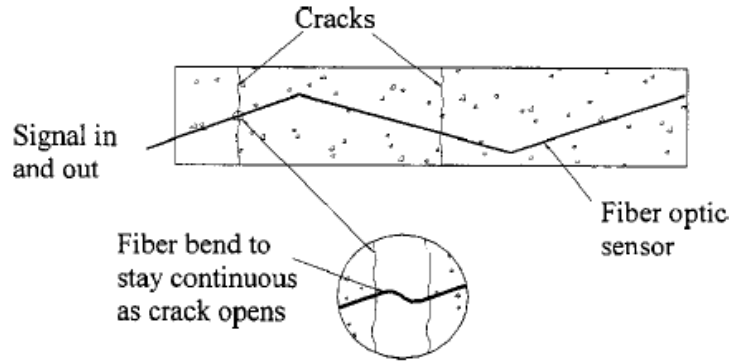
Figure 2.42: Principle of operation of the zigzag sensor [73].
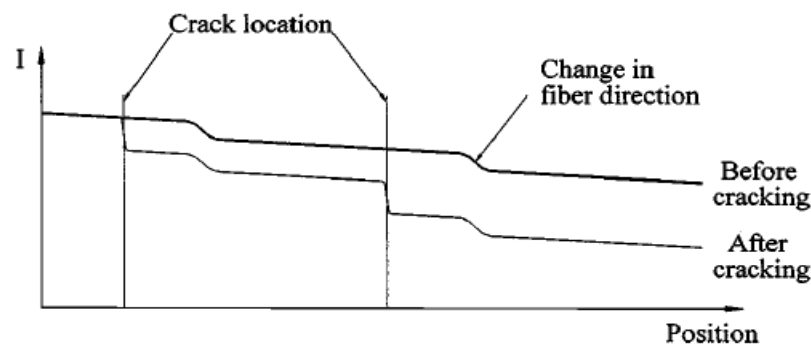
Figure 2.43: Intensity along the fiber, measured by means of the optical time-domain reflectometry equipment [73].

When there is no crack, the intensity of the backscattered signal follows relatively smooth curve (upper curve in Figure 2.43). There are only small losses of intensity at the bending of the fiber and it depends on the radius of curvature of bending. When a crack opens in the structure, a fiber intersecting the crack at an angle around 90° has to bend to stay continuous (Figure 2.42). This abrupt bending of fiber causes a sharp drop in the intensity of the optical signal as shown by the lower curve of Figure 2.43. This intensity loss is located and detected by OTDR and thus the crack location could be identified. With the proposed technique most of the cracks could be located, but the cracks must cross the fiber at an angle around 90°. The cracks which do not cross the fiber or cross the fiber at angles almost parallel to the fiber, will be missed out. Based on reflectometry, another fiber optic sensor called Brillouin optical time-domain reflectometer (BOTDR) was used for distributed sensing. BOTDR can measure strain continuously over a distance of 10 Km. It has the capability of detecting deformations

and diagnose problems in large scale structures such as buildings, tunnels, and levees etc. [126].

2.9 Summary

Different FOS techniques have been discussed here so far. EFPI sensors are great for local strain monitoring. The sensitivity and coupling efficiency of EFPI sensors depends on what kind of fiber is being used. If multimode fiber is being used, sensitivity will be low, but the coupling efficiency will be high. On the other hand, if single-mode fiber is used, sensitivity will be high, but the coupling efficiency will be low. The main disadvantage of EFPI sensor is that its diameter is relatively lager and sometimes it is not suitable to embed an EFPI sensor into a structure.

FOCS follow the principle of signal loss due to increase in bending which is damage induced. Apart from this, there can be several other reasons for signal loss, i.e. free fiber bending (extra fiber, which is not attached to the structure), fluctuations in light source power etc. Also, the sensitivity and resolution of FOCS are very low. Also in OTDR, the intensity of the signal is interrogated for damage monitoring. Again, there can be multiple reasons for intensity loss. The intensity losses due to the bending of fiber and the damage are almost the same, so the resolution is very poor.

From the literature available so far it is clear that FOPS is the best among all the fiber optic sensors for global SHM. FOPS can perform global SHM in two ways; static loading test and dynamic loading test. As of now, FOPS have only been studied qualitatively; therefore, FOPS have further scope for quantitative study like, investigation on damage size and location in structures. The other problem with FOPS is that the whole fiber is sensitive and it picks up the other unwanted disturbances which lead to a very unstable output signal from FOPS. FOPS signal needs to be stabilized for a reliable study on damage investigation.

FBG sensors are the most widely researched and implemented among all the fiber optic sensors for local SHM. FBG sensors are highly sensitive and accurate for the measurement of various physical parameters like, strain, temperature, pressure etc. Multiplexing method makes it even more valuable. It would be interesting to look into various ways by which the FOPS and FBG can be combined on a single fiber to get a

better picture (global SHM + local SHM) on the damage scenario in a structure. To be able to do this, both must operate in the same wavelength region. Currently, FBG set up is very bulky and expensive as it employs optical spectrum analyzer (OSA) and a big communication light source. Bringing down FBG's set up cost is another aspect which can be looked at.

CHAPTER 3 FBG for resin pressure measurement in a curing composite laminate for quality optimization

Resin pressure or resin flow measurement is a very important of SHM of a curing composite laminate. In this study, a special purpose FBG sensor is developed for the in-situ measurement of resin pressure. This device uses the principle of differential pressure in liquids. The stability and the reliability of the proposed FBG sensor have been proved. It is concluded that this FBG sensor can be used for the measurement of resin pressure in high temperature and low bleed curing of composite laminates, such as out of autoclave curing.

3.1 Introduction

Fiber optic sensors are one of the latest smart materials. Among all the fiber optic sensors, FBG sensors are being used extensively for various applications. Structural health monitoring (SHM) is one of the important application areas for FBG. Mostly, SHM is performed by tracking the strain at various important points in a structure. The simultaneous measurement of cure induced strain and cure temperature was carried out by using a FBG/EFPI hybrid sensors [107]. The FBGs written on high birefringent fibers were utilized to measure the effective transverse strain (cure shrinkage) of a curing composite [108]. Sometimes other parameters like, pressure, temperature etc. might be of key importance as far as the SHM of some structures is concerned.

FBG sensors were effectively used to investigate the tool-part interaction during the cure process of composite [109]. In resin infusion process the embedded FBGs were used to identify the resin flow front in addition to the process strain and health monitoring of the infused parts [110, 111]. Recently, to quantify the spring-in distortion of a complex L-shaped structure, a 'non-axisymmetric strain' measurement technique was proposed in which the birefringence effect of the FBG was utilized [112]. The FBGs directly embedded between the plies could be used for the life cycle monitoring of the composites, starting from process monitoring to the damage detection. These embedded FBG can also be used to measure the applied compaction pressure through the transverse strain measurement.

However, the embedded FBG sensors cannot be used to measure the liquid resin pressure inside the curing composites. Resin pressure distribution of a curing laminate is the key parameter that controls the strength, stiffness and void nucleation of the cured part. It is vital to monitor and control the resin movement of the curing laminate to optimize its quality with any manufacturing process [123, 124]. The gradient of resin pressure inside a curing composite dictates the constituent's volume fraction, void migration and eventually, the quality of the laminate. In other words, resin pressure measurement is important for health monitoring of curing composite laminates. Therefore, it is imperative to monitor the resin pressure all through its curing process in order to be able to optimize the quality of the laminate. Ultrasonics [113], dielectric sensors [114] and fiber optic sensors [115] were used to detect the resin flow-front and to optimize the process. These sensors were embedded in dry fiber fabrics and the resin was infused to saturate the fabrics. However, the above said sensors are not suitable for prepreg laminate because it involves the usage of fibers fully impregnated in resin (prepreg) to achieve higher fiber volume fractions. Hence, in prepreg laminate, the resin flow takes place in a fully saturated medium. Since resin movement is slow through porous fiber beds, it is considered to be laminar with low Reynolds number. In such resin saturated medium, externally applied compaction pressure is shared by both resin and fiber.

To measure the hydrostatic resin pressure an attempt was made [116] with stamp-sized flat sensors. Unfortunately, these sensors provided only the quantitative information about the resin pressure owing to the noise issues. A different pressure sensing device based on the principle of pressure transfer in liquids was demonstrated [117]. The response of this device for no bleed and low resin flow conditions was not satisfactory and needed further improvement. Also, the sensitivity and stability of this device for high temperature curing (>120 ^{0}C) composites was questionable.

A dual purpose FBG sensor with a pressure sensitivity of $2.02 \times 10^{-6} MPa^{-1}$ was proposed to measure hydrodynamic pressure and temperature [97]. The pressure/load sensitivity of a bare FBG along transverse direction being inconspicuous was amplified by converting transverse strain into axial strain and the sensitivity was improved to $2.2 \times 10^{-2} MPa^{-1}$ [118]. In this method, the liquid pressure was

transformed into axial strain in the FBG with the help of elastic polymers. The mechanism was such that a lateral pressure applied to the polymer extended the FBG axially. Another FBG sensor with a fused-silica head was developed to measure the pressure and temperature of geothermal wells [119]. A hydrostatic pressure sensor with a hollow cylinder partially filled with silicone rubber was designed to measure liquid level in storage tanks [120, 121]. These FBG sensors measured the liquid pressure only if they were immersed in the water; hence, the measurement was affected by dynamics of liquid. Therefore, the polymer encapsulated FBG pressure sensors are not preferred for the regions where the accessibility is poor and the pressure is high and dynamic.

In this work a special purpose FBG device is designed and fabricated to measure the hydrostatic resin pressure with improved sensitivity and reliability. The proposed FBG sensor device measures liquid pressure in such a way that it need not be immersed in the liquid. This sensor is designed to measure the hydrostatic resin pressure of curing composites under high temperature and diverse pressure conditions in particular.

3.2 Theory and device development

The FBG is inscribed on the core of the fiber with the help of a phase mask and laser beam (Excimer laser 248 nm). The Bragg wavelength reflected by an FBG is given as

$$\lambda_B = 2n_{eff}\Lambda \tag{3.1}$$

where n_{eff} is effective refractive index and Λ is the grating period. The relation between the change in Bragg wavelength and the corresponding axial strain in an FBG is given by

$$\frac{\Delta\lambda_B}{\lambda_B} = (1 - p_e)\varepsilon_z + (\alpha_s + \xi)\Delta T \tag{3.2}$$

where $p_e = 0.22$ is the fiber photo elastic constant, α_s is the coefficient of thermal expansion of silica fiber and ξ thermo-optic co-efficient [1, 121]. The schematic diagram of the newly proposed FBG sensor for hydrostatic pressure measurement is shown in Figure 3.1.
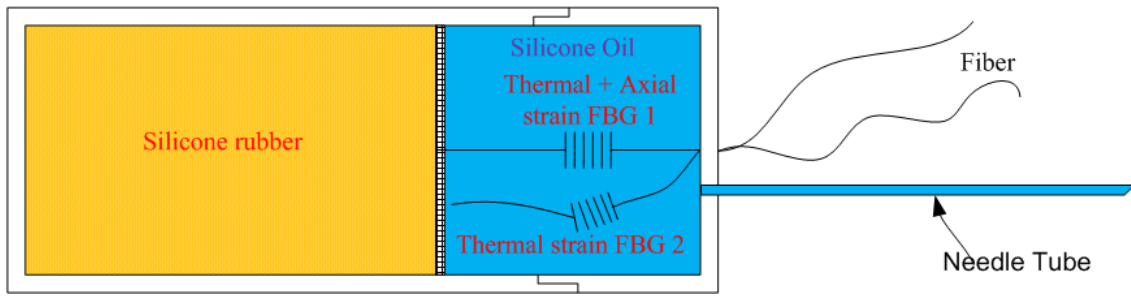
Figure 3.1: Schematic diagram of newly proposed FBG sensor for hydrostatic pressure measurement.

A hollow cylinder with one end closed and the other end enclosed with a cap was made from a stainless steel hollow rod. To hold the pressure sensing FBG fiber along the axis of the cylinder, a hole of 1 mm in diameter was drilled in the center of the cap. Another hole of 1.5 mm diameter was drilled at a distance of 2.5 mm from the center of the cap to accommodate a needle tube of 1.4 mm in diameter. A stable and inert silicone rubber was partially filled in the cylinder. Further, a round metal plate (thickness 0.2 mm) was glued to the silicone rubber. One end of FBG was glued to this metal plate through a small hole at its center. The other end of FBG passes through the center hole of the cap and the fiber was glued to the cap around this center hole as shown in Figure 3.1. Non-reactive high temperature silicone oil was filled in the empty portion of the cylinder through the needle tube to avoid a direct contact between the FBG and the epoxy (resin). The second FBG (FBG2) was left free inside the cylinder to measure the temperature induced Bragg wavelength shift only. This is used as a temperature compensator for the pressure sensing FBG1. The fabricated FBG sensor proposed in this research work is shown in Figure 3.2. The spectrum of both the FBGs (FBG1 and FBG2) used in this pressure sensing device is shown in Figure 3.3.

Figure 3.2: Fabricated FBG Sensor
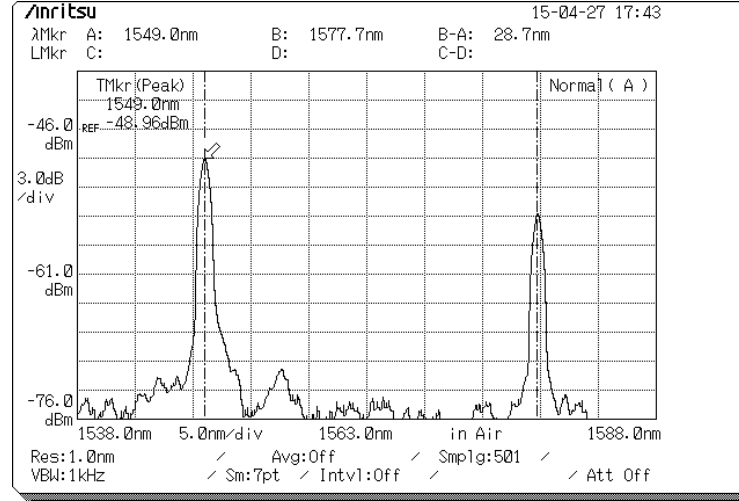
Figure 3.3: The spectrum of the dual FBG sensor.

The proposed FBG sensor is designed to measure the hydrostatic liquid pressure. The tip of the needle tube is put at a certain point in the liquid where the hydrostatic pressure has to be measured. When the needle tube of the sensor is put in the liquid, it enters the tube and builds up pressure on the silicone oil and that pressure is finally exerted on the silicon rubber resulting in axial compression of silicon rubber. In this FBG sensor design, the hydrostatic pressure compresses the silicone rubber axially rather than radially as was case for lateral pressure sensors [120, 121]. Thus, an axial strain is exerted on the pressure sensing FBG (FBG1 in Figure 3.2) in response to the hydrostatic pressure. A relationship between the liquid pressure (P_l) and the axial strain experienced by the FBG is given as

$$\varepsilon_z = \varepsilon_f = \varepsilon_R = \frac{P_l}{E_f \left(\frac{A_f}{A_R}\right) + E_R \left(\frac{L_f}{L_R}\right)} \tag{3.3}$$

where L_f and L_R are the lengths, A_f and A_R are the cross sectional areas and E_f and are the elastic coefficients of the FBG (glass fiber) and silicone rubber respectively ($E_f = 70$ GPa, $E_R = 127.55$ MPa). At constant room temperature ($\Delta T = 0$), the equation (3.2) and equation (3.3) could be rewritten as

$$\left(\frac{\Delta\lambda_B}{\lambda_B}\right)_P = (1 - p_e)\frac{P_l}{E_f\left(\frac{A_f}{A_R}\right) + E_R\left(\frac{L_f}{L_r}\right)} \tag{3.4}$$

3.3 Experiments and Results

3.3.1 Calibration of the sensor (FBG1) at room temperature

The sensitivity of the proposed FBG sensor was calibrated through water column experiment. The experimental set up for this is shown in Figure 3.4. In this experiment, the needle tube of the FBG sensor was introduced into the bottom of a liquid column. The water enters the tube and the hydrostatic pressure is exerted on the silicon rubber. This pressure compresses the silicon rubber. This in turn produces axial strain in the FBG1. The liquid pressure P_l exerted at the bottom of a water column of height H is given as

$$P_l = \rho_l g H \tag{3.5}$$

where ρ_l is the liquid density and g is the gravitational constant. Equation (3.4) and equation (3.5) can be rewritten as

$$\left(\frac{\Delta\lambda_B}{\lambda_B}\right)_P = (1 - p_e)\frac{\rho_l g H}{E_f\left(\frac{A_f}{A_R}\right) + E_R\left(\frac{L_f}{L_r}\right)} = k_p(\rho_l g H) \tag{3.6}$$

where k_p is called the pressure sensitivity of the proposed FBG sensor [97, 118].
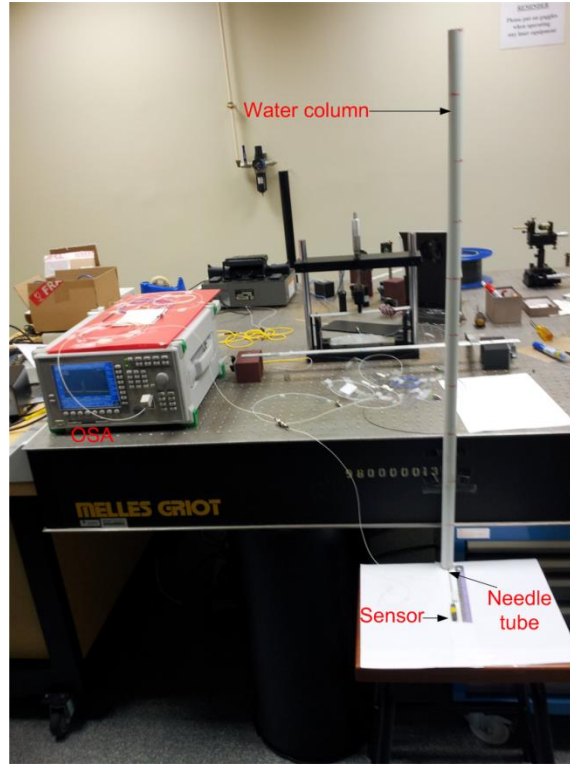
Figure 3.4: Experimental set up for proposed FBG sensor calibration.

As the water level increases, the corresponding hydrostatic pressure increases linearly at the bottom of the water column. As a result the compression in silicon rubber increases linearly. Hence, the axial strain experienced by the FBG1 increases linearly with increasing water level or in other words the Bragg wavelength shift increases linearly with increasing water level. The theoretical shift in Bragg wavelength due to a particular hydrostatic pressure is calculated by equation (3.6). The theoretical and the experimental shifts in Bragg wavelength are compared in Figure 3.5. Both (theoretical and experimental Bragg wavelength shifts) are linear with hydrostatic pressure exerted on the bottom of the water column. The sensitivity (k_p) of the proposed FBG sensor is calculated using equation (3.6). Experimentally, the pressure sensitivity of the proposed FBG sensor was measured to be $1.636 \times 10^{-2} MPa^{-1}$. Theoretically, the pressure sensitivity was found to be $1.4266 \times 10^{-2} MPa^{-1}$. Both the pressure sensitivity values are more or less the similar.
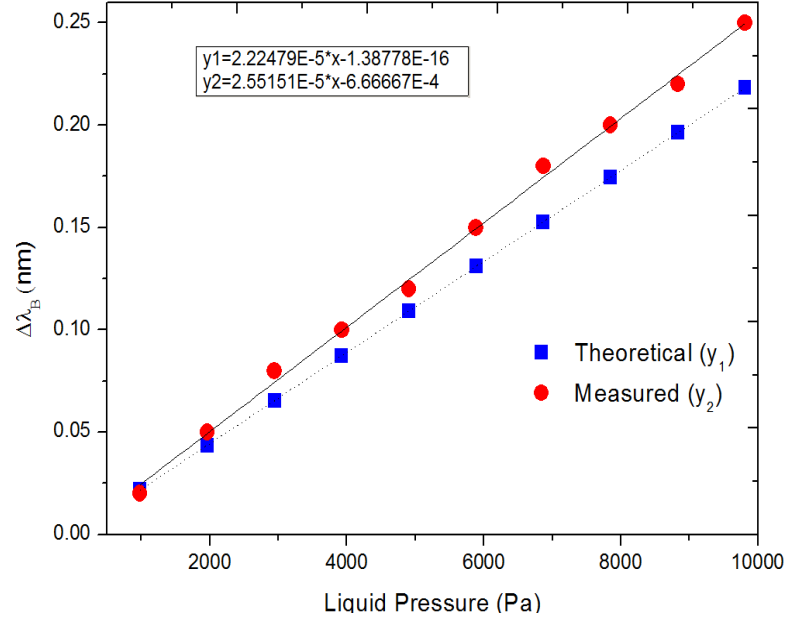
Figure 3.5: Response of the sensor at room temperature (27°C).

In Figure 3.5, there is a deviation between experimental and simulation data, especially, the larger deviation in the higher liquid pressure. The simulated Bragg wavelength shift ($\Delta\lambda_B$) is calculated by using standard values of elastic coefficient of fiber glass and silicon rubber (E_f and E_R). Also, cross-sectional areas of the fiber core and silicone rubber (AF and A_R), lengths of fiber and silicon rubber (L_f and L_R) are used to simulate the Bragg wavelength shift. All these values may not be exactly the same in reality as were used for simulation purpose. A slight deviation will lead to a difference between experimental and simulation data. Initially at lower pressure, this difference might be very small, but it is supposed to get widened on higher pressure values. The repeatability of the sensor was confirmed by repeating the experiments three times. These results are shown in Figure 3.6. The average standard deviation for these three trials is 0.007 nm. This is due the sluggish movement of the silicone oil once it is disturbed from still. Therefore, a settling time for the silicone oil should be allowed before starting next experiment. In Figure 3.6, most of the data points of trial 1 and trial 3 are exactly the same. The data points of trial 2 are also not too different, except for the last point. These trials were conducted using the highest available resolution (0.1 nm) of OSA. At such low resolution, the peak value of Bragg reflection oscillates within the limit of resolution. In such cases, the value which stays the most is considered which might contribute to error to some extent. Also, a slight tilt of the

water column will reduce the effective height of water level, which might be the case for trail 2.
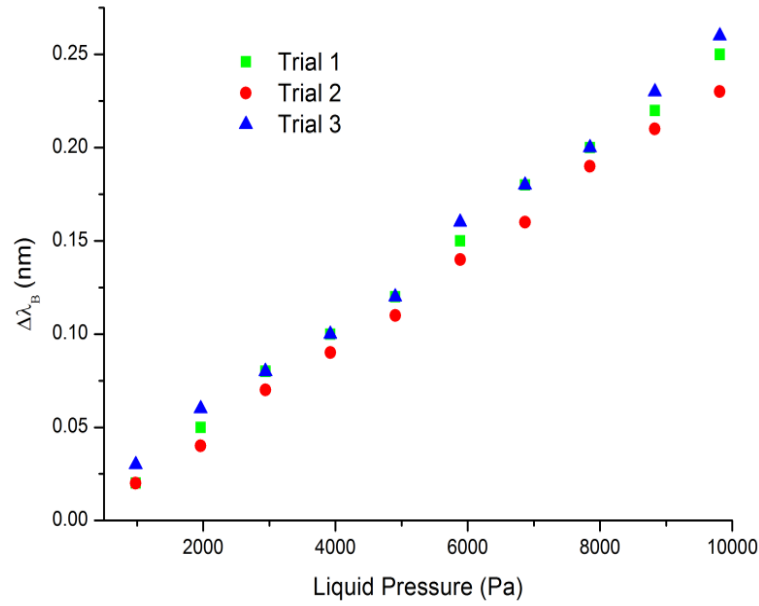
Figure 3.6: Three trials showing the repeatability of the sensor.

3.3.2 Resin pressure measurement

The FBG sensor developed in the current work was further used to monitor the hydrostatic resin pressure of a high temperature curing epoxy prepreg laminate. The needle tube was inserted in the center of the prepreg lay-up and then it was cured in a convection oven the schematic of which is shown in Figure 3.7. As the temperature increases the prepreg resin transforms into liquid and balances a part of the applied load as hydrostatic pressure. This pressure is sensed by the FBG1 and the corresponding resin volume fraction could be obtained at specific locations of the curing composite. A temperature compensation technique was adopted to separate the temperature and pressure induced Bragg wavelength shifts of the FBG1. This is done by placing FBG2 inside the cylinder with one of its ends left free. Thus, it is possible to measure the oven temperature near the laminate and the resin pressure at the center of the curing laminate concurrently.
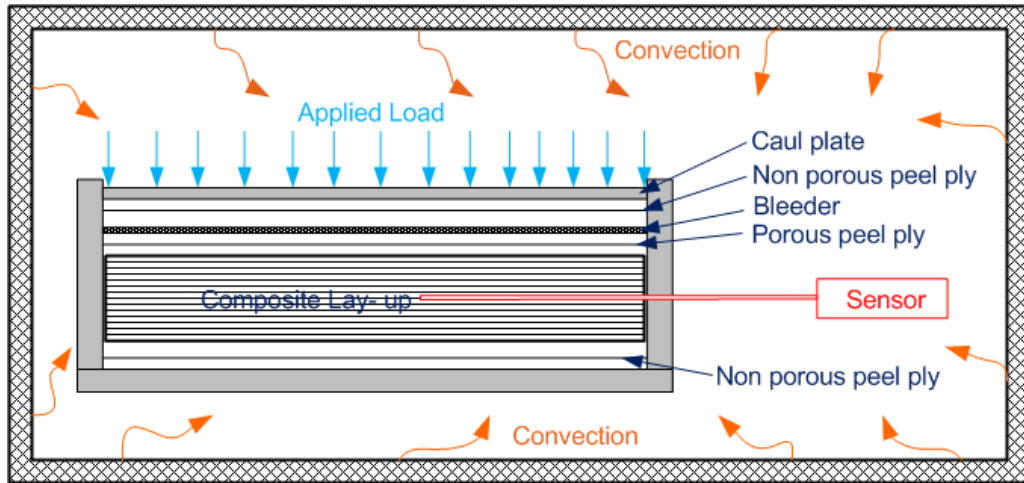
Figure 3.7: Schematic of the fabrication set up and materials used in the experiment.

The actual experimental arrangement for in-situ resin pressure measurement is shown in Figure 3.8. The unidirectional prepreg plies (Glass/epoxy) of size *100 mm X 100 mm X 0.25 mm* were laid up in an aluminum fixture with a square cut-out of the same size. There were fifty plies in the prepreg lay-up with thickness of 0.25 mm each. Hence, the total thickness of the laminate was 12.5 mm and the needle tube was inserted at a thickness of 3.5 mm from the bottom of the lay-up. A hole was drilled in the center of a cut-out edge of the aluminum fixture which is perpendicular to the fiber direction as indicated in Figure 3.7. The sensor's needle tube was inserted into the laminate through this hole to locate the tip of the needle exactly at the center of the laminate. Non-porous peel plies were used to separate the aluminum fixture and laminate easily. A bleeder cloth was placed on the top of the laminate to facilitate the resin flow in the transverse direction of the laminate. A porous peel ply was used to separate the bleeder cloth from the prepreg lay-up. Even though the size of the square cut-out of the fixture and the prepreg plies are same a small gap exists between the lay-up and fixture sides as shown in Figure 3.8. This gap contributes to an edge resin flow along the fiber direction. This entire set-up was put in the convection oven and the laminate was cured at the manufacturer's recommended temperature (Figure 3.10) with a compaction pressure of 29.43 k Pa. These measurements are detailed in the subsequent sections.
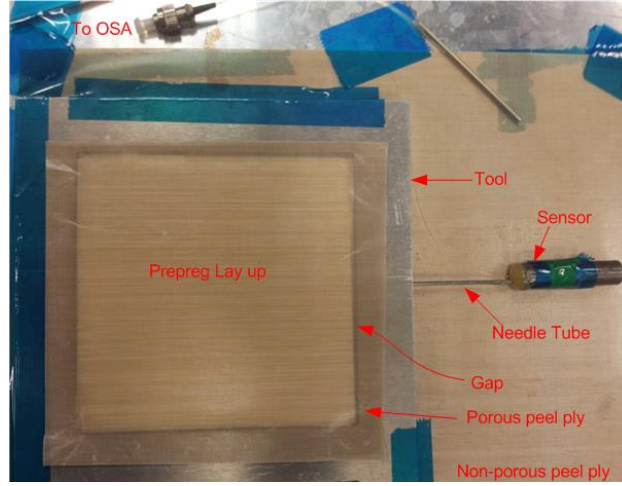
Figure 3.8: Actually assembled set up and materials used in the experiment.

As stated earlier, the FBG sensing device proposed in this experiment carries two
FBGs. The FBG1 was glued between the cylinder's cap and the circular metal plate
which was fixed on the silicon rubber. FBG1 measures the Bragg wavelength shift
induced by hydrostatic resin pressure and temperature rise both as given by the
equation below

$$\left(\frac{\Delta\lambda_B}{\lambda_B}\right)_{FBG1} = \left(\frac{\Delta\lambda_B}{\lambda_B}\right)_P + \left(\frac{\Delta\lambda_B}{\lambda_B}\right)_T \qquad (3.7)$$

The Bragg wavelength shift measured by FBG2 is due to the temperature rise alone, it
is described as

$$\left(\frac{\Delta\lambda_B}{\lambda_B}\right)_{FBG2} = \left(\frac{\Delta\lambda_B}{\lambda_B}\right)_T \qquad (3.8)$$

Therefore, the Bragg wavelength shift (FBG1) due to the resin pressure could be
obtained as

$$\left(\frac{\Delta\lambda_B}{\lambda_B}\right)_P = \left(\frac{\Delta\lambda_B}{\lambda_B}\right)_{FBG1} - \left(\frac{\Delta\lambda_B}{\lambda_B}\right)_{FBG2} \qquad (3.9)$$

The wavelength shifts measured by the both FBGs and the wavelength shift due to the
hydrostatic resin pressure alone are shown Figure 3.9. As the oven temperature rises,
both FBGs measure the same change in Bragg wavelength up to a temperature rise of

90°C. At this temperature a sudden difference in the wavelength shift was observed as shown in Figure 3.9. The wavelength shift of FBG1 is higher than that of FBG2 due to the liquid resin that pressurizes the FBG1 until the gelation of resin is reached. After gelation, the wavelength shifts of both the FBGs are identical again till the end of the cure.
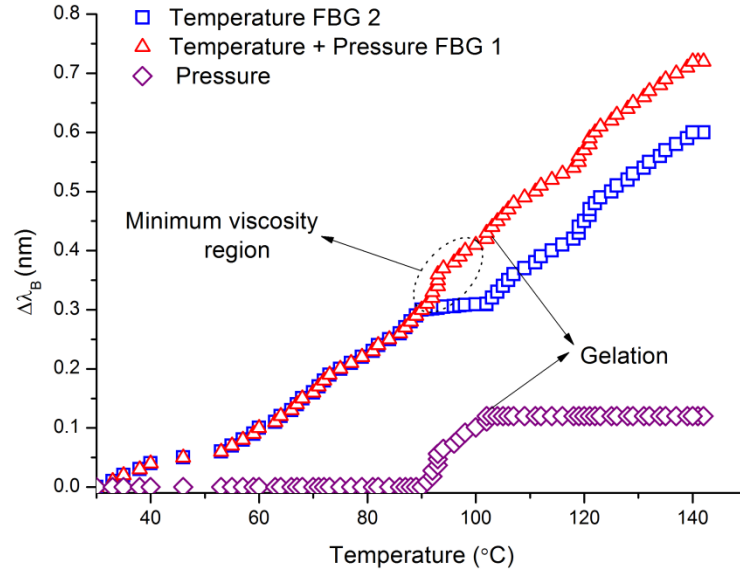
Figure 3.9: Shift in the Bragg wavelengths of FBG 1 and FBG 2 due to temperature & pressure both (red) and due to temperature only (blue), respectively.

Initially, the prepreg was a semisolid (B-stage) with the fiber volume fraction of 0.54. Therefore, no difference between the Bragg wavelength shifts of the two FBGs was observed during the initial stages of curing. As the temperature ramps up (2 ^{0}C/min), the viscosity of the resin drops to a minimum value. At 90°C, the entire resin becomes liquid which carries a part of the applied compaction pressure. This liquid enters the needle tube and the exerted pressure is transferred to the sensor (FBG1) and it induces a sudden rise in the Bragg wavelength of FBG1. This sudden shift in Bragg wavelength is converted to the corresponding pressure values as described in equation (3.5) and equation (3.6). The resultant hydrostatic resin pressure development for the given temperature cure cycle along with the viscosity profile is shown in Figure 3.10. The viscosity profile could be obtained for the same temperature cure cycle using rheometer. After the gelation of resin, the liquid resin that entered the tip of the needle blocks it. This is why the pressure sensed by the FBG1 was constant after gelation.

Since the fiber volume fraction is high enough, the total pressure applied for laminate compaction is shared by both resin and fiber [122]. The applied compaction pressure is very low in comparison with the actual laminate fabrication. Therefore, the resin loss at the center of the laminate is almost negligible. The maximum hydrostatic pressure measured by the FBG1 is 13.315 KPa which is 46 % of the applied compaction pressure.
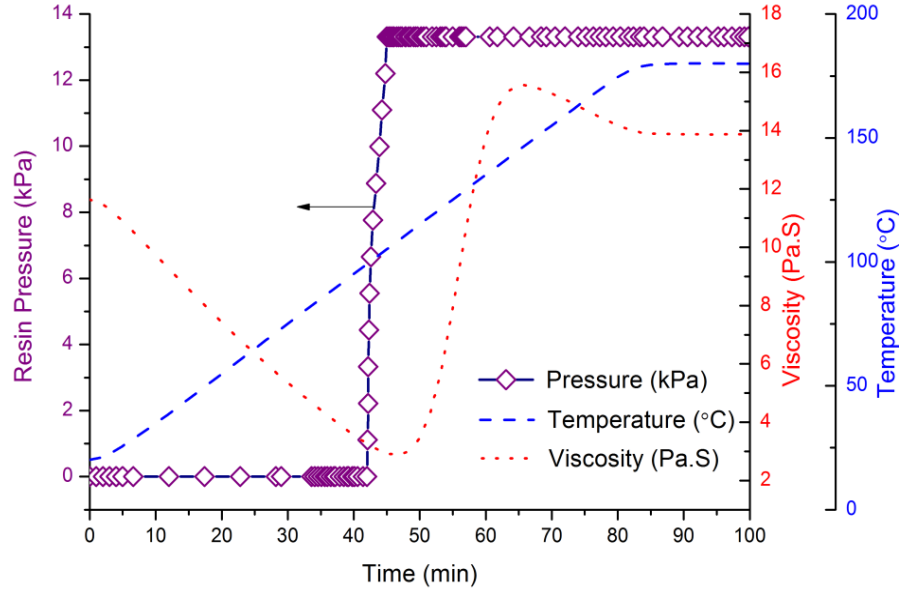
Figure 3.10: Resin pressure, temperature and viscosity variation with time.

3.4 Summary

In this work, a low cost special purpose FBG sensor with needle tubing is designed and fabricated to measure pressure change in liquids. The sensitivity of the sensor is calibrated through a simple hydrostatic pressure measurement experiment using a simple water column. The sensitivity of the sensor is found to be $1.636 \times 10^{-2} MPa^{-1}$ which is higher than the lateral pressure sensors available elsewhere. The reliability of the proposed FBG sensor is confirmed through repeated experiments.

This sensor was further used to measure the hydrostatic resin pressure of a high temperature and low compaction pressure curing prepreg composite laminates (out of autoclave). The measured resin pressure values were numerically validated. This sensor could also be used for resin pressure measurement of autoclave curing

laminates with a compaction pressure not exceeding 0.3 MPa. The length of the silicon rubber must be modified to measure compaction pressure higher than 0.3 MPa.

Therefore, the proposed FBG sensors can be used for the mapping of resin pressure distribution across the entire curing laminate by putting several such sensors at various points in the laminate while it cures. Hence, the strength, stiffness and void nucleation of the cured composites can be controlled using such sensors. In other words, the SHM of curing composites can be performed using FBG sensors proposed in this work. The additional advantage of needle tubing is that these FBG sensors could also be used for liquid pressure measurement where accessibility is difficult, such as geothermal wells and oil pipes.

CHAPTER – 4 Efficient Design of Fiber Optic Polarimetric Sensors (FOPS) for crack location and sizing

A new design of FOPS is proposed and validated. The output of this FOPS is very stable as only the central part of FOPS is sensitive, keeping the "leading-in" and "leading-out" parts insensitive. This design is then implemented to locate and estimate the size of a crack in a cantilever. An experimental study on cracks in Fixed-fixed beams is also presented.

4.1 Introduction

In the field of structural health monitoring (SHM), fiber optic sensors (FOS) play an efficient role and are capable of providing fast and real time monitoring [36, 45, 75-76]. Based on the literature survey presented in chapter 2, FOPS is a strong contender for global SHM among all the fiber optic sensors. FOPS is also used to measure physical parameters such as pressure, strain, twist etc. Recently, a Sagnac interferometer was designed using a specific configuration of Hi-Bi (or FOPS) fibers. It works as temperature and strain independent torsion sensor [77]. The other simple and efficient design of fiber-optic polarimetric twist/torsion sensor was also presented [78].

FOPS have already been tested for dynamic and static global SHM of different structures [35, 79]. The SHM of a localized part (or local SHM) could not be performed using FOPS. The results of tests performed with FOPS so far are not sufficient to predict the actual state of damage in a structure [35, 36]. These results hardly provide with any information which could help in accessing the actual damage state in a structure. Hence, the information given by FOPS is partial and in need of further study. Also, the output signal from FOPS is noisy as it picks up unwanted disturbances readily. Some parts of PM fiber, which transmits and receives the signal are always outside the structure. These extra fibers are also a part of the sensor and therefore pick up spurious signals from its surroundings and add them to the actual signal leading to inaccurate measurements. That is why it is essential that the length of extra fiber be kept short so as to reduce noise in actual signal arising from disturbances

in the fiber outside the region of interest. Thus, SHM tests could not be performed effectively at long distances.

In this research, we present a new FOPS design comprising of three parts; the "lead-in" part, the "active part" and the "lead-out" part [60]. Of the three parts, only the active part (or central) is made sensitive to the structural variations while the rest of the two parts are kept insensitive. It has already been stated that with former FOPS design, the length of the sensor needs to be made as short as feasible to minimize external disturbances. In field applications long fibers are usually required. The new FOPS design abolishes this restriction and it provides with a very stable output signal even with a very long fiber (50m or more). With this design, the health of any specific part of a bigger structure could be monitored from long distances using a long lead-in and lead-out fibers while confining the active-fiber to the region of interest. With this new FOPS design, long Hi-Bi (or PM) fibers can be used to make long distance SHM possible with FOPS.

Further, this new design of FOPS is implemented to present our data on an aluminum cantilever and fixed-fixed beams. These structures are considered for study because there are lots of important structures like wings of an aircraft, blades of wind turbines, bridges etc. that experience stresses similar to that of these beam structures. In the present work, the effect of damage on the frequency of the second mode is explored for the first time in case of cantilevers using FOPS. The effect of a crack on both the first and the second fundamental frequencies of a cantilever is analyzed. A relationship between the relative size of a crack in a cantilever and the change in the frequencies of fundamental modes is established [80-82]. This relation has been verified experimentally. A methodology has been proposed which shows that the FOPS technology can be used for the investigation of crack location and crack size along with the global health monitoring in case of cantilevers. An experimental study on effect of crack location and crack size on the first fundamental frequency of a Fixed-fixed beam has also been presented.

4.2 Theory

In this section it is proved that only the active part of the proposed FOPS design is sensitive using Mueller matrix formulation. Further, a crack theory involving first and second fundamental modes in a cantilever is formulated.

4.2.1 Layout of the new design of FOPS

In the conventional FOPS system, linearly polarized light with its direction of polarization at 45° with the slow (or fast) axis is launched into the core of the fiber. The half wave plate is used to set this angle. This angle is kept 45° because in this case the components of the electric field vector, along fast and slow axes, are equal in amplitude which makes the PM fiber the most sensitive. However, it also makes the polarization of light at the output to be highly prone to unwanted disturbances resulting in unstable output signal. If the direction of polarization of the light is kept along any of the two (slow or fast) axes, the sensor is not sensitive at all and output light will remain linearly polarized in the same direction as it was at the entrance end of the fiber. Such an arrangement is used in fiber optic communication where the requirement is that the input signal is not perturbed by environmental factors.
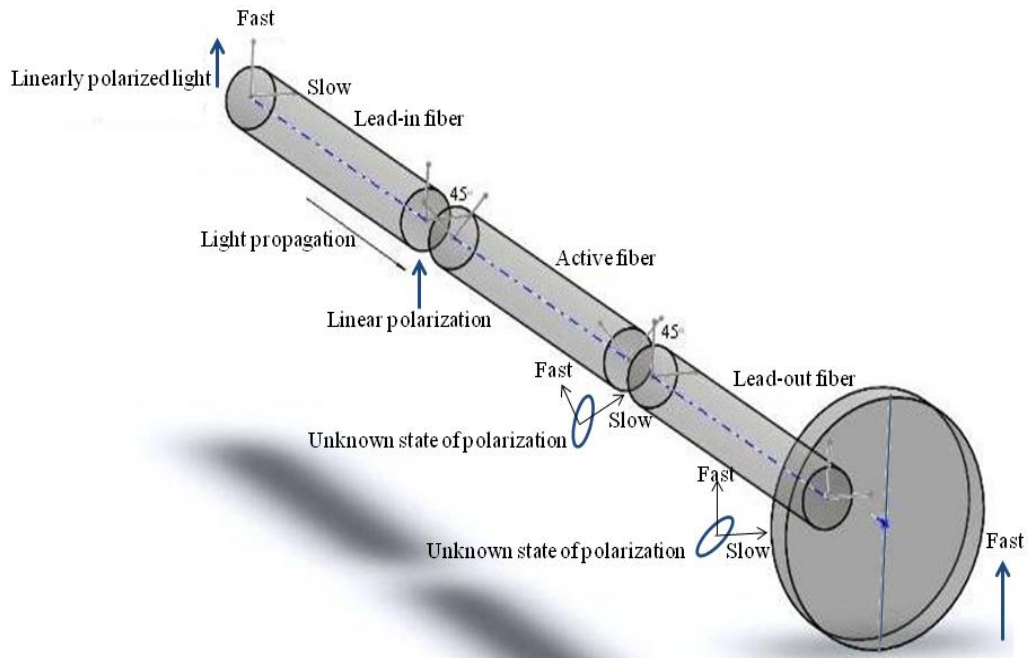
Figure 4.1: Cross sectional layout of new FOPS design.

With this understanding, a different design of FOPS has been proposed which consists of three parts; the lead-in fiber, active fiber and lead-out fiber, as shown in the Figure 4.1. Linearly polarized laser light is launched into the lead-in fiber with the electric vector along either the fast or slow axis, making this fiber insensitive to external perturbations and we get the same linearly polarized light at the output of the lead-in fiber. The lead-in fiber is spliced at an angle of 45° with the active fiber. Light then enters the active fiber with the electric vector at 45° with fast (or slow) axis, making it very sensitive to external perturbations. The amplitudes of the fast and slow components are equal in length in active fiber. Since the exact length of active fiber is not known, the phase change introduced by the active fiber cannot be known. Hence, at the output of the active fiber, the polarization state of the light is unknown. The active part is further spliced with the lead-out fiber at an angle of 45°, which essentially align the fast and slow axes of the lead-in and the lead-out fiber. As the lead-in fiber is insensitive and does not change the polarization of light, a stable polarization mode is likely to be induced in the lead-out fiber [60]. As the light enters the lead-out fiber, the fast and slow components are redistributed and do not have the equal amplitudes anymore. The exact length of lead-out part is not known and hence we get unknown state of polarization at the output of the lead-out fiber once again, as shown in the Figure 4.1. The analyzer, at the exit end of the lead-out fiber, is kept along the fast (or slow) axis of the lead-out fiber. In polarization maintaining fibers, the phase difference between the fast and slow components changes continuously which decides the state of polarization at a particular point, but their amplitudes remain the same at all the time. Since the analyzer is along the fast axis, it selects the fast component from the lead-out fiber only. Essentially, the phase difference introduced by lead-out fiber is not taken into account, as only one component (fast in this case) is considered by aligning the analyzer along the fast axis of the lead-out fiber. Hence, the light after passing through analyzer will be independent of changes in the polarization of light made by the lead-out fiber. Thus, this design keeps the lead-in and the lead-out parts of the sensor insensitive, while maintaining the active part to be sensitive to structural stress.

Mathematically, it can be proved that only the active part of this FOPS design is sensitive. The propagation of light in Hi-Bi fiber can be described by a Mueller matrix [83]. The behavior of the linear polarizer and analyzer can also be characterized by

Mueller matrices. The final Modified Mueller Stokes matrix for the light incident on the detector can be written as the product of all the Mueller matrices corresponding to each optical component used in Figure 4.1:

$$[S_{out}] = [M_A][M_{Lead\ out}][R_{45}][M_{Active}][R_{45}][M_{Lead\ in}][M_P][S_{in}]$$

(4.1)

where $[S_{in}]$ is the Strokes vector of the input light. $[M_P]$ is the Mueller matrix of the linear polarizer along the axis of Hi-Bi fiber. $[M_{Lead\ in}]$, $[M_{Active}]$ and $[M_{Lead\ out}]$ are the Mueller matrices which describe the change in the Strokes vector due to the propagation of light into the lead-in, active and lead-out fibers of the FOPS respectively. $[R_{45}]$ are the rotation matrices and $[S_{out}]$ is the Strokes vector of the output light after the analyzer.

$$
\begin{bmatrix} S_0^{out} \\ S_1^{out} \\ S_2^{out} \\ S_3^{out} \end{bmatrix} = \begin{bmatrix} \frac{1}{2} & \frac{1}{2} & 0 & 0 \\ \frac{1}{2} & \frac{1}{2} & 0 & 0 \\ 0 & 0 & 0 & 0 \\ 0 & 0 & 0 & 0 \end{bmatrix} \times \begin{bmatrix} 1 & 0 & 0 & 0 \\ 0 & 1 & 0 & 0 \\ 0 & 0 & cos\left(\frac{2\pi l_3}{l_b}\right) & sin\left(\frac{2\pi l_3}{l_b}\right) \\ 0 & 0 & -sin\left(\frac{2\pi l_3}{l_b}\right) & cos\left(\frac{2\pi l_3}{l_b}\right) \end{bmatrix}
$$

$$
\times \begin{bmatrix} 1 & 0 & 0 & 0 \\ 0 & 0 & -1 & 0 \\ 0 & 1 & 0 & 0 \\ 0 & 0 & 0 & 1 \end{bmatrix} \times \begin{bmatrix} 1 & 0 & 0 & 0 \\ 0 & 1 & 0 & 0 \\ 0 & 0 & cos\left(\frac{2\pi l_2}{l_b}\right) & sin\left(\frac{2\pi l_2}{l_b}\right) \\ 0 & 0 & -sin\left(\frac{2\pi l_2}{l_b}\right) & cos\left(\frac{2\pi l_2}{l_b}\right) \end{bmatrix}
$$

$$
\times \begin{bmatrix} 1 & 0 & 0 & 0 \\ 0 & 0 & -1 & 0 \\ 0 & 1 & 0 & 0 \\ 0 & 0 & 0 & 1 \end{bmatrix} \times \begin{bmatrix} 1 & 0 & 0 & 0 \\ 0 & 1 & 0 & 0 \\ 0 & 0 & cos\left(\frac{2\pi l_1}{l_b}\right) & sin\left(\frac{2\pi l_1}{l_b}\right) \\ 0 & 0 & -sin\left(\frac{2\pi l_1}{l_b}\right) & cos\left(\frac{2\pi l_1}{l_b}\right) \end{bmatrix}
$$

$$
\times \begin{bmatrix} \frac{1}{2} & \frac{1}{2} & 0 & 0 \\ \frac{1}{2} & \frac{1}{2} & 0 & 0 \\ 0 & 0 & 0 & 0 \\ 0 & 0 & 0 & 0 \end{bmatrix} \times \begin{bmatrix} S_0^{in} \\ S_1^{in} \\ S_2^{in} \\ S_3^{in} \end{bmatrix}
$$

(4.2)

$$\begin{bmatrix} S_0^{out} \\ S_1^{out} \\ S_2^{out} \\ S_3^{out} \end{bmatrix} = \begin{bmatrix} \frac{1}{4}(S_0^{in} + S_1^{in})\left\{1 - cos\left(\frac{2\pi l_2}{l_b}\right)\right\} \\ \frac{1}{4}(S_0^{in} + S_1^{in})\left\{1 - cos\left(\frac{2\pi l_2}{l_b}\right)\right\} \\ 0 \\ 0 \end{bmatrix} \qquad (4.3)$$

where l_b is the beat length of the of the polarization maintaining (PM) fiber. The beat length is the length of PM fiber during which the phase difference of 2π occurs between the fast and slow components of light and the light becomes linearly polarized in the same direction again. In general, the Strokes vector S_{out} describes the polarization evolution of any LP_{0P} mode and not just the LP_{01} mode [83]. However, in this case, only LP_{01} mode has been used. The intensity of light at the detector is denoted by S_0^{out}. From equation (4.3), it is clear that the final Strokes vector is independent of the lengths of lead-in and lead-out sections (l_1 and l_3 respectively) of the sensor proving that this new FOPS is insensitive to the strains produced in the lead-in and lead-out fibers. The final Strokes vector depends only on l_2 which is the length of active section. It proves that the active part is sensitive only.

4.2.2 Crack theory involving first and second fundamental modes for a cantilever

This proposed design of FOPS produces a very stable output and therefore the information provided this FOPS is more reliable. This data definitely presents the more accurate case for the determination of crack size and location in different engineering structures. The fundamental frequencies of any structures depend on its boundary conditions. The frequency of nth fundamental mode of a cantilever is given by [35]:

$$f_n = [a\frac{(2n-1)\pi}{2}]^2 \sqrt{\frac{EI}{\rho A}} \qquad (4.4)$$

From equation (4.4), it can be clearly seen that the frequency of the fundamental mode depends on the flexural stiffness (*EI*) of the cantilever. If the beam is damaged, the stiffness will reduce resulting in a corresponding decrease in the frequency of the fundamental mode.

In our study, the crack is modelled by a mass-less linear spring of stiffness K [80]. The cracked beam and its spring model are shown in the Figures 4.2(a) and (b) respectively. The relative change in the frequency of any fundamental mode is given by [81]:

$$\frac{\Delta f_n}{f_n} = sin^2(\frac{n\pi x}{2})\frac{EI}{KL} \qquad (4.5)$$

where EI is the stiffness, L is the length of the cantilever and x represents the non-dimensional crack location and it is the function of distance (l) of crack from the fixed end. The stiffness K of the spring is given by [82, 84]:

$$K = \frac{EI}{(5.346h).f(a/h)} \qquad (4.6)$$

where 'h' is the height of the cantilever and 'a' is the size of the crack. The function $f(a/h)$ is given by [17, 19]:

$$f(a/h) = 1.8624(a/h)^2 - 3.95(a/h)^3 + 16.375(a/h)^4 - 37.226(a/h)^5 +$$
$$78.81(a/h)^6 - 126.9(a/h)^7 + 172(a/h)^8 - 143.97(a/h)^9 +$$
$$66.56(a/h)^{10} \qquad (4.7)$$

As the ratio a/h is small, higher orders of a/h could be neglected. Hence equation (4.7) reduces to:

$$f(a/h) \approx 1.8624(a/h)^2 \qquad (4.8)$$

From equations (4.5) and (4.6) we have:

$$\frac{\Delta f_n}{f_n} = Sin^2(\frac{n\pi x}{2})\frac{5.346.h.f(a/h)}{L} \qquad (4.9)$$

From equation (4.9) it is clear that the change in natural frequency depends on the location and size of the crack both.

(a)   (b)
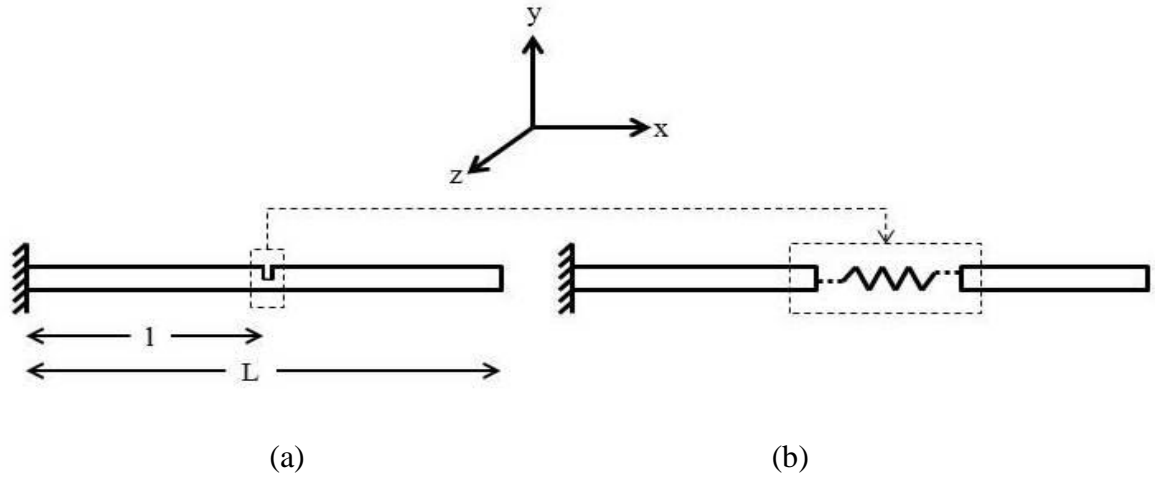
Figure 4.2: (a) An aluminum cantilever with a single crack and (b) spring model of cracked cantilever beam.

4.3 Experiments and results

The schematic of the experimental set-up to test this new design of FOPS is shown in the Figure 4.3. The cross marks in the diagram indicate the splicing points. The output from the photodiode could be interrogated either by an Oscilloscope or by a Data Acquisition System. Standard Hi-Bi fiber, HB600 provided by Fibercore Ltd, was used for this test. The beat length of this fiber is 1.3mm at 633nm. He-Ne laser (633nm) provided by Melles Griot, was used as the light source for this experiment. The output power of the laser was 3mW. Three Hi-Bi fibers were spliced together in a certain manner as depicted in the Figure 4.1 using an arc fusion splicer (FSM-40PM by Fujikura) shown in the Figure 4.4. In this splicer, a splicing profile can be selected in which any angle between the principal axes of two Hi-Bi fibers can be set-up.
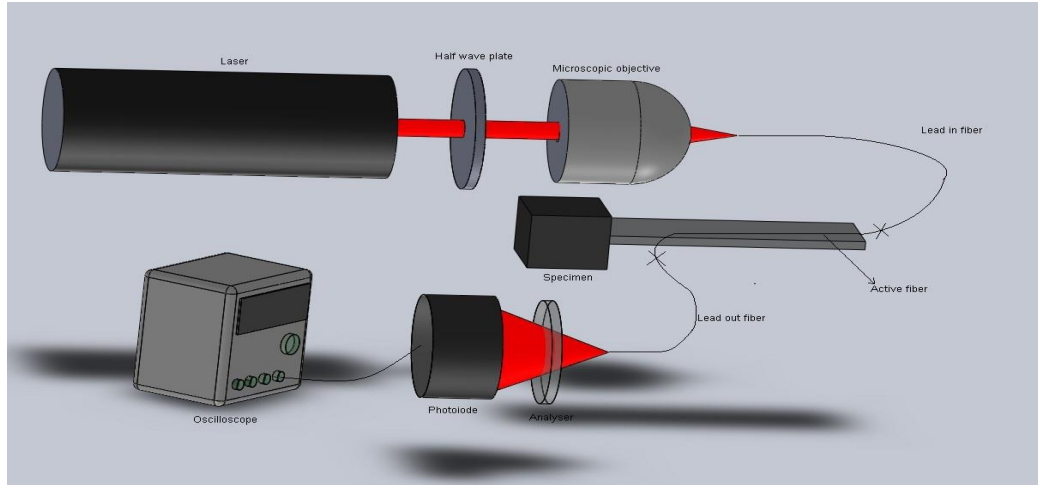
Figure 4.3: Schematic of new FOPS experimental set-up with insensitive coupling.

Figure 4.4: Screen and front panel of the Splicer.

Figure 4.5 shows the screen shots of the output from the photodiode of a conventional FOPS system with a single Hi-Bi fiber of about 30 meters. The polarized laser light (633 nm) was launched with its electric vector at 45° with fast (or slow) axis with the help of a half wave plate. From Figures 4.5(a) and (b), it is clear that the output from the conventional FOPS system is highly unstable and therefore, it is very difficult and tedious to use conventional FOPS for SHM of different structures. Figure 4.6 shows the screen shots of the output from the photodetector of the new FOPS system. Again the half wave plate was used to launch the linearly polarized laser light into the lead-in fiber at an angle of 0° with either the fast axis or the slow axis. Since the active fiber is spliced at 45° with the lead-in fiber, the angle between the direction of polarization of light and the fast axis (or slow axis) becomes 45° inactive fiber. Lastly, the light

coming out lead-out fiber passes through an analyzer which was kept along fast (slow) axis to select one polarization component of the lead-out fiber. This condition makes lead-in fiber, lead-out fiber completely insensitive and active fiber the most sensitive to external perturbations. Figures 4.6(a) and (b) show the output from new FOPS which is highly stable.

(a)   (b)
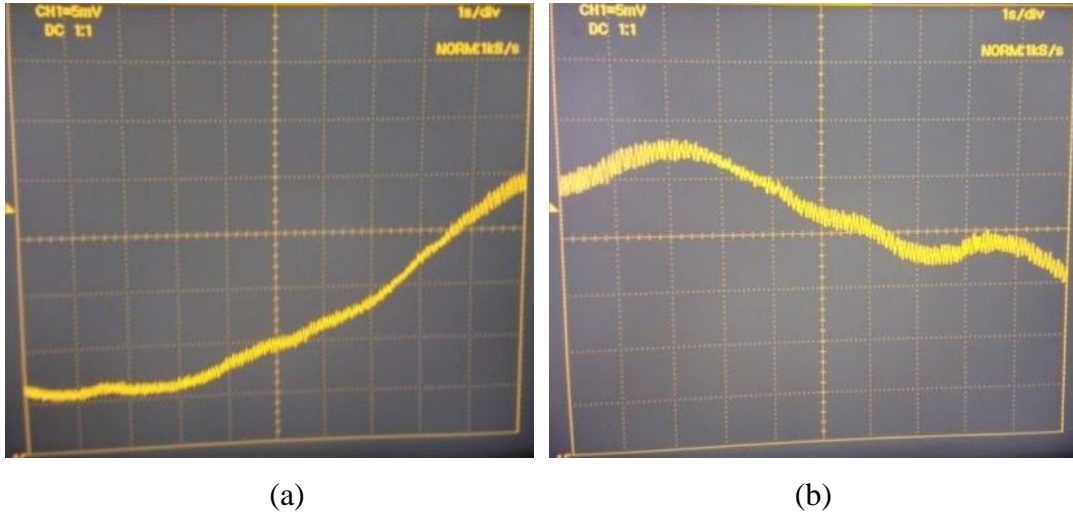
Figure 4.5: Screen shots of the output coming from the former FOPS system.

(a)   (b)
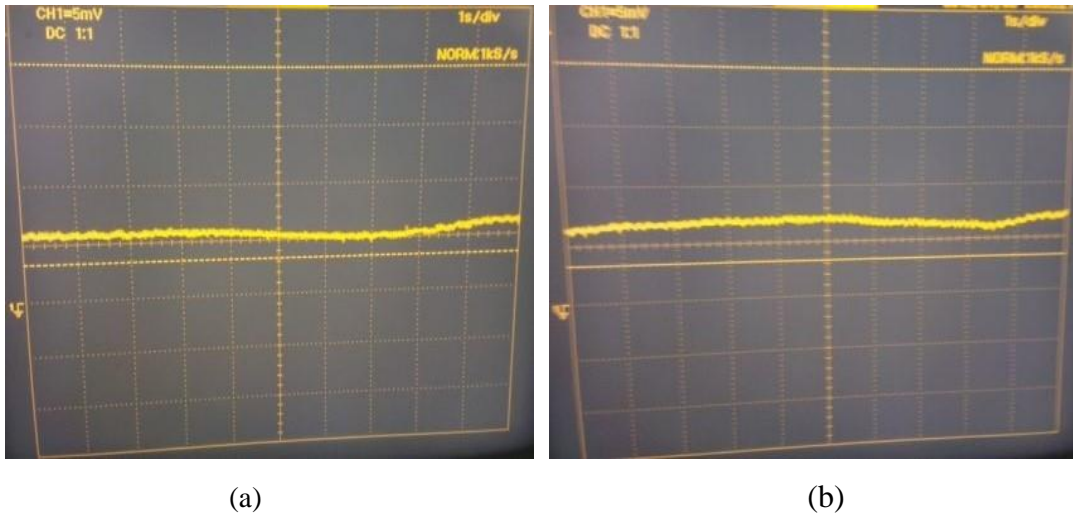
Figure 4.6: Consecutive screen shots of the output coming from new design of FOPS system.

Figure 4.7 shows the responses of the three sections of this new FOPS design, the lead-in fiber, the active fiber and the lead-out fiber, when subjected to external perturbations respectively. From Figure 4.7, it is clear that the sensitivity of both the

lead-in and lead-out fibers is almost negligible as compared to that of the active fiber. Hence now by using short active part, any localized section of a structure can be targeted for SHM. Also by using a long lead-in and lead-out fibers, long distance SHM can now be performed with FOPS.

Figure 4.7: Responses of three parts of the current FOPS design.

This very stable FOPS system was then used to investigate the size and location of a crack in an aluminum cantilever. The length of lead-in, active and lead-out fibers were 30 meters, 0.5 meters and 5 meters respectively. In this case the active part is sensitive only. As light traverses the active fiber, the polarization of light divides into two components; one along the fast axis and another one along the slow axis. The fast component travels faster than the slow component leading to a phase difference between both the components. The active fiber is bonded to the specimen (cantilever in this case) with epoxy. In case of strain (elongation or compression) produced in active fiber, the distance travelled by both the components (fast and slow) changes and hence the phase difference changes. This leads to the change in the polarization of light. Since the light reaches the photodiode through a linear analyzer, the intensity measured by the photodiode changes. Dynamic changes in the strain cause periodic changes in the intensity of the light at the frequency depending on the external perturbations.

4.3.1 Damage investigation in a cantilever beam

An aluminum cantilever beam of length 265mm, breadth 19mm and thickness 3.2mm was used in the experiment. The cantilever is made to vibrate with its fundamental

frequency by impacting it with a hammer. These vibrations yield elongation and compression in the Hi-Bi fiber with the same fundamental frequency of the cantilever. This leads to the change in intensity of light at the photodiode with the same frequency. The vibrations are completely reproducible. The schematic diagram of experimental set-up is shown in Figure 4.3 and the actual experimental set-up is shown in the Figure 4.8. An oscilloscope was used to record the frequencies of first and second fundamental modes. Figure 4.9 shows the oscilloscope traces of the first and second fundamental frequencies of the cantilever. Different traces in Figure 4.9 correspond to different crack sizes for the crack location at 2 cm from the fixed end of the cantilever. Though the crack location is the same for all the traces in Figure 4.9, the flexural stiffness (*EI*) of the cantilever reduces on increasing the crack size. This in turn decreases the fundamental frequencies as illustrated in equation (4.5). This reduction in fundamental frequencies with increasing crack size can be clearly seen in Figure 4.9. F1 and F2 refer to first and second mode, respectively. Cracks were induced with a very fine saw.
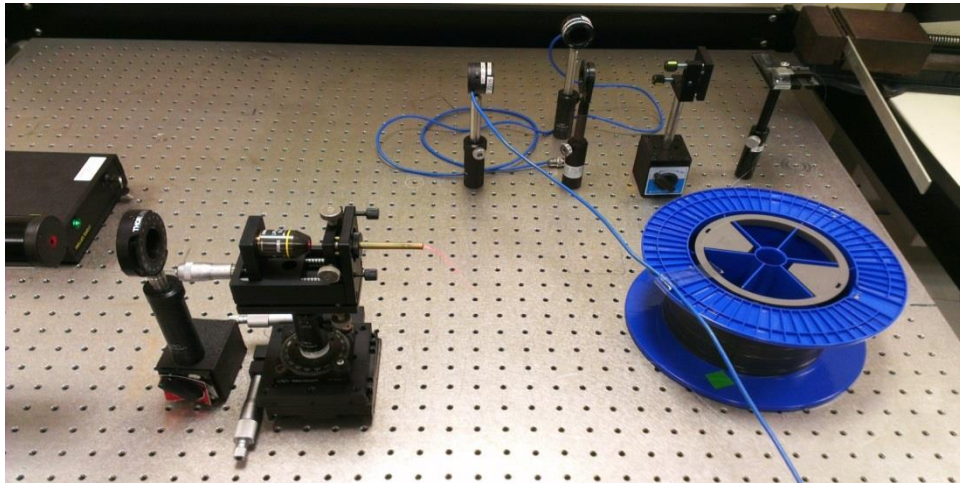
Figure 4.8: Designed lab experimental set-up for FOPS.

(a)

(b)

(c)

(d)
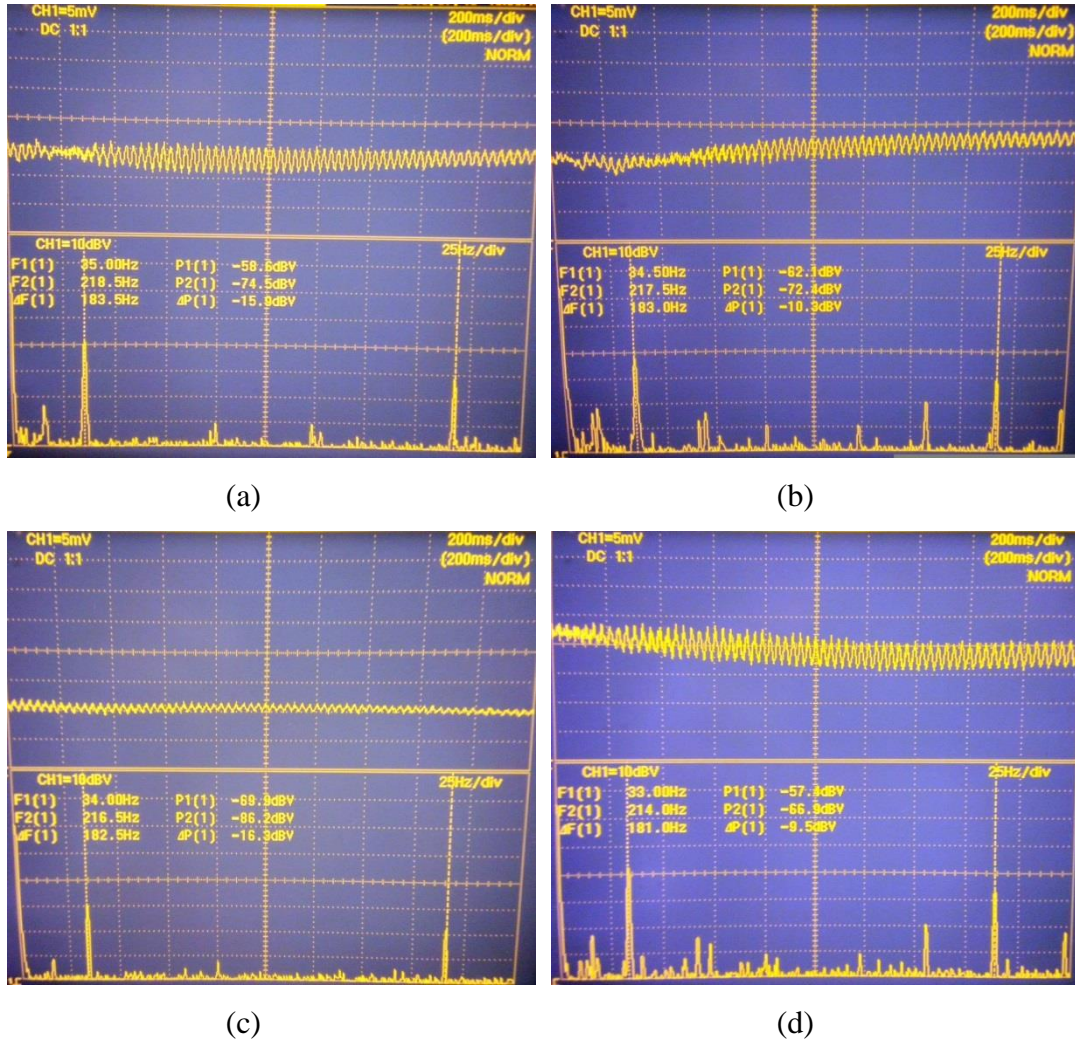
Figure 4.9: Oscilloscope traces showing the frequencies of first and second fundamental mode of the cantilever with a fixed crack location 2 cm from the fixed end and crack size is (a) no crack, (b) 3 mm, (c) 6 mm, (d) 8.5 mm.

Equation (4.9) shows that for a particular crack location and for small values of (a/h), the relative change in the fundamental frequencies $(\Delta f_n/f_n)$ is a quadratic function of (a/h). The plots in Figure 4.10 and Figure 4.11, show the variations of $(\Delta f_1/f_1)$ and $(\Delta f_2/f_2)$ with relative crack size (a/h) and trend as per the theory. Although their form of the equation is quadratic (px^2+qx+r), the coefficients 'q' and 'r' are very small and can be neglected. Change in the boundary conditions, resolution limitation of the oscilloscope etc. lead to the non-zero values of coefficients 'q' and 'r'.
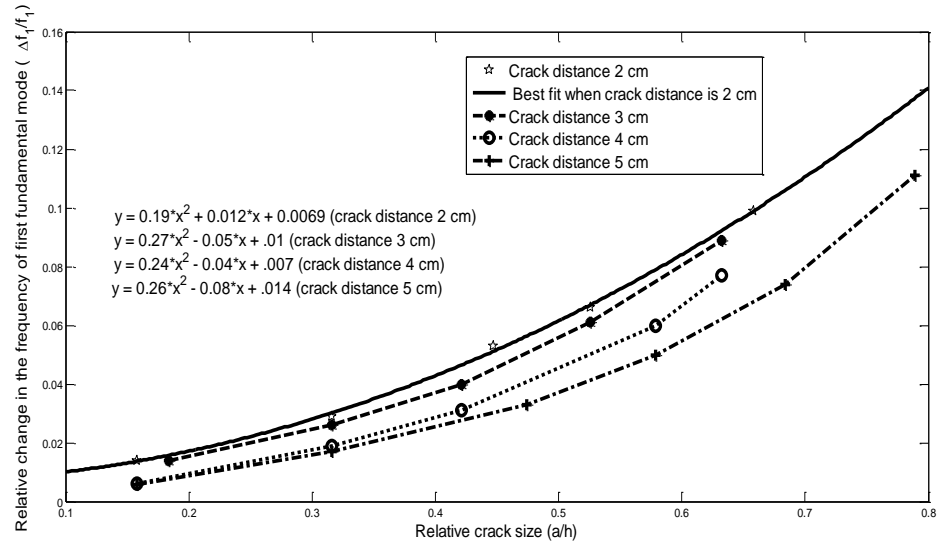
Figure 4.10: Relative change in the first fundamental frequency of a cantilever with relative crack size at different crack locations.
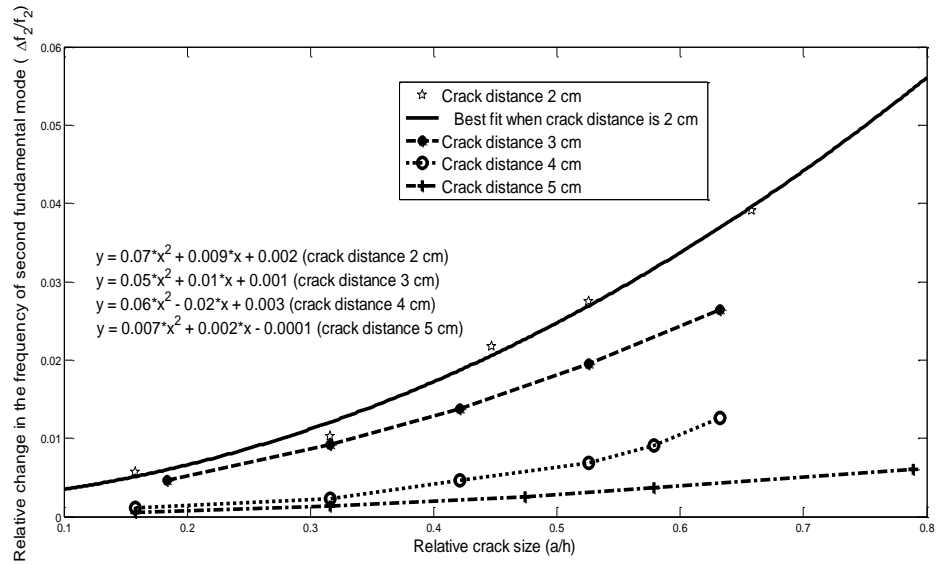
Figure 4.11: Relative change in the second fundamental frequency of a cantilever with relative crack size at different crack locations.

Furthermore, the relative change in the frequencies of first and second fundamental modes is plotted against the relative distance (l/L) of the crack from the fixed end of the cantilever in Figures 4.12 and 4.13 respectively. Different plots correspond to different crack sizes. From Figures 4.12 and 4.13, it is clear that the second fundamental mode is more sensitive to the crack location as the plots in Figure 4.13 are steeper than the plots in Figure 4.12. Hence the second mode distinguishes crack locations better than the first one. But this is true only in the vicinity of the fixed end

76

of the cantilever, i.e. the regions of high strain (or stiffness). As we move away from the fixed end of the cantilever, the strain/stress decreases. In the regions of low strain i.e. away from the fixed end of the cantilever, the change in the frequency of first mode becomes more significant than changes in the second mode. It means if the crack is far away from the fixed end, the first mode is dominant. Hence the comparison between the change in fundamental frequencies (Δf_1 and Δf_2) gives a strong indication of the location of the crack.
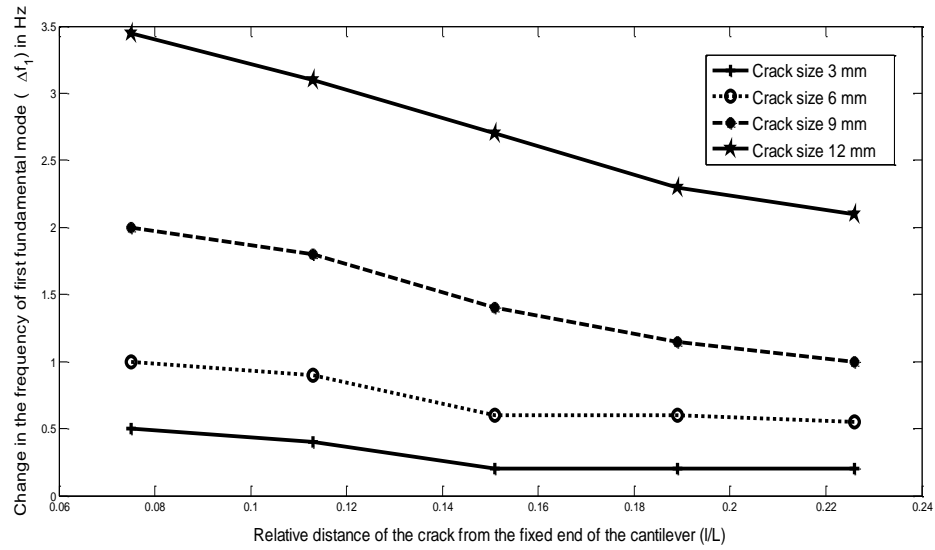
Figure 4.12: Change in the first fundamental frequency with relative position of a crack with different crack sizes.
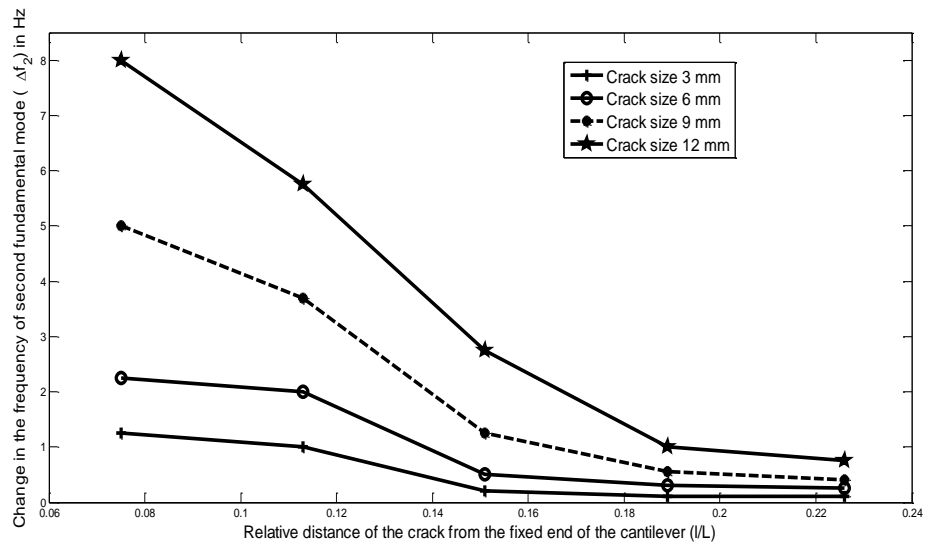
Figure 4.13: Change in the second fundamental frequency with relative position of a crack with different crack sizes.

Equation (4.9) indicates that the ratio of change in frequencies of any two fundamental modes is independent of the size of the crack (a). Figure 4.14 shows the plots of the ratio of second fundamental frequency to first fundamental frequency against the crack size at different crack locations. The almost straight lines in Figure 4.14 suggest that $\Delta f_2/\Delta f_1$ is independent of the crack size. This ratio depends only on the crack location. Thus, by calculating this ratio ($\Delta f_2/\Delta f_1$), the location of the crack can be identified with the help of Figure 4.9. This information about the crack location can further be used in conjunction with Figure 4.9 and Figure 4.10 to know the size of the crack.
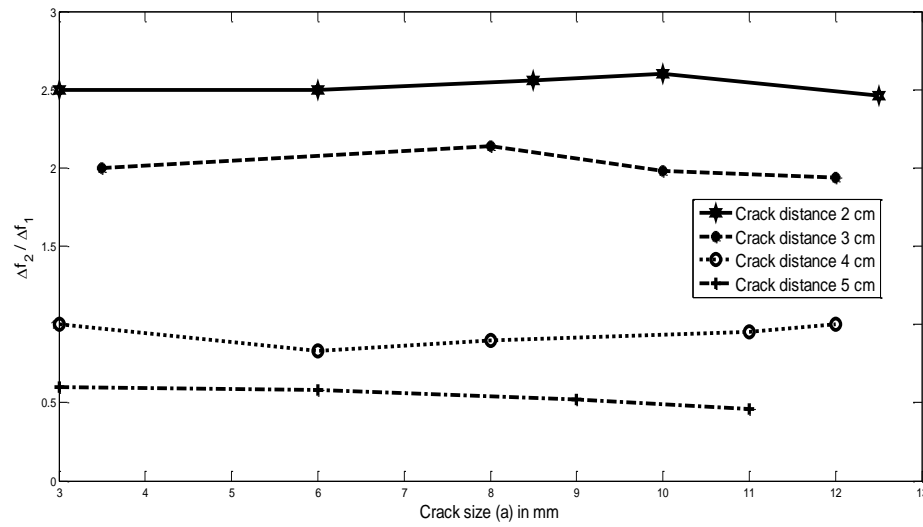
Figure 4.14: Ratio of the frequencies of second to first fundamental mode vs crack size at different crack locations.

4.3.2 Damage investigation in a fixed-fixed beam

Further, an experiment was performed with a beam fixed at both the ends. The size of the beam was $370 \times 19 \times 3.2$ mm^3. The active part of the FOPS was bonded to the fixed-fixed beam and rest of the set-up was the same as shown in Figure 4.3. In case of a fixed-fixed beam, the second fundamental mode could not be excited. The relative change in the frequency of first fundamental mode ($\Delta f_1/f_1$) is plotted against the relative crack length (a/h) for different crack locations in Figure 4.15. The distance of crack is measured from the mid-point of the beam. The plots in Figure 4.15 (for fixed-fixed beam) trend as per the theory established for cantilevers in equation (4.9). Again, although the form of the equation is quadratic (px^2+qx+r), the coefficients 'q' and 'r' are very small and can be neglected.

Furthermore, the change in the frequency of first fundamental mode (Δf_1) has been plotted against the relative distance (l/L) of the crack from the center of the fixed-fixed beam in Figures 4.16. Different plots correspond to different crack sizes. From Figure 4.16, the value of Δf_1 is higher when the crack is close to the mid-point of the beam and it decreases as the crack moves towards the fixed ends of the beam. This suggests that center region of a fixed-fixed beam is a high strain (or stiffness) region. Figure 4.16 also suggests that if the value Δf_1 is significantly high (>1 Hz), the crack will more like to be in the central region of the fixed-fixed beam.
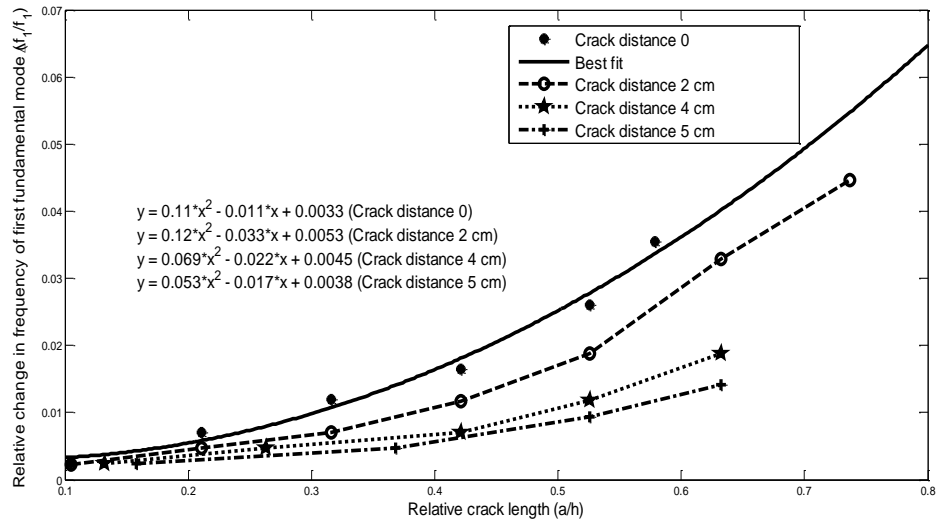
Figure 4.15: Relative change in the first fundamental frequency of a fixed-fixed with relative crack size at different crack locations from the mid-point.
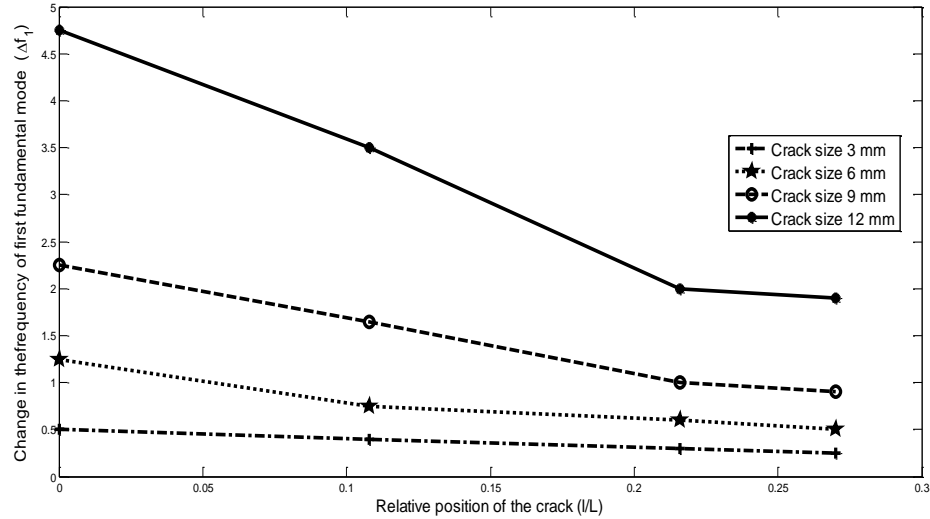
Figure 4.16: Relative change in the first fundamental frequency of a fixed-fixed with relative position of a crack from the mid-point with different crack sizes.

Although the change in frequency of the first mode (Δf_1) gives important information about the crack size and location in case of a fixed-fixed beams also, the size and location of cracks could not be found unlike the case of cantilevers. This is because in case of a fixed-fixed beam, the second fundamental mode could not be excited.

4.4 Summary

The output signal of proposed FOPS is much more stable as compared to the output signal of conventional FOPS. Therefore, with this design of FOPS, SHM tests can be performed more accurately. Unlike earlier, long distance long distance SHM can be performed without jeopardizing the signal stability and measurement accuracy. Further, this design of FOPS has been successfully implemented for the actual damage state in cantilever beams, which was incomplete at best in the past. Finally, results show that the detection of the location and size of a crack is possible with FOPS in case of a cantilever like structures. An experimental study on effect of cracks on first fundamental frequency of Fixed-fixed beams has also been presented. Although the results give important information about the damage state in the beam, the exact location of the cracks could not be found as the second fundamental mode could not be excited in the fixed-fixed beam.

CHAPTER – 5 FBG and FOPS for Local and Global SHM on a single fiber

A novel concept is proposed by which FBG and FOPS can be realized on a single fiber. According to this proposition FBG written of polarization maintaining (PM) fiber (or PM-FBG) can be used for both, local and global SHM simultaneously. Further, based on this concept a sensor design has been proposed which gives improved information on the damage location in beam structures.

5.1 Introduction

Fiber optic sensors are now being increasingly used in SHM industry for different mechanical and civil structures [85]. Of all the Fiber Optic Sensors, Fiber Bragg Grating (FBG) sensors are the most versatile and are being used in a variety of applications ranging from damage detection in composites [50] to dynamic structural strain monitoring on Hong Kong's Tsing Ma bridge [67] to long term stain monitoring in the construction industry [86, 87]. Since the FBGs perform point measurement, the monitoring of the entire structure cannot be readily accomplished.

The fiber optic polarimetric sensors (FOPS) allow real time measurement which provides a global response of structure to external loads. FOPS have already been implemented for global damage monitoring structures. Usually, FOPS monitor the structures through static or dynamic loading tests [35]. FOPS only provide global information without specific information on the severity or location of damage sites.

FBG sensors provide localized strain data, thereby providing local damage information, while FOPS (PM fiber) are known for their capabilities of global damage monitoring. However, each sensor has to be used with its own instrumentation and processing system. Independently obtained information from FBG and FOPS instrumentations definitely provides an improved scenario if combined together. The instrumentation of both FBG and FOPS together is complicated to handle and becomes expensive too. Getting combined information from only one set up (either FBG or FOPS) would be good. It was thought that an FBG written on the Polarization Maintaining (PM) fiber should thus be able to provide combined information; global

structural monitoring (FOPS) and local strain sensing (FBG). For an FBG written on Polarization Maintaining fiber (PM-FBG), two Bragg reflections corresponding to the two modes of polarization of light, are observed [90]. A PM-FBG spliced to a single mode fiber was demonstrated as a dual purpose compact fiber optic grating vector vibroscope in which the amplitude and the orientation of the vibration from the principal axes could be measured. The response of the sensor is completely independent of temperature variation [88]. On application of a transverse load on a π-phase shifted PM-FBG, spectral splitting occurs. This feature was used for transverse load measurement [89]. A PM-FBG was embedded in an epoxy specimen and then it was put under biaxial loading experiment. The results showed that transverse sensitivity of the PM-FBG is smaller than the longitudinal one [90]. The spectral properties of diametrically compressed PM-FBG displayed that reflected spectra exhibit narrow and tunable spectral hole. The tuning of this spectral hole depends on the magnitude and angle of the applied force [91].

Available literature suggests that PM-FBG sensors have only been studied for transverse strain. In SHM techniques, the longitudinal strain is measured instead. The reaction of PM-FBG to longitudinal strain is similar to that of a normal FBG; both Bragg wavelengths shift in unison under longitudinal strain. The peak amplitudes of both Bragg wavelengths never came to focus as the peak powers remain unchanged under longitudinal strain. In this research, the amplitudes of both the Bragg wavelengths have also been studied for the first time. In the current work, a novel idea is proposed which makes the peak amplitudes responsive to longitudinal strain. The change in peak amplitude provides the state of polarization (SOP) which is FOPS action. Additionally, the Bragg wavelength shift provides local longitudinal strain (FBG action). SOP measurement is used for global monitoring and Bragg wavelength shift is used for local strain monitoring. This enables both global and local structural health monitoring to be realized simultaneously on a single PM-fiber with only one experimental set up (FBG instrumentation). Thus, combined (FBG + FOPS) information could be obtained with minimum instrumentation and cost.

As a consequence of this idea, a sensor design is proposed which provides the precise damage location site in the beam structures independent of the boundary conditions.

Hence it may apply to a wide variety of beam structures. This design can be altered to achieve high precision too. The precision in locating the damage can be as good as 8-10cm, depending on how close two PM-FBGs can be spliced.

5.2 Theoretical background and concept development using Mueller matrices

In case of PM fiber, the refractive indices along the fast axis and slow axis are different resulting in two peaks in the reflection spectrum of a PM-FBG. The Bragg wavelengths for the refractive indices along fast and slow axes are given as [90, 92]:

$$\lambda_{B,f} = 2n_1\Lambda$$

(5.1)

$$\lambda_{B,s} = 2n_2\Lambda$$

where $\lambda_{B,f}$, $\lambda_{B,s}$ and n_1, n_2 are the Bragg wavelengths and refractive indices along the fast and slow axes. Λ is the grating period. The wavelength shifts for the fast and slow components due to longitudinal strain, assuming there is no transverse strain, can be written as [92]:

$$\Delta\lambda_{B,f} = \varepsilon_3 \left[1 - \frac{1}{2}n_1^2 p_\varepsilon\right] \lambda_{B,f}$$

(5.2)

$$\Delta\lambda_{B,s} = \varepsilon_3 \left[1 - \frac{1}{2}n_2^2 p_\varepsilon\right] \lambda_{B,s}$$

where ε_3 is the longitudinal strain and p_ε is the strain optic coefficient. The difference between n_1 and n_2 of a PM fiber is very low (0.00033 in this case) and the strain value is also a very small quantity and it is measured in $\mu\varepsilon$. Therefore, both wavelength shifts given by equation (5.2) are essentially the same. The effect of longitudinal strain on the amplitudes of these two peaks has never been studied earlier. Figure 5.1 shows the linearly polarized light being launched into a PM-FBG fiber with the direction of polarization at an angle θ from the fast axis of the PM fiber.
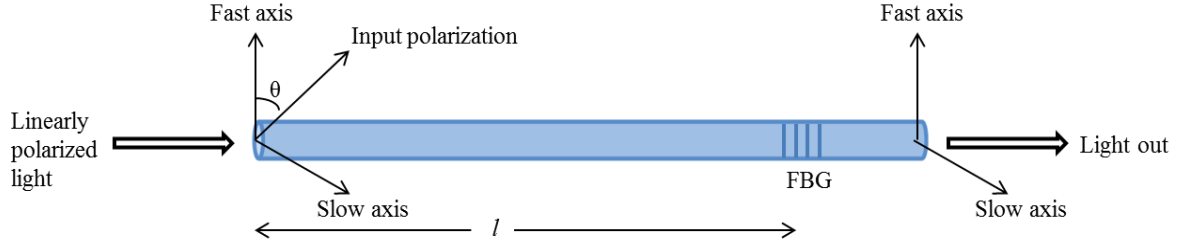
Figure 5.1: Cross sectional layout on an FBG written on a PM fiber with linearly polarized light launched at an angle θ.

The intensity of the two Bragg reflected peaks can be calculated using the Mueller matrix method [83]. The finally modified Mueller Stokes matrix for light emerging from the fiber along the fast axis can be written as the product of the Mueller matrices corresponding to each element shown in Figure 5.1. Hence,

$$[S_{out}] = [M_{PM,l,ref.}][M_f][M_{PM,l}][M_\theta][S_{in}]$$

(5.3)

where $[S_{in}]$ and $[S_{out}]$ are the Stokes vectors of the input and output light respectively. $[M_\theta]$ is the Mueller matrix of the light, linearly polarized at an angle θ from the fast axis of the PM fiber. $[M_{PM, l}]$ is the Mueller matrix which describes the change in the Stokes vector due to the propagation of light in the PM fiber. $[M_f]$ is the component along the fast axis. The component along the slow axis can also be considered simply by reversing the sign in the Mueller matrix $[M_f]$. Finally, $[M_{PM, l, ref.}]$ is the matrix of the light reflected from the FBG. The reflected light travels the same path again.

$$
\begin{bmatrix} S_0^{out} \\ S_1^{out} \\ S_2^{out} \\ S_3^{out} \end{bmatrix}_f =
\begin{bmatrix}
1 & 0 & 0 & 0 \\
0 & 1 & 0 & 0 \\
0 & 0 & \cos\left(\dfrac{2\pi l}{l_b}\right) & \sin\left(\dfrac{2\pi l}{l_b}\right) \\
0 & 0 & -\sin\left(\dfrac{2\pi l}{l_b}\right) & \cos\left(\dfrac{2\pi l}{l_b}\right)
\end{bmatrix}
\times
\begin{bmatrix}
\dfrac{1}{2} & \dfrac{1}{2} & 0 & 0 \\
\dfrac{1}{2} & \dfrac{1}{2} & 0 & 0 \\
0 & 0 & 0 & 0 \\
0 & 0 & 0 & 0
\end{bmatrix}
$$

$$
\times
\begin{bmatrix}
1 & 0 & 0 & 0 \\
0 & 1 & 0 & 0 \\
0 & 0 & \cos\left(\dfrac{2\pi l}{l_b}\right) & \sin\left(\dfrac{2\pi l}{l_b}\right) \\
0 & 0 & -\sin\left(\dfrac{2\pi l}{l_b}\right) & \cos\left(\dfrac{2\pi l}{l_b}\right)
\end{bmatrix}
$$

$$
\times
\begin{bmatrix}
1 & \cos2\theta & \sin2\theta & 0 \\
\cos2\theta & \cos^2 2\theta & \cos2\theta.\sin2\theta & 0 \\
\sin2\theta & \cos2\theta.\sin2\theta & \sin^2 2\theta & 0 \\
0 & 0 & 0 & 0
\end{bmatrix}
\tag{5.4}
$$

$$
\times
\begin{bmatrix} S_0^{in} \\ S_1^{in} \\ S_2^{in} \\ S_3^{in} \end{bmatrix}
$$

$$
\begin{bmatrix} S_0^{out} \\ S_1^{out} \\ S_2^{out} \\ S_3^{out} \end{bmatrix}_f =
\begin{bmatrix}
\left(S_0^{in} + S_1^{in}.\cos2\theta + S_2^{in}.\sin2\theta\right)\cos^2\theta \\
\left(S_0^{in} + S_1^{in}.\cos2\theta + S_2^{in}.\sin2\theta\right)\cos^2\theta \\
0 \\
0
\end{bmatrix}
\tag{5.5}
$$

In general, the Stokes vector S_{out} describes the polarization evolution of any LP_{0P} mode and not just the LP_{01} mode [83]. However, in this case, only LP_{01} mode has been used. Here the matrices have been solved for fast component. The first Stokes parameter, S_0^{out}, represents the intensity of fast component. From equation (5.5), it is clear that the intensity of the fast component is independent of the length of the PM fiber. It indicates that the longitudinal strain has no effect on the intensity, but the intensity is a sin and cosine function of the input polarization angle θ. Similarly, the matrix for the slow component can be calculated.

5.3 Development of new concept

The novel proposal in this paper makes the amplitude of the fast (or slow) component of the PM-FBG fiber sensitive to the longitudinal strain. A separate PM fiber is spliced to the PM-FBG at an angle of 45° as shown in the Figure 5.2. Deviation from 45°

during splicing will cause uneven sinusoidal variation of peak amplitudes. l_1 is the length of the first section of the PM fiber and l_2 is the distance of the FBG from the splice point. In this case, the final modified Mueller Stokes matrix for the fast component received at the OSA can be written as the product of all the Mueller matrices corresponding to every action shown in Figure 5.2.
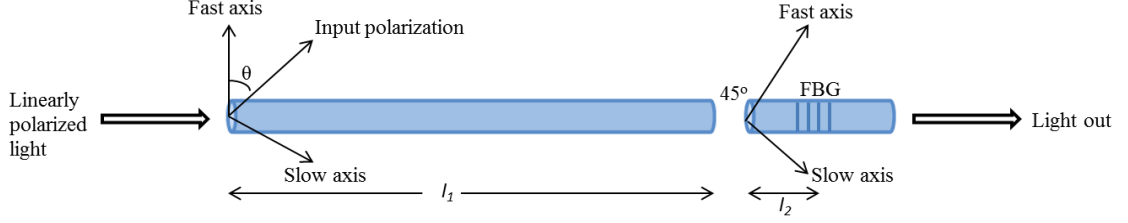
Figure 5.2: Cross sectional layout of a PM fiber spliced to a PM-FBG at an angle of 45°.

$$[S_{out}] = [M_{PM,l_1,ref}][R_{45}][M_{PM,l_2,ref.}][M_f][M_{PM,l_2}][R_{45}][M_{PM,l_1}][M_\theta][S_{in}] \quad (5.6)$$

where $[S_{in}]$ and $[S_{out}]$ are the Stokes vectors of the input and output light respectively. $[M_\theta]$ is the Mueller matrix of the light, linearly polarized at an angle θ from the fast axis of the PM fiber. $[M_{PM,l_1}]$ and $[M_{PM,l_2}]$ are the Mueller matrices which describe the change in the Stokes vector due to the propagation of light into the PM fiber of length l_1 and l_2 respectively. $[M_f]$ is to select the fast component. $[R_{45}]$ are the rotation matrix. Finally, $[M_{PM,l_1,ref}]$ and $[M_{PM,l_2,ref.}]$ are the matrices for the light reflected from the FBG, which travels the lengths l_1 and l_2 again.

$$\begin{bmatrix} S_0^{out} \\ S_1^{out} \\ S_2^{out} \\ S_3^{out} \end{bmatrix} = \begin{bmatrix} \frac{1}{2}\begin{bmatrix} (S_0^{in} + S_1^{in}cos2\theta + S_2^{in}sin2\theta) \\ -\{S_0^{in}sin2\theta + S_1^{in}cos2\theta.sin2\theta + S_2^{in}sin^2 2\theta\}cos\left(\frac{2\pi l_1}{l_b}\right) \end{bmatrix} \\ 0 \\ \frac{1}{2}\begin{bmatrix} (S_0^{in} + S_1^{in}cos2\theta + S_2^{in}sin2\theta) \\ -\{S_0^{in}sin2\theta + S_1^{in}cos2\theta.sin2\theta + S_2^{in}sin^2 2\theta\}cos\left(\frac{2\pi l_1}{l_b}\right) \end{bmatrix}cos\left(\frac{2\pi l_1}{l_b}\right) \\ -\frac{1}{2}\begin{bmatrix} (S_0^{in} + S_1^{in}cos2\theta + S_2^{in}sin2\theta) \\ -\{S_0^{in}sin2\theta + S_1^{in}cos2\theta.sin2\theta + S_2^{in}sin^2 2\theta\}cos\left(\frac{2\pi l_1}{l_b}\right) \end{bmatrix}cos\left(\frac{2\pi l_1}{l_b}\right) \end{bmatrix} \quad (5.7)$$

From equation (5.7), it is clear that S_o^{out}, which represents the intensity (amplitude) of the fast component reflected by the PM-FBG, is a function of θ and l_1 only. It is independent of l_2 i.e. for a fixed input polarization angle θ; the intensity is responsive to the changes in length in the first section of PM fiber (l_1), but not to that in the second section (l_2). The length l_1 can be kept as long as required and l_2 can be kept as short as possible. l_b represents the beat length of the polarization maintaining fiber used. Essentially, with this idea, the intensity of light reflected by PM-FBG is a function of the changes in length produced in the PM fiber before the splicing point (length l_1), where the Bragg wavelength is not responsive enough as this region is far away from the FBG. However, it does not respond to the longitudinal strain produced in the PM fiber on which the FBG is written (length l_2).

It has already been shown that the FBGs are useful in damage detection only if the damage is very close to them (around 10 cm) [66]. Multiple FBGs configuration is used for distributed strain sensing. With the current approach, the intensities of fast and slow components of the Bragg reflection change with the elongation of the PM fiber. The state of polarization (SOP) which is the function of intensities of fast and slow components (I_f and I_s) is defined as [35]:

$$SOP = (I_f - I_s)/(I_f + I_S) \tag{5.8}$$

These intensities I_f and I_s vary sinusoidally with increasing elongation in the PM fiber and therefore, SOP varies sinusoidally with increasing elongation in the PM fiber.

The intensities of the fast and slow components are the functions of longitudinal strain produced in the length l_1 and the angle of input polarization (θ) both as suggested by the equation (5.7). If there is damage in the length l_1, the stiffness of this part will reduce and therefore, small loads will produce more strain in this section (l_1) which in turn will cause the amplitude of the fast component to change more rapidly. Hence, only damage will be responsible for the change in the cycle period of the amplitude. Though the amplitude varies with θ too, the change in θ does not alter the cycle period of amplitude of the fast component (Appendix A). Only damage in the first section of PM fiber would change the cycle period.

If light intensity changes, both I_f and I_s will follow accordingly. This will change the SOP value instantly, but here in this study, the SOP value at a particular instant of time does not play any role. The period of SOP cycle is the only important parameter which is the function of longitudinal strain only.

5.4 Experiments and results

5.4. 1 Validation of the proposed concept

To validate the above concept, an experiment was performed to see the effect of longitudinal extension on the intensities of the fast and slow Bragg wavelengths reflected by the PM-FBG. A grating was written on a PM fiber using an Excimer laser (248nm) and a phase mask to reflect an 810nm Bragg wavelength. The fast and the slow Bragg wavelengths of this PM-FBG differ by 0.2 nm (theoretically 0.17 nm) as shown in the Figure 5.5. This PM-FBG was bonded to the bottom of 70x1.9x.32 cm^3 simply supported aluminium beam using epoxy. A micrometer was used to provide a known displacement of the center of the beam. The actual experimental setup and the schematic diagram are shown in the Figure 5.3 and Figure 5.4 respectively.

Figure 5.3: Experimental set up to test the response of PM-FBG under strain.
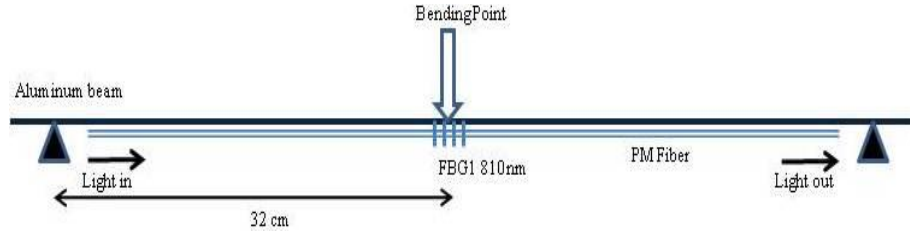
Figure 5.4: Schematic diagram of simply supported beam with PM-FBG fiber bonded to the bottom of the aluminum beam.

Figure 5.5 shows the screen captures from an Optical Spectral Analyzer (OSA) depicting the reflections from the PM-FBG for different mid-point deflections of the beam. Clearly, both fast and slow Bragg wavelengths increase by the same amount with increasing displacement/strain (Table 5.1), but their intensities do not change as suggested by the equation (5.5). A higher order mode was observed due to the short length of the PM fiber [67, 68].

(a)   (b)

(c)   (d)
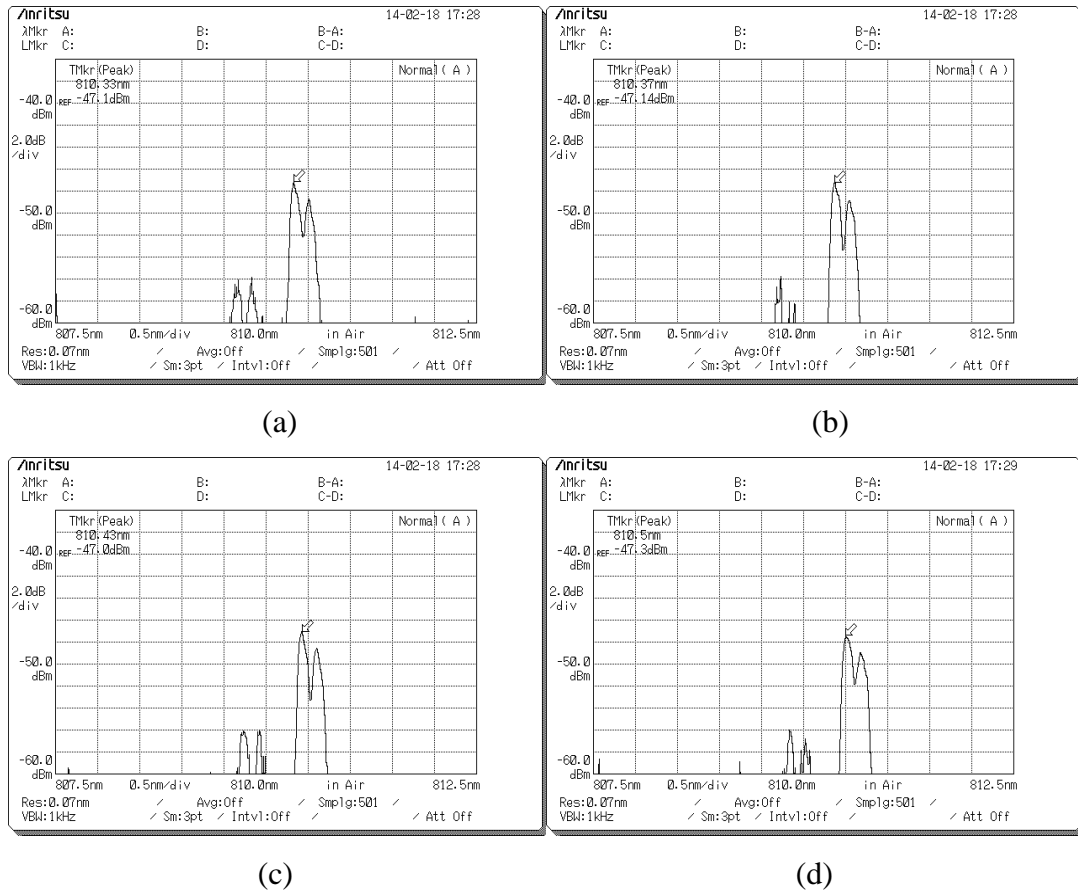
Figure 5.5: OSA screen captures showing fast and slow components reflected by a PM-FBG due to vertical displacement of the mid-point of the aluminum beam by (a) 0, (b) 2mm, (c) 5mm and (d) 8mm.

Table 5.1: Wavelength of fast and slow components with increasing displacement.

Mid-point deflection (mm)	Wavelength Shift of Fast component (nm)	Wavelength shift of slow component (nm)
0	810.33	810.53
2	810.37	810.57
5	810.43	810.63
8	810.50	810.70

By splicing a PM fiber at an angle of 45° to a PM-FBG, the intensities of the two Bragg wavelengths reflected by PM-FBG become sensitive to the elongation in the spliced PM fiber. Figure 5.6 is a schematic of such a spliced PM-FBG and the experimental set up was the same as in Figure 5.3. The spliced PM-FBG was again bonded to the bottom of an aluminum beam as before.
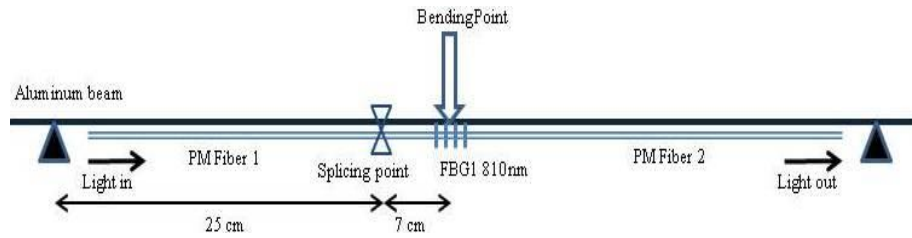
Figure 5.6: Schematic of spliced PM-FBG.

The OSA screenshots (Figure 5.7) show that when a PM fiber is spliced to a PM-FBG, the intensities of the fast and slow Bragg reflections change with changing elongation of the beam. At the same time, the Bragg Wavelengths of the FBG shift. The SOP value as per equation (5.8) is plotted in Figure 5.8. As expected, the SOP value varies sinusoidally with the vertical displacement of the bending point. Also, the SOP must respond only to the strain (elongation) produced in the first section of the PM fiber (before splicing point), but not to strain produced in the second section of the PM fiber (after splicing) as suggested by the equation (5.7). This is because the intensity shown in equation (5.7) is independent of length l_2 and the strain produced in the PM fiber after the FBG does not alter the polarization of light falling on PM-FBG.

(a)   (b)

(c)   (d)
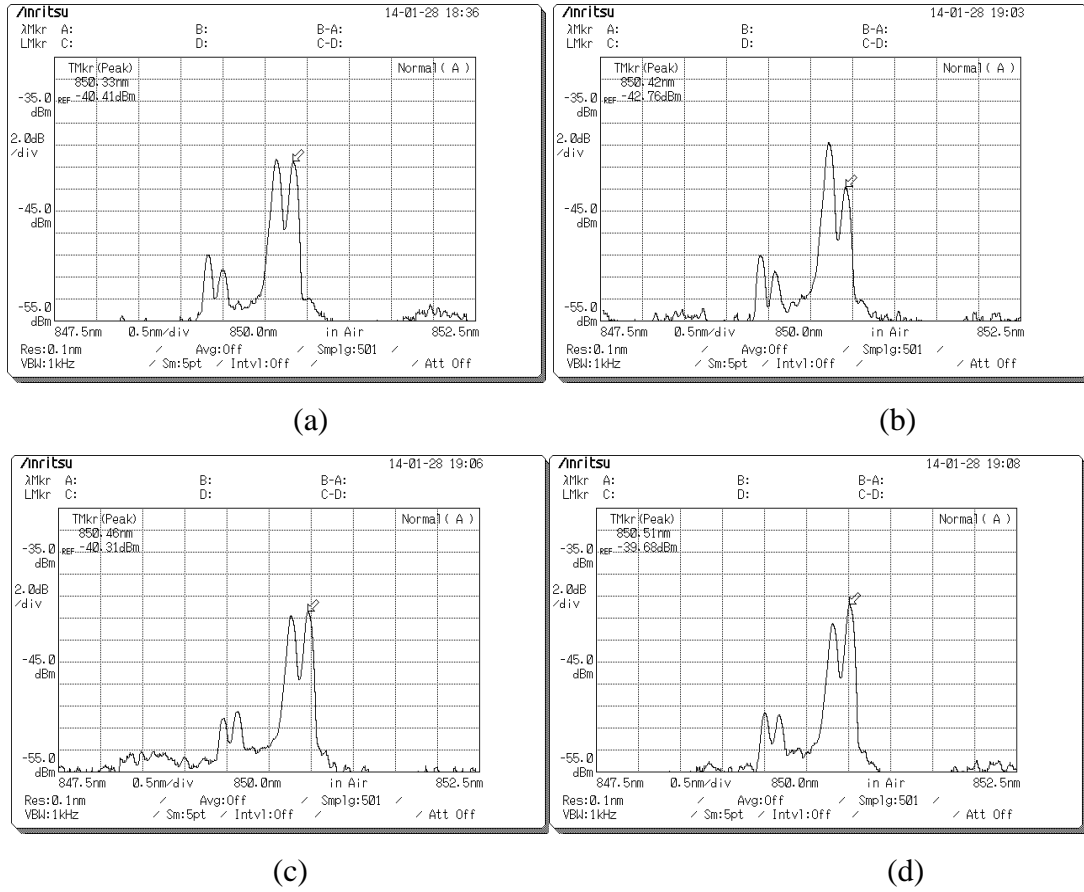
Figure 5.7: OSA shots of the spectrum reflected by the PM-FBG keeping the bending point was at the PM FBG (Figure 5.8) and the vertical displacement at the bending point was (a) 0, (b) 4mm, (c) 6mm and (d) 8mm.
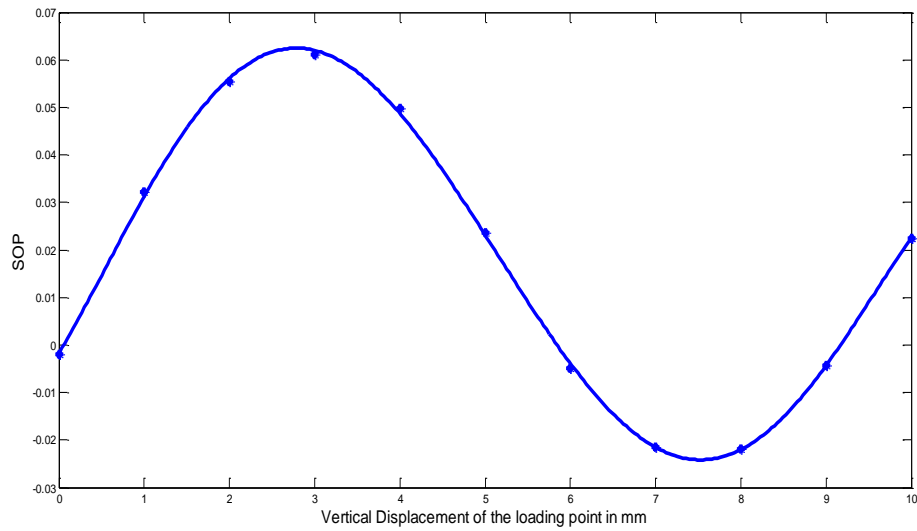
Figure 5.8: SOP for increasing displacement.

This experiment highlights that SOP changes sinusoidally with increasing elongation in the first section of the PM fiber which could be the basis of global structural health monitoring as per the FOPS concept [35]. It is well known that FBGs are sensitive only to damages in their immediate vicinity. Spliced PM-FBG has two sections – a near field FBG sensor to detect cracks locally and a global FOPS sensor which can detect structural anomalies.

5.4. 2 Sensor design for crack location in beam structures

Based on the results of the experiments performed above, a design which is the combination of two sections of PM fiber and two PM-FBGs is proposed herein. This design is capable of detecting a crack irrespective of its location in the beam. This design tells us the approximate location of the crack. The schematic of this sensing system is shown in the Figure 5.9.
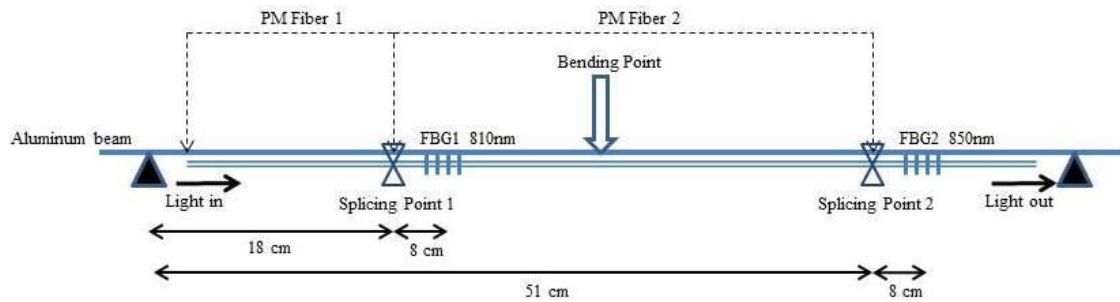
Figure 5.9: Schematic of the design for the detection and approximate location of crack in a beam structure.

In this design two PM-FBGs with Bragg wavelengths of 810nm and 850nm are used. The principal axes (fast and slow axis) of the spliced PM fibers at both the splicing points were misaligned by 45° as it leads to the maximum sensitivity (maximum intensity variation) [35]. The light loss at each splicing point is 0.01-0.05 dB, which is very low and therefore, it allows multiple splicing points without any significant signal loss. The peak of the SOP cycle of PM-FBG1 (810nm) shifts if the damage is on the left side of splicing point1 (or FBG1) and the peak of the SOP cycle of FBG2 (850nm) shifts if the damage is on the left side of splicing point2 (or FBG2), provided that the light is launched into the fiber from the left side. If the crack is on any of the FBGs, there will be a corresponding Bragg wavelength characteristic shift. To understand how this design works, the sensitivity of the Bragg wavelength characteristic of FBG1

was first studied. The beam was bent at its mid-point with the help of a three point bending machine to produce strain in the beam. A crack of size 7mm was made at different points along the beam as shown in the Figure 5.10.

(a)   (b)

(c)
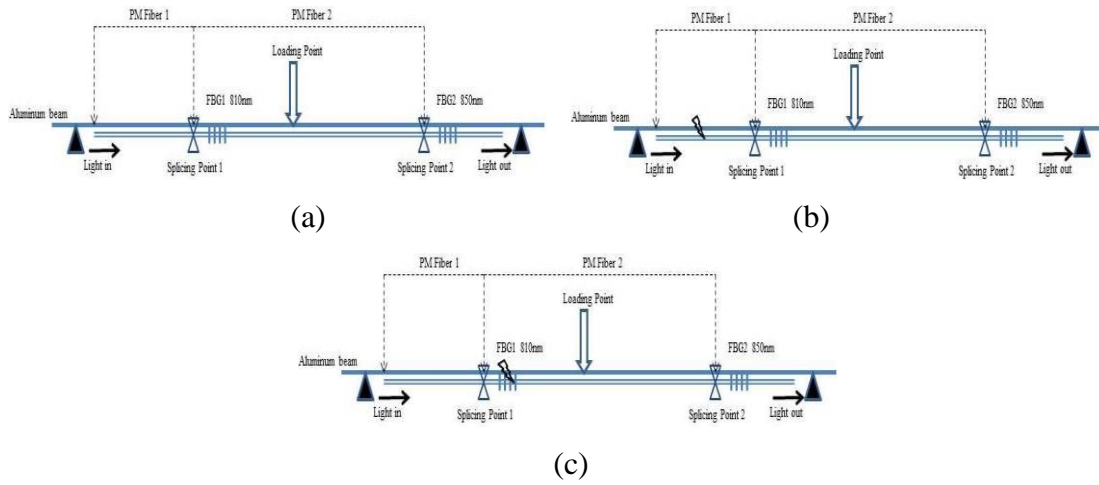
Figure 5.10: Schematic of the proposed design to see how strain-wavelength characteristic of FBG1 responds to the damage at different locations with (a) no crack, (b) one crack at 15 cm to its left and (c) one crack at the FBG1 itself.

The change in the wavelength with the vertical displacement of the mid-point of the beam for different crack locations (Figure 5.11) shows that plots corresponding to a no crack and to a crack located 15 cm to the left of FBG1 (or splicing point1) overlap (gradients being almost the same) i.e. no significant effect of the crack. But when the crack is in the vicinity of FBG1 (either left or right), the slope of the plot differs significantly (maximum gradient) indicating the presence of the crack. For a clearer real structure application assertion, the change in wavelength ($\Delta\lambda$) of an FBG is linearly proportional to the strain and can be easily converted into strain. The range of strain induced at the point of PM-FBG1 during this experiment is about 0-700 $\mu\varepsilon$. The strain experienced on a point of a real structure comes more or less within the same range.
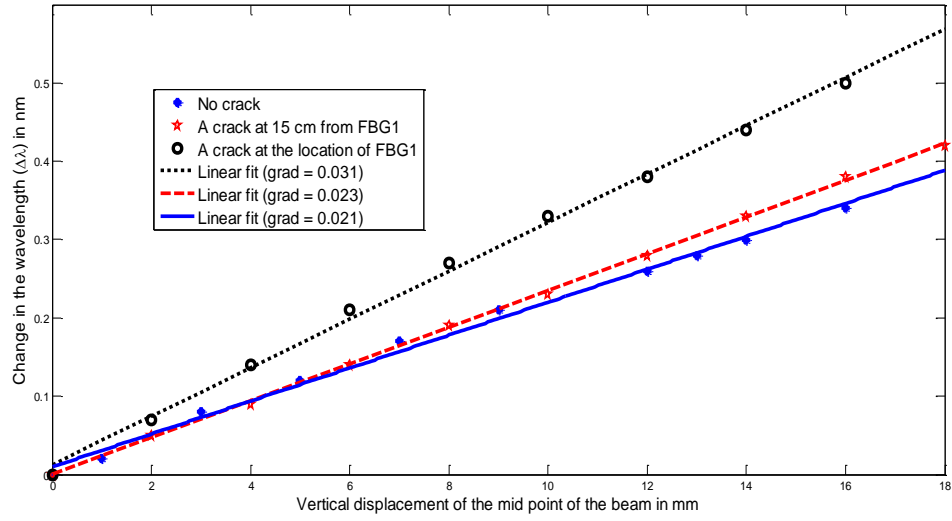
Figure 5.11: Change in the wavelength of FBG1 vs the displacement of the mid-point of the beam with a crack at different locations.

Next, the SOP characteristic of PM-FBG1 was investigated to assess how its cycle varies with the location of damage in the beam. The size of the damage was again kept 7mm. The schematic diagrams for different crack locations are shown in the Figure 5.12. The corresponding SOP cycles are depicted in Figure 5.13. The cycle span for the first case (no crack) is the largest. Clearly, for the second case (a crack at 15cm to the left of FBG1), the cycle span is the smallest, with peak value shifting approximately from 12mm to 9mm of vertical displacement. In the third case (an additional crack at 11cm to the right of FBG1), the peak value of SOP cycle did not shift. It reiterates that the peak of the SOP cycle of FBG1 shifts only if the damage happens on the left side of the FBG1, but is independent of the damage happening on the right side of splicing point 1, as established in equation (5.7). The later damage would be detected by the SOP cycle of FBG2 as it is on the left side of FBG2. In the first case, the amplitude of the SOP cycle seems to be low. This is because a little change in the input polarization angle θ might have changed the amplitude of the SOP cycle (Appendix A), but cycle peak shifts only when there is damage. Now if Bragg wavelength shift and the SOP cycle of FBG1 are to be looked at together, the Bragg wavelength shift responds to the crack close (either left or right) to FBG1 and the peak of the SOP cycle shifts only if the crack on the left side of FBG1 irrespective of the distance of crack from the FBG1. Neither the Bragg wavelength shift nor the peak of the SOP cycle responds if the crack is on the right and far from the FBG1. Hence, with

94

this approach FBG1 can identify and approximately locate the crack if it is on the left side of FBG1.

(a)

(b)

(c)
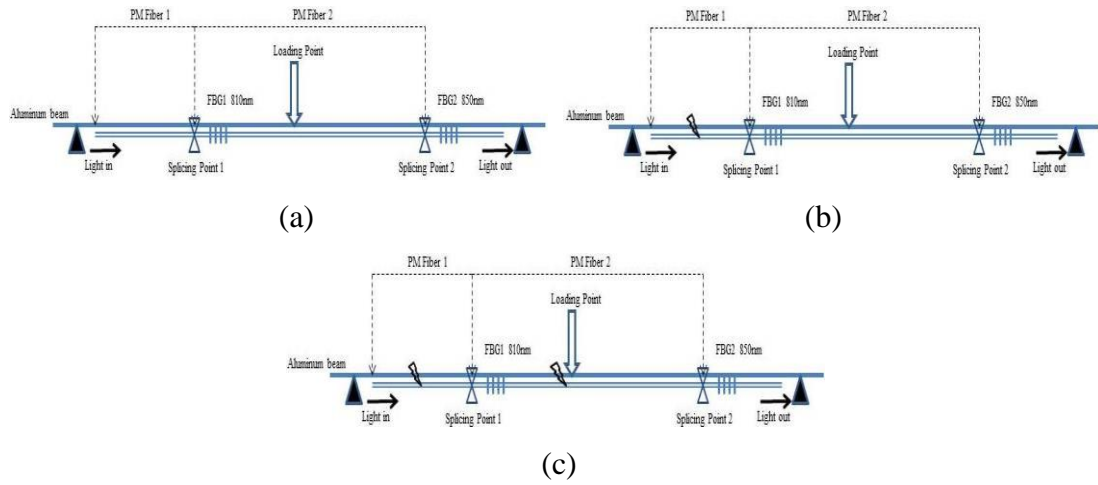
Figure 5.12: Schematic of the design to see the response of the SOP cycle of FBG1 to the damage at different locations with (a) no crack, (b) one crack at 15cm to the left of FBG1 and (c) two cracks, one at 15cm to the left and another at 10 cm to the right of FBG1.
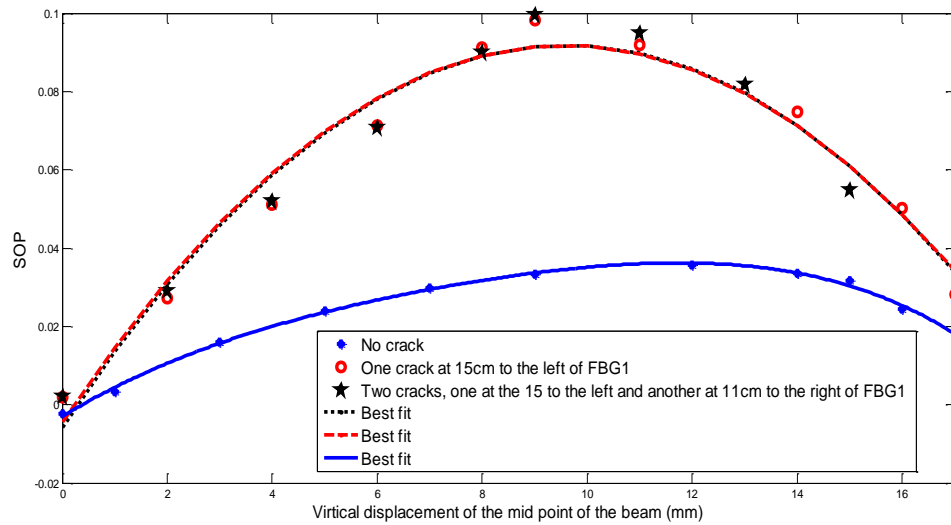
Figure 5.13: The SOP cycles of FBG1 corresponding to different crack positions.

Furthermore, the SOP characteristic of PM-FBG2 was studied to assess how its cycle varies with the damage. For this study, the schematic diagrams corresponding to a no crack condition and to a crack located between both FBGs are shown in Figure 5.14 and in Figure 5.15 the corresponding SOP cycles for the PM-FBG2 are depicted. Clearly, for the second case the SOP cycle has experienced a very significant change,

95

with the peak value shifting nearly from 6.5mm (no crack) to 3.5mm of vertical displacement. Thus, the SOP cycle of PM-FBG2 is reduced when a crack is made at the left-hand side of its splicing point. If the damage is close (either left or right) to the PM-FBG2, the Bragg wavelength will vary.

(a)   (b)
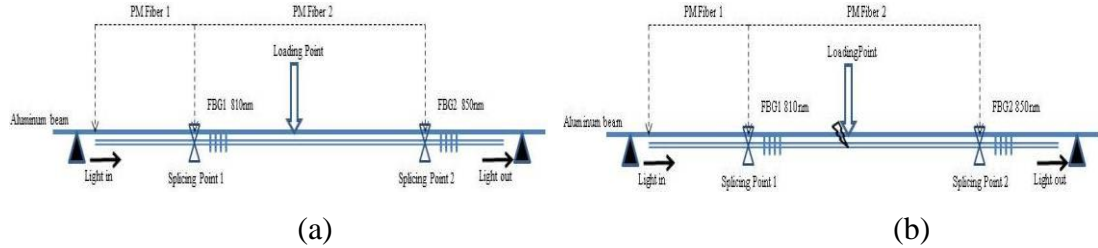
Figure 5.14: Schematic of the design to see the response of the SOP cycle of FBG2 to the damage at different locations with (a) no crack and (c) a crack at 23 cm from FBG2.
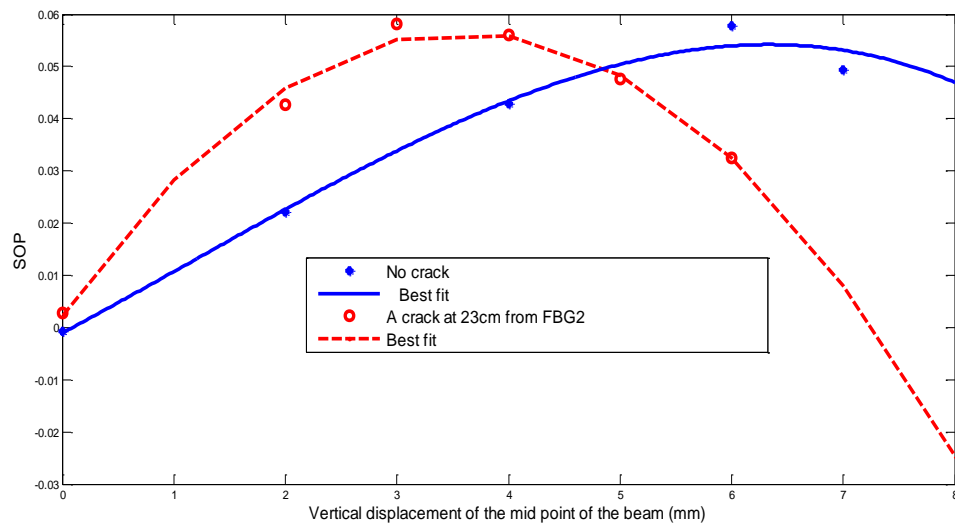
Figure 5.15: The SOP cycles of FBG2 corresponding to different crack positions.

Now both the FBGs (FBG1 and FBG2) together, are able to detect the presence of the damage in the entire beam and they give the approximate location of the damage also. If the Bragg wavelength shift plot of any of the FBGs differs significantly, it means the damage is close (either right or left) to the respective FBG. If the peak of the SOP cycle of FBG1 shifts, it means the damage is on the left side of the FBG1. Similarly, if the peak of the SOP cycle of FBG2 shifts, it means the damage is to the left side of splicing point 2. Finally, if the peak of the SOP cycle of FBG1 does not shift, but that

of FBG2 does, the damage is somewhere between the two FBGs. The length on the right-hand side of FBG2 is about 5-6cm only and if the damage is in this region, the Bragg wavelength shift plot of FBG2 will differ significantly as it has already been mentioned that an FBG's damage detection range (through its Bragg wavelength shift plot) is about 10cm [66]. Thus, this combination of PM fibers and PM-FBGs gives us combined information which we used to get from two different systems; Bragg wavelength shift from the normal FBG interrogation system and the SOP cycle from the FOPS system. In FOPS system, a number of expensive and dedicated optical components are required and their alignment is a very critical issue. This design gives the additional benefit of FOPS with no external optics required and there is no alignment issue at all.

The length from left end to splicing point1 (18cm in Figure 5.9) is the FOPS region for FBG1 and again the length from left end to splicing point2 (51cm in Figure 5.9) is the FOPS region of FBG2. If the damage is in the middle of FOPS region of a particular FBG, the complete additional strain caused by the damage will be contained in that FOPS region and the shift in the peak of the corresponding SOP cycle will be the largest. If the damage is close to the splicing point of a particular FBG, the concerned FOPS region will not contain the additional strain completely, some additional strain will occur in the right-hand side of the same splicing point which is not the FOPS region of the concerned FBG. Therefore, the shift in the peak of SOP cycle will be smaller in this case. The precision in the damage location depends on the distance between both the FBGs. Precision can be improved (8-10cm) by multiplexing more PM-FBGs in the same fashion and by reducing the distance between the consecutive PM-FBGs, which depends on how close the two PM-FBGs can be spliced.

5.5 Summary

Research work presented in this paper increases the scope of FBG in the field of structural health monitoring. The method of spliced PM-FBG is used not only to measure the Bragg wavelength shift (FBG measurement) but also to measure the variation in the SOP cycle (FOPS measurement). Thus PM-FBG combines the global damage monitoring technique and local damage monitoring technique on a single fiber and only FBG experimental setup is used to obtain this combined information. The FOPS instrumentation is no longer required reducing the cost and the complexity of

the experimental set-up. Further, based on this spliced PM-FBG concept, a sensor design is proposed for crack monitoring in beam structures. It can monitor the beam structures globally as well as locally and it is demonstrated that it gives a very strong idea of the crack location in the beam. The working of this sensor design is completely independent of the boundary condition of the beam structure under investigation, therefore, it is implied that this sensor design will work with all beam configurations. Crack location can be obtained with high precision by splicing multiple PM-FBGs; however information about crack size is absent. This spliced PM-FBGs sensor method has a great scope for SHM of two dimensional structures also.

CHAPTER – 6 Combined FBG and FOPS on a single fiber for SHM of two-dimensional structures

It has already been shown in chapter 5 that an FBG written on a Polarizing Maintaining (PM) fiber can discern information from both FBG & FOPS sensors using only one decoding system. This reduces costs and complexities. In this chapter, few properly multiplexed PM-FBG sensors are applied for SHM of an aluminum plate. The results demonstrate that the damage site can be located in two-dimensional structures, like plates using this multiplexed PM-FBG sensing array.

6.1 Introduction

The latest generation smart materials have already surpassed the capabilities of traditional smart materials. These smart materials provide better and effective alternative to traditional structural health monitoring techniques [1]. In the last couple of decades, structural health monitoring (SHM) techniques using sensors are on rise to meet the ever changing demands due to increased construction and manufacturing activities worldwide [93, 94]. The civil/mechanical structures such as bridges, dams; aircraft components such as wings, hulls are constantly subjected to some form of external loading [2]. Almost all these structures are two dimensional in reality and they must be monitored regularly for variations in strain or loading.

Fiber optic sensors (FOS) are one of the latest generation sensors that are being used extensively in the field of SHM. Fiber optic sensors offer a number of advantages over traditional sensors. These include immunity to electromagnetic interference, electrically passive, long term stability, light weight, small size, multiplexing capabilities, ease of installation, durability etc. Fiber optic sensors that have been researched the most so far include fiber Bragg grating (FBG) and fiber optic polarimetric sensors (FOPS). The implementation of FBG sensors at different construction sites [67, 86 &87] proves its value for long term strain monitoring. FBG could monitor a very limited region around them leading to local SHM [66]. FOPS on the contrary is suitable for global SHM [35]. As stated in chapter 5, a combination of

FBG and FOPS are well suited for obtaining local and global SHM information. The combined information would lead to a better picture of damage location and size.

It has already been proved in chapter 5 that a spliced PM-FBG can provide the combined information of FBG and FOPS without any additional experimental set-up for FOPS. In other words, the spliced PM-FBG can provide the local and global structural health information simultaneously. The analysis of results obtained in chapter 5 showed that the combined information obtained from the experiment gives a better and clearer picture of damage site in beam structures. It has already been established that a combination of two PM-FBGs is able to monitor the damage site in beam structures. Here in this research work, more PM-FBGs have been multiplexed and implemented for the SHM of an aluminum plate. The experimental results show that this design (multiplexed PM-FBGs) is capable of providing damage location in two-dimensional structures also.

6.2 Theoretical background

Light gets divided into two components as it enters the high birefringent medium of a PM fiber. One component travels along the fast axis and the other travels along the slow axis. Since the refractive indices are different along fast and slow axes, PM-FBG reflects two Bragg wavelengths; one corresponding to the fast axis ($\lambda_{B,f}$) and another corresponding to slow axis ($\lambda_{B,s}$) [90, 92].
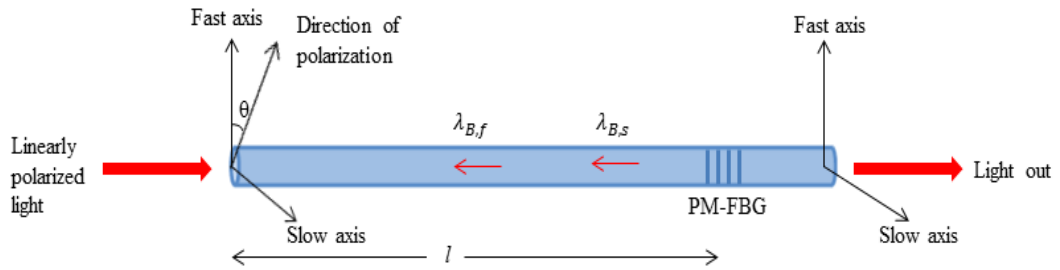
Figure 6.1: Schematic of PM-FBG with linearly polarized light being launched at an angle θ from the fast axis.

In Figure 6.1, linearly polarized light is launched into a PM fiber with an FBG written on its core. The light is launched at an angle θ from the fast axis of the PM fiber. There are two Bragg reflections $\lambda_{B,f}$ and $\lambda_{B,s}$ emerging from PM-FBG corresponding to fast and slow axes as shown in the Figure 6.1. The evolution of intensities of both the

Bragg reflections (fast and slow) during their journey in a high birefringent medium can be expressed by Mueller matrix method [83]. As established in chapter 5, the Mueller matrix of the fast component emerging out of the PM fiber (Figure 6.1) after being reflected by PM-FBG can be written as

$$\begin{bmatrix} S_0^{out} \\ S_1^{out} \\ S_2^{out} \\ S_3^{out} \end{bmatrix}_f = \begin{bmatrix} \left(S_0^{in} + S_1^{in}.\cos2\theta + S_2^{in}.\sin2\theta\right)\cos^2\theta \\ \left(S_0^{in} + S_1^{in}.\cos2\theta + S_2^{in}.\sin2\theta\right)\cos^2\theta \\ 0 \\ 0 \end{bmatrix} \tag{6.1}$$

The Stokes vector given by equation (6.1) corresponds to the fast component. In equation (6.1), S_0^{out} is the intensity of the fast component and clearly, it is independent of the length of the PM fiber. It shows that the longitudinal strain (change in the length of PM fiber) has no effect on the intensity. The intensity is a sine and cosine function of the input polarization angle θ only. Similarly, this can also be proved for the slow component also.
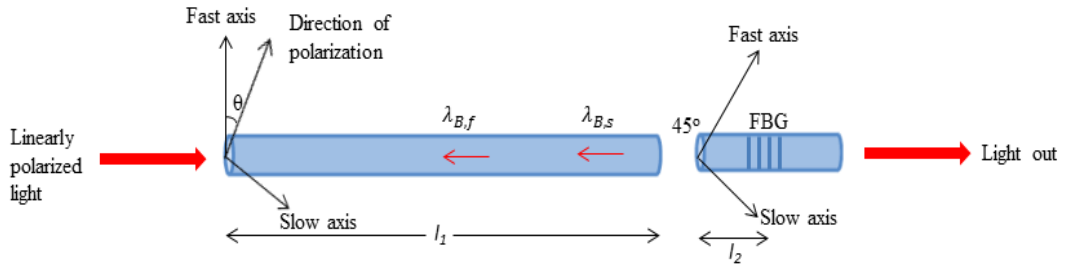
Figure 6.2: Schematic of PM-FBG spliced to PM fiber at an angle of 45° with linearly polarized light being launched at an angle θ from the fast axis.

For the spliced PM-FBG sensor design proposed in chapter 5 (Figure 6.2), the resultant Stokes vector for the fast component emerging out of the PM fiber comes out to be:

$$\begin{bmatrix} S_0^{out} \\ S_1^{out} \\ S_2^{out} \\ S_3^{out} \end{bmatrix} = \begin{bmatrix} \frac{1}{2}\left[\begin{array}{c} \left(S_0^{in} + S_1^{in}cos2\theta + S_2^{in}sin2\theta\right) \\ -\{S_0^{in}sin2\theta + S_1^{in}cos2\theta.sin2\theta + S_2^{in}sin^2 2\theta\}cos\left(\frac{2\pi l_1}{l_b}\right) \end{array} \right] \\ 0 \\ \frac{1}{2}\left[\begin{array}{c} \left(S_0^{in} + S_1^{in}cos2\theta + S_2^{in}sin2\theta\right) \\ -\{S_0^{in}sin2\theta + S_1^{in}cos2\theta.sin2\theta + S_2^{in}sin^2 2\theta\}cos\left(\frac{2\pi l_1}{l_b}\right) \end{array} \right]cos\left(\frac{2\pi l_1}{l_b}\right) \\ -\frac{1}{2}\left[\begin{array}{c} \left(S_0^{in} + S_1^{in}cos2\theta + S_2^{in}sin2\theta\right) \\ -\{S_0^{in}sin2\theta + S_1^{in}cos2\theta.sin2\theta + S_2^{in}sin^2 2\theta\}cos\left(\frac{2\pi l_1}{l_b}\right) \end{array} \right]cos\left(\frac{2\pi l_1}{l_b}\right) \end{bmatrix} \qquad (6.2)$$

From equation (6.2), it is clear that the intensity of the fast component emerging from the PM fiber is a function of length l_1 (before splicing point) of PM fiber or in other words, the intensity is a function of longitudinal stain produced in the length l_1 of PM fiber. The misalignment of 45° makes intensity a sinusoidal function of longitudinal strain. Any deviation from 45° would cause uneven sinusoidal variation of the intensity. Essentially, with this idea, the intensity of the fast component reflected by PM-FBG is a sinusoidal function of longitudinal strain produced in the PM fiber (before the splicing point). Since this part of the PM fiber (length l_1) is far away from the FBG, the Bragg wavelengths are not responsive enough to detect the damage in this region. It has already been shown that the FBGs are useful in damage detection only if the damage is in the vicinity of the FBG (around 10 cm) [66]. However the intensity is not the function of longitudinal strain produced in the PM fiber on which the FBG is written (length l_2). If the intensities of both the Bragg reflections are known, the SOP value can be calculated as [35]:

$$SOP = (I_f - I_s)/(I_f + I_s) \qquad (6.3)$$

where I_f and I_s are the intensities of the fast and slow Bragg reflections.

Since intensities of both the Bragg reflections vary sinusoidally with the increasing longitudinal strain in the PM fiber, the state of polarization (SOP) will also vary sinusoidally with longitudinal strain which is similar to conventional Fiber Optic Polarimetric Sensors (FOPS) [35]. In other words, the intensities are the sinusoidal function of the load that is put on the structure which in fact produces strain in the structure. This sensor design can easily be bonded or embedded in any structure. If damage occurs in the region of length l_1 of a particular structure, the stiffness of this

part of the structure will go down. This will result in the increased longitudinal strain with the same load. Thus, in case of damage in the region l_1, the SOP will change faster with increasing load than it does in case of no damage. In other words, the period of SOP cycle will reduce in case of damage. Since the intensities (I_f & I_s) are independent of length l_2, it can be said that the SOP cycle of a particular PM-FBG reduces only if the damage is in front of the splicing point of that PM-FBG. Though the intensities vary with input polarizations angle θ too, the change in θ does not alter the period of SOP cycle. Only the damage in the part of length l_1 of PM fiber would change the cycle period. Thus, by this experimental approach, FOPS experimental set up is not required to calculate SOP as it can be calculated by using the FBG experimental set up only. Thus, both local and global structural health information can be obtained by conventional FBG set up only.

6.3 Experiments and Results

An experiment was performed to show that intensities of both the Bragg wavelengths of PM-FBG oscillate with increasing longitudinal strain. A grating was inscribed on the core of a PM fiber using the Excimer laser (248 nm) and a phase mask to reflect a Bragg wavelength of 1560 nm. This PM-FBG was then spliced with another PM fiber at an angle of 45° as shown in the Figure 6.2. This spliced PM-FBG was further bonded at the bottom of an aluminum plate along its length and a simple static loading test was performed through a hanger. The hanger was placed in the middle region of the plate as shown in the Figure 6.3. The weight of the hanger was 300g. Further, 500g weights were put one by one on the hanger to produce longitudinal strain in the plate and in the PM fiber bonded to the plate. The two Bragg wavelengths corresponding to fast and slow axes of the PM fiber are shown in Figure 6.4. The beat length of the PM fiber used in this experiment was approximately 5mm. The fast and the slow Bragg wavelengths of these PM-FBGs differ by 0.37nm (theoretically 0.33nm) as shown in the Figure 6.4. The responses of the fast and the slow Bragg wavelengths to this static loading test are shown in the Figure 6.4(a)-(f). This test was performed at room temperature and the temperature was constant during the entire test.

Figure 6.3: Experimental set up to test the response of PM-FBG under longitudinal strain.

(a)   (b)   (c)

(d)   (e)   (f)
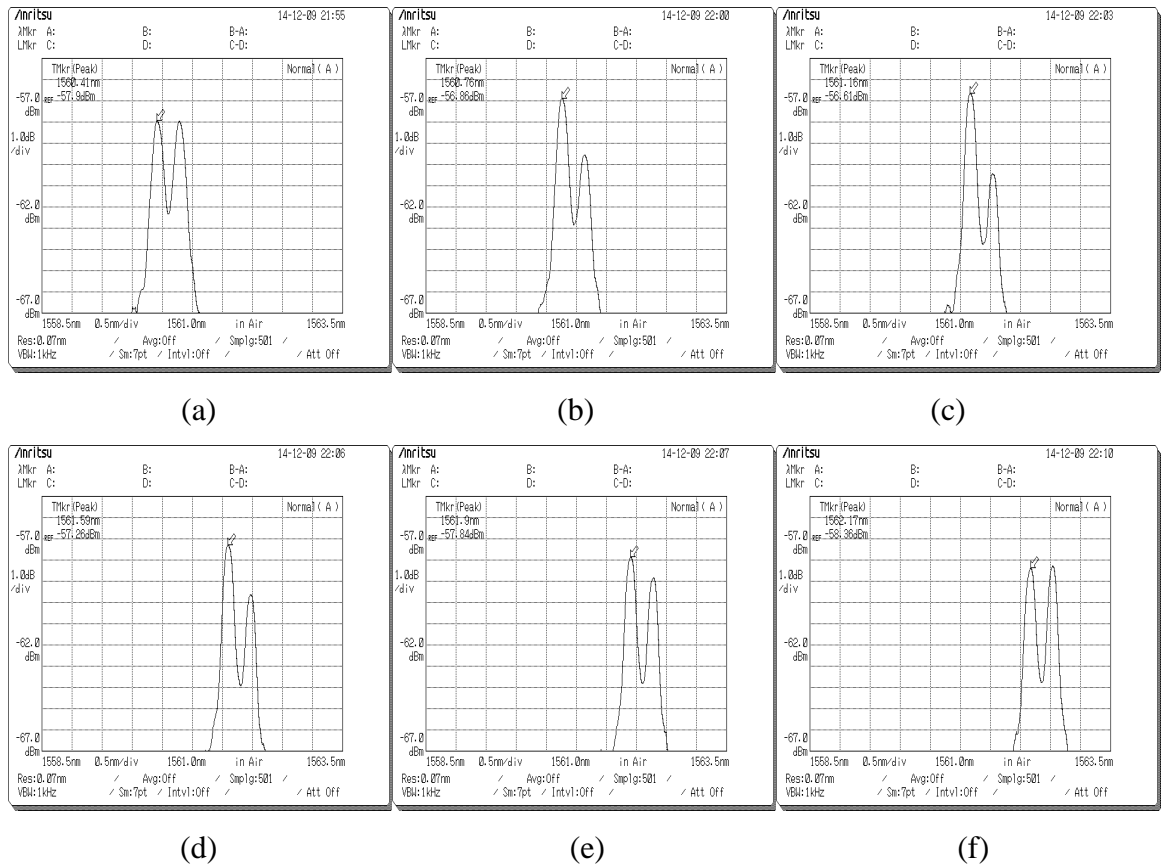
Figure 6.4: OSA shots of the spectrum reflected by the PM-FBG when a load of (a) 0, (b) 1300g, (c) 2800g, (d) 4300g, (e) 5300g and (f) 6300g was put on the plate through the hanger.

In Figure 6.4(a)-(f), the Bragg wavelengths shifted to longer wavelengths with increasing load is expected of a normal FBG. The intensities of Bragg reflections were

found to vary sinusoidally with increasing loads as given by equation (6.3). This information, which facilitates global SHM, is a response expected of FOPS. Thus, PM-FBGs can be used for both local and global SHM simultaneously.

6.4 Sensor design for crack monitoring in 2-D structures

Further, it has been demonstrated that this idea of spliced PM-FBG gives enough information to assess the health of two dimensional objects. Three FBGs were written on a PM fiber using different phase masks to reflect the Bragg wavelengths of 1560nm, 1541nm and 1566nm. These three PM-FBGs (FBG1=1560nm, FBG2=1541nm and FBG3=1566nm) were spliced together with a splicing angle of 45° at every splicing point. The PM-FBGs were spliced at certain distances from each other keeping the dimensions of the plate in mind. These spliced PM-FBGs were then bonded to the bottom of the aluminum plate in a way as shown in Figure 6.5. This arrangement was used to study the effect of side cracks on the intensities of Bragg wavelengths of these three PM-FBGs. The schematic of the specimen plate along with all the spliced PM-FBGs is shown in Figure 6.6. The size of the aluminum plate was 45X15X0.3 cm^{3}. The plate was simply supported and the load was applied at the mid-point of the plate via a hanger. The experimental setup was the same as shown in the Figure 6.3.
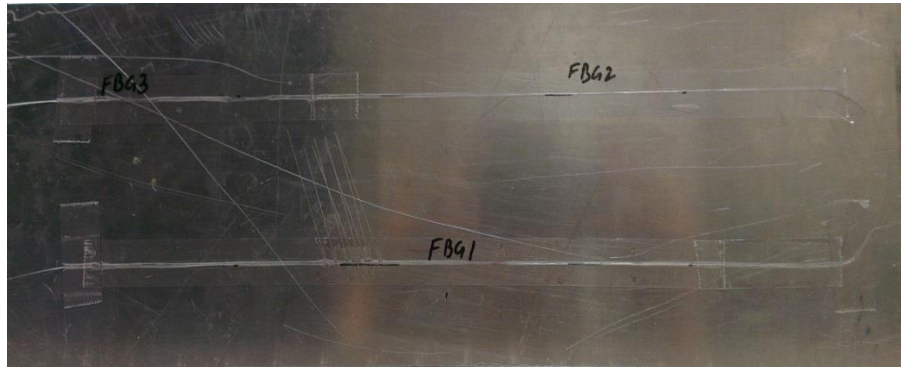
Figure 6.5: Aluminum plate bonded with three PM-FBGs at the surface.
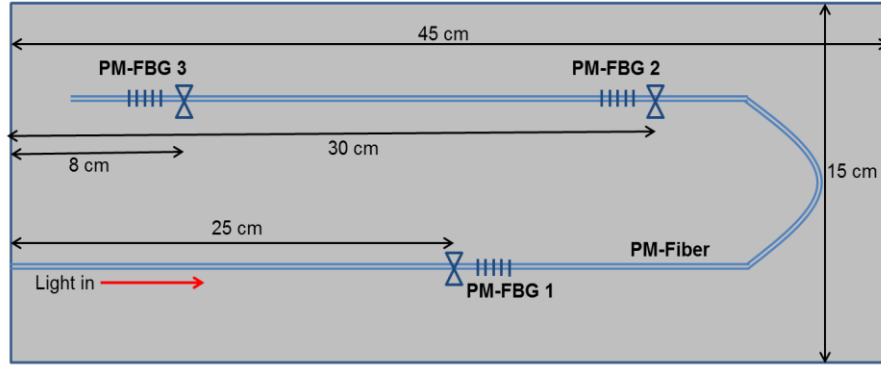
Figure 6.6: Schematic of the aluminum plate bonded with three PM-FBGs at the surface to study side cracks.

The load was increased step by step and the SOP cycles of all the PM-FBGs were plotted. Furthermore, side-cracks (about 2.5 cm each) were made at different locations as depicted in Figure 6.7. For every case depicted in Figure 6.7, the corresponding SOP cycles for PM-FBG1 are shown in Figure 6.8. For the same crack scenarios (Figure 6.7), the SOP cycles for PM-FBG2 and PM-FBG3 are shown in the Figure 6.9 and Figure 6.10 respectively.
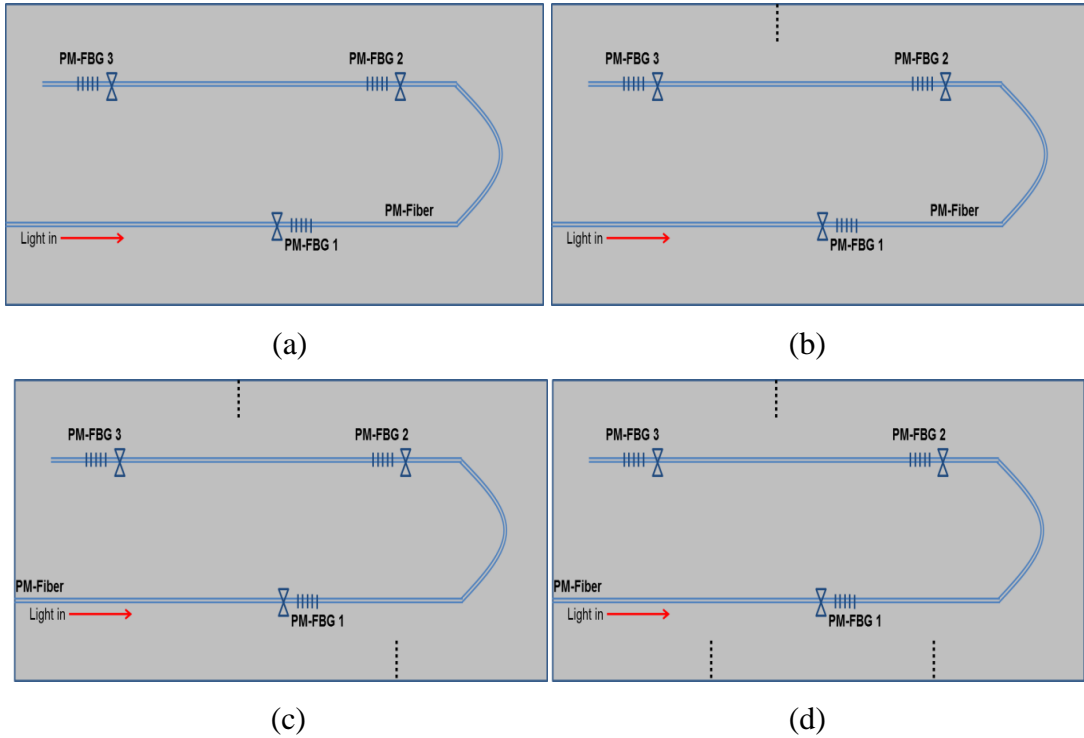
Figure 6.7: Aluminum plate with (a) no crack, (b) a crack before PM-FBG3, (c) two cracks, first before PM-FBG3 and second before PM-FBG2 and (d) three cracks, first before PM-FBG3, second before PM-FBG2 and third before PM-FBG1.

Figure 6.8: SOP cycles of PM-FBG1 for different crack scenarios depicted in Figure 6.7(a)-(d).

Figure 6.9: SOP cycles of PM-FBG2 for different crack scenarios depicted in Figure 6.7(a)-(d).

Figure 6.10: SOP cycles of PM-FBG3 for different crack scenarios depicted in Figure 6.7(a)-(d).

Mathematically, it has already been proved that the SOP cycle of a particular PM-FBG reduces only due to a damage which is in front (left side) of the splicing point of that PM-FBG. The damages that are after (right side) the splicing point have no effect on the SOP cycle of that PM-FBG. Figure 6.8 shows that the SOP cycles of PM-FBG1 for the crack scenarios shown in Figure 6.7(a) (no crack), in Figure 6.7(b) (one crack) and in Figure 6.7(c) (two cracks) are almost the same. This is because of the fact that the cracks in the case of Figure 6.7(b) and Figure 6.7(c) are after (right side) the splicing point of PM-FBG1. For the crack scenario depicted in Figure 6.7(d), since one crack is before the splicing point of PM-FBG1, the SOP cycle reduced clearly (the highest point of SOP cycle being moved from 2800 g to 1800 g). Similarly, the SOP cycle of PM-FBG2 did not reduce due to the crack shown in Figure 6.7(b) as it is after the splicing point of PM-FBG2. The SOP cycle of PM-FBG2 reduced for crack scenario shown in Figure 6.7(c) as one of the cracks is before the splicing point and it reduced even further in the case of Figure 6.7(d) due to the occurrence of an additional crack before the splicing point. The SOP cycle of PM-FBG3 further reduced for crack scenarios shown in Figures 6.7(b)-(c) as all the additional cracks are before the splicing point of PM-FBG3. For every crack scenario shown in Figures 6.7(a)-7(d), the loads required for the complete SOP cycles of all the PM-FBGs can be extrapolated from the points that are there in Figures 6.8, 6.9 and 6.10. The load values for the complete SOP cycles will be four times the load values at which the highest point of

SOP cycles of PM-FBG1, 2 and 3 (shown in Figures 6.8, 6.9 and 6.10 respectively) are achieved. This is because at these highest points, only a quarter of a full SOP cycle is achieved. These load values are shown in table 6.1. These observations reinstate that the SOP cycle of a particular PM-FBG reduces only if the damage is before the splicing point of that PM-FBG. The interpretations of these results infer that if the damage is before the splicing point of PM-FBG1, SOP cycles of all the PM-FBGs will reduce. If the damage is after the splicing point of PM-FBG1, but before the splicing point of PM-FBG2, only the SOP cycles of PM-FBG2 & PM-FBG3 will reduce. Similarly, if the damage is after the splicing point of PM-FBG2, but before the splicing point of PM-FBG3, only the SOP cycle of PM-FBG3 will reduce.

Table 6.1: The loads required for the complete SOP cycles of all the PM-FBGs for crack scenarios shown in Figure 6.7(a)-(d).

Number of cracks	Load required for a full SOP cycle of PM-FBG 1	Load required for a full SOP cycle of PM-FBG 2	Load required for a full SOP cycle of PM-FBG 3
0 (Figure 6.7(a))	11200 g	9200 g	5600 g
1 (Figure 6.7(b))	11200 g	9200 g	4400 g
2 (Figure 6.7(c))	11200 g	7200 g	3600 g
3 (Figure 6.7(d))	7200 g	3200 g	-

Another experiment with a similar aluminum plate was conducted to study the effect of damage present in the mid-region of the plate (between both the fiber lines) on SOP cycles. A PM-FBG arrangement similar to Figure 6.6 was again placed on the plate. The schematic of this arrangement is shown in the Figure 6.11. In this experiment, cracks were made close to the bisecting line (along the length) as shown in the Figure 6.12(b) and Figure 6.12(c).
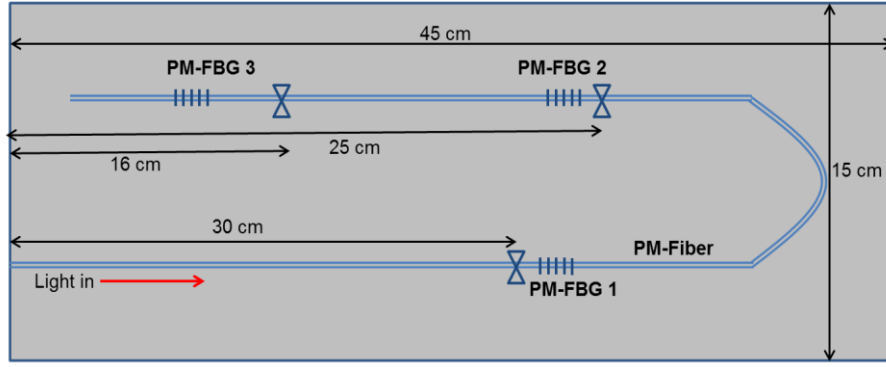
Figure 6.11: Schematic of the aluminum plate bonded with three PM-FBGs at the surface to study mid-plate cracks.

(a)

(b)

(c)
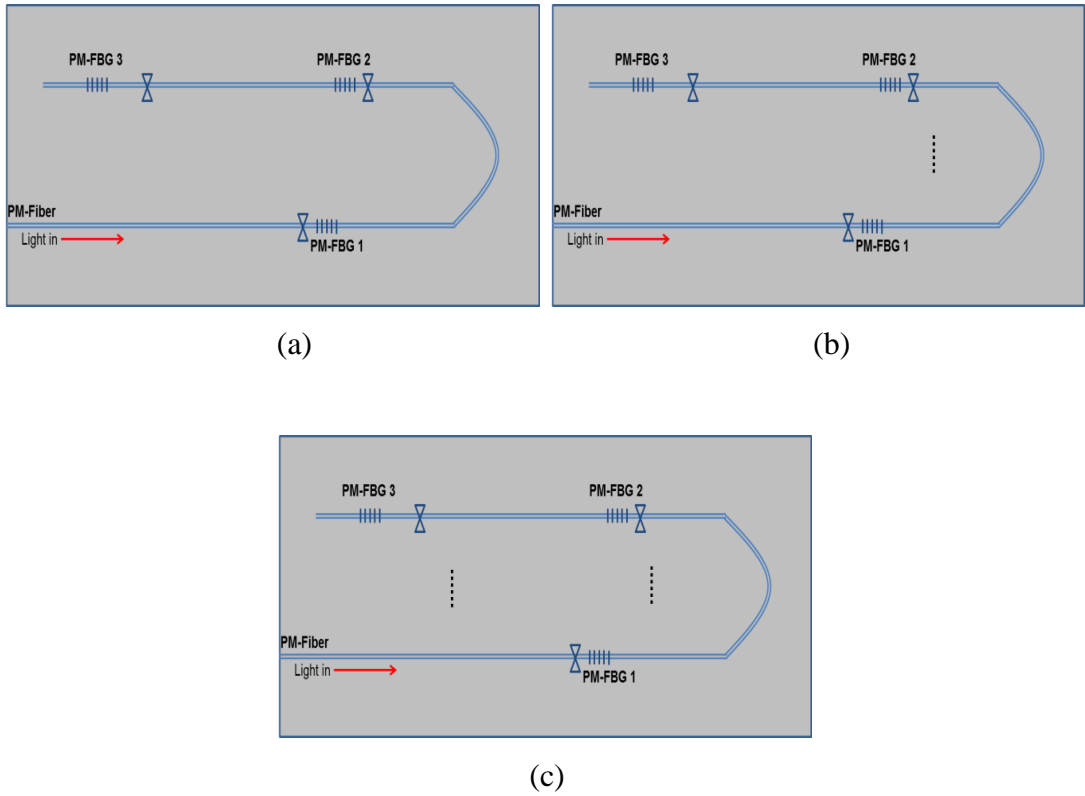
Figure 6.12: Aluminum plate with (a) no crack, (b) a crack before PM-FBG2 and (c) two cracks, first before PM-FBG2 and second before PM-FBG3.

The similar loading test was again performed to see the responses of SOP cycles of PM-FBG1, PM-FBG2 and PM-FBG3 to the crack scenarios depicted in Figure 6.12. The responses of SOP cycles of PM-FBG1, PM-FBG2 and PM-FBG3 to all the crack scenarios presented in Figure 6.12 are shown in Figure 6.13, Figure 6.14 and Figure 6.15 respectively. The SOP cycles of PM-FBG1 (Figure 6.13) for no crack (Figure 6.12(a)) and for one crack (Figure 6.12(b)) were almost the same as the crack shown in

Figure 6.12(b) is behind the splicing point of PM-FBG1. When an additional crack was made before the splicing point of PM-FBG1 (Figure 6.12(c)), the SOP cycle reduced (the highest point of SOP cycle moved from 1800 g to 1000 g). Similarly, the SOP cycle of PM-FBG2 (Figure 6.14) reduced because of the crack shown in Figure 6.12(b) and it reduced even further due to an additional crack shown in the Figure 6.12(c) as both the cracks are before the splicing point of PM-FBG2. Similar to PM-FBG2, the SOP cycle of PM-FBG3 reduced more and more for crack scenarios shown in Figure 6.12(b) and Figure 6.12(c) as all the cracks are before the splicing point of PM-FBG3. For every crack scenario shown in Figure 6.12(a)-(c), the loads required for the complete SOP cycles of all the PM-FBGs can be extrapolated from the data points shown in Figures 6.13, 6.14 and 6.15. The load values for the complete SOP cycles will be four times the load values at which the highest points of SOP cycles of PM-FBG1, 2 and 3 (shown in Figures 6.13, 6.14 and 6.15 respectively) are achieved. These load values are shown in table 6.2. The interpretations of these results again suggest that the SOP cycle of a particular PM-FBG reduces only if the damage is before the splicing point of that PM-FBG. From these observations it can be inferred that if the damage is before the splicing point of PM-FBG1, SOP cycles of all the PM-FBGs will reduce. If the damage is after the splicing point of PM-FBG1, but before the splicing point of PM-FBG2, SOP cycles of PM-FBG2 & PM-FBG3 will reduce while that of PM-FBG1 will not. Hence this design is capable of detecting the damage present within the plate also.
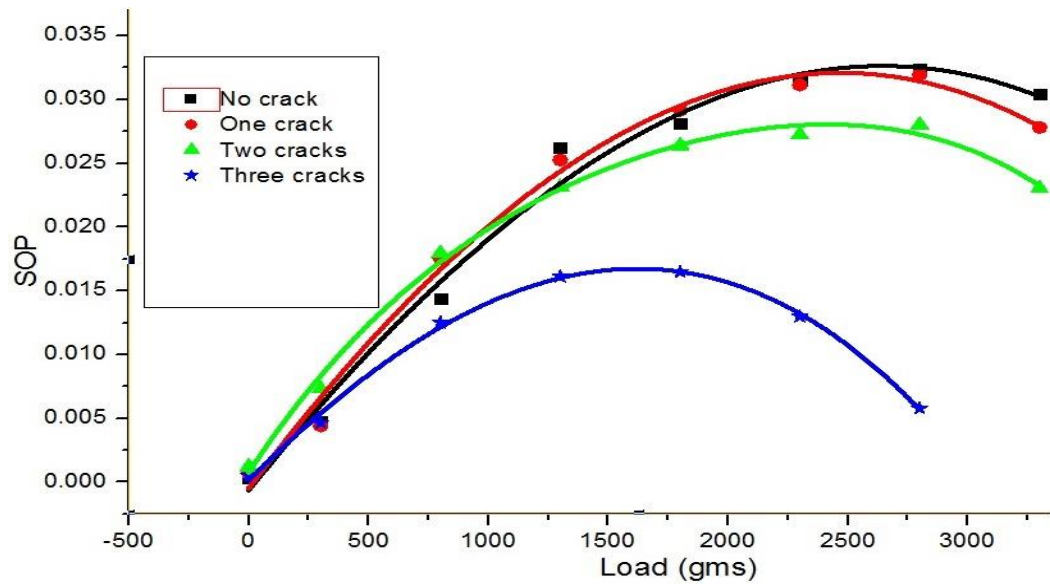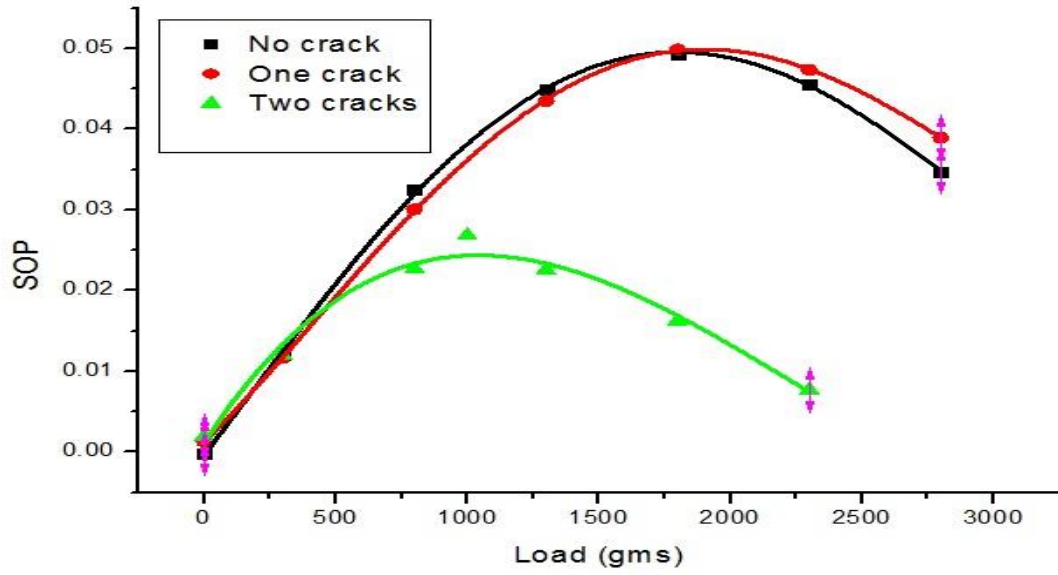
Figure 6.13: SOP cycles of PM-FBG1 for different crack scenarios depicted in Figure 6.12(a)-(c).
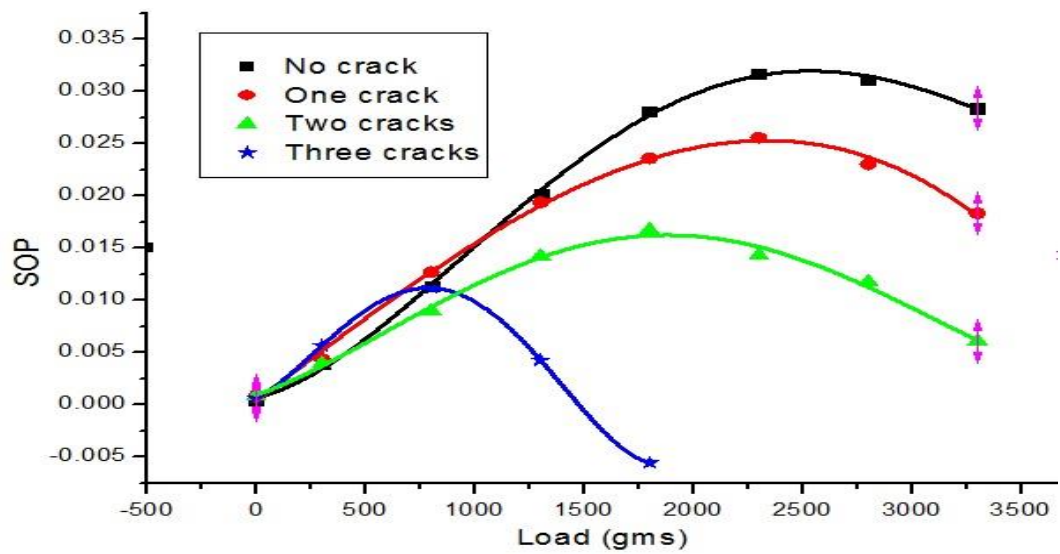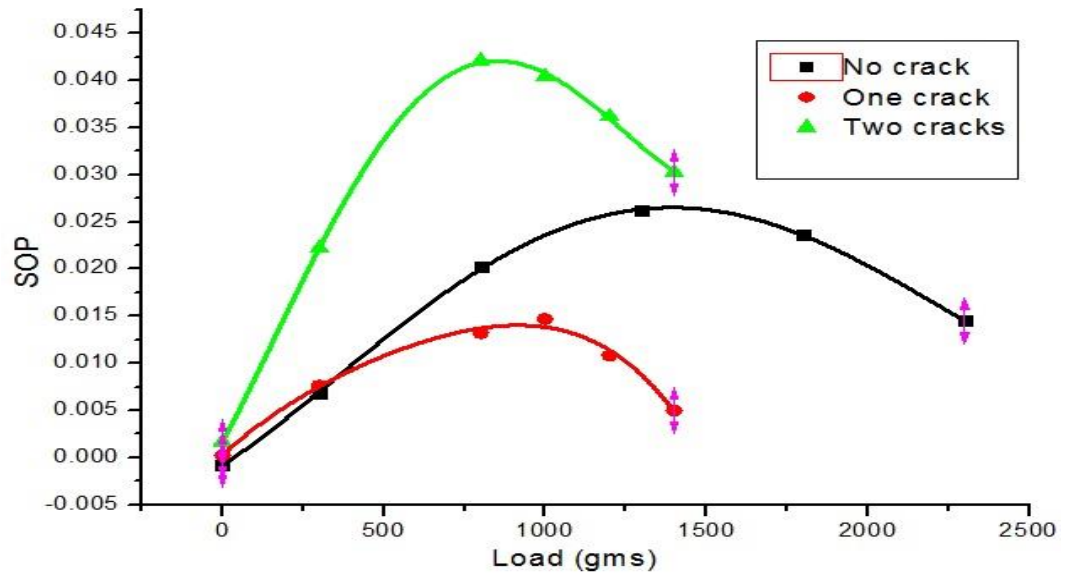

Figure 6.14: SOP cycles of PM-FBG2 for different crack scenarios depicted in Figures 6.12(a)-(c).
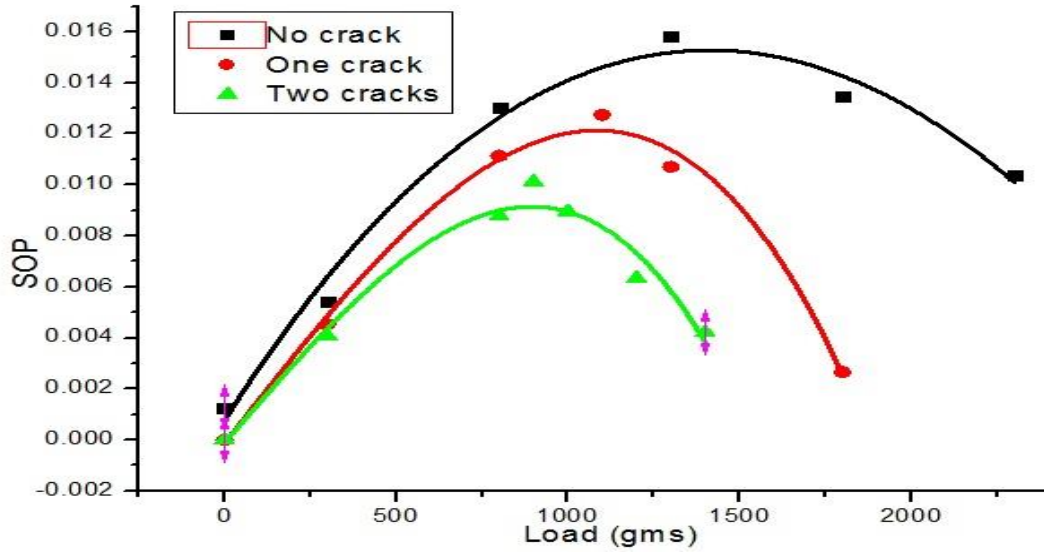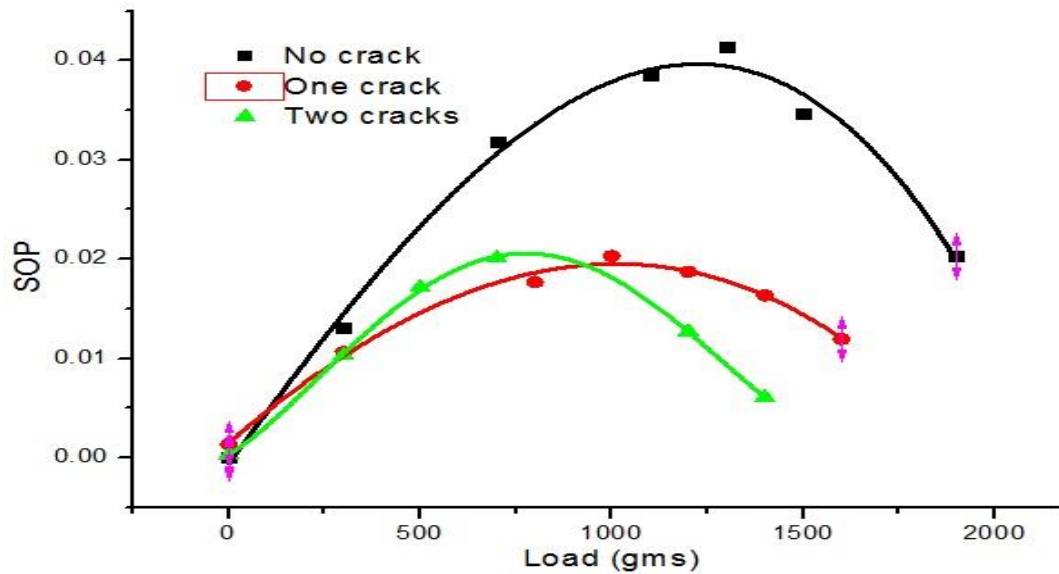
Figure 6.15: SOP cycles of PM-FBG3 for different crack scenarios depicted in Figures 6.12(a)-(c).

Table 6.2: The loads required for the complete SOP cycles of all the PM-FBGs for crack scenarios shown in Figure 6.12(a)-(c).

Number of cracks	Load required for a full SOP cycle of PM-FBG 1	Load required for a full SOP cycle of PM-FBG 2	Load required for a full SOP cycle of PM-FBG 3
0 (Figure 6.12(a))	7200 g	5400 g	5000 g
1 (Figure 6.12(b))	7200 g	4000 g	4000 g
2 (Figure 6.12(c))	4000 g	3200 g	2800 g

The results of experiments conducted in this work suggest that the approximate location of the crack can be determined just by looking at the SOP cycles of all three PM-FBGs. If the loads required by all the three PM-FBGs to complete their SOP cycles decrease, it will mean that the crack is before the splicing point of PM-FBG1. If the loads required by PM-FBG2 and PM-FBG3 to complete their SOP cycles decrease while the load required by PM-FBG1 to complete its SOP cycle remains the same, it will mean that the crack is before the splicing point of PM-FBG2 (but after the splicing point of PM-FBG1). Finally, if the load required by PM-FBG3 to complete its SOP cycle decreases only, it will mean that the crack is before the splicing the point of PM-FBG3 (and also, after the splicing point of PM-FBG2). The difficulty in crack

113

detection lies in the region after the splicing point of PM-FBG3. This region (after the splicing point of PM-FBG3) can be divided into two lateral parts; the mid-region (between both the fiber lines, laterally) and the side region (laterally). If there is a crack in the mid-region (between both the fiber lines) after the splicing point of PM-FBG3, it will be picked up by the reduction in SOP cycle of PM-FBG1 as the crack would be close enough to the PM fiber of PM-FBG1 to be considered before the splicing point of PM-FBG1. Of course, the SOP cycles of PM-FBG2 and PM-FBG3 will also follow subsequently. If there is any crack in the side-region after the splicing point of PM-FBG3, none of the SOP cycle will respond, as this crack will be after all the PM-FBGs and also far from the PM fiber of PM-FBG1.Thus, the SOP cycles of all the three PM-FBGs can monitor the location of the crack in the plate if the crack is anywhere but in the side-region and after the splicing point of PM-FBG3. On the other hand, if there is a side crack after the splicing point of PM-FBG3, it should be detected by the Bragg wavelength shift characteristic of PM-FBG3 as this crack would be close to PM-FBG3. To show this, an additional experiment was conducted in which an additional side crack was made after PM-FBG3, as shown in the Figure 6.16. The Bragg wavelength shift characteristic of PM-FBG3 for different crack scenarios shown in Figure 6.12(a)-6.12(c) and Figure 6.13 is shown in Figure 6.17. Clearly, the gradient of Bragg wavelength shift vs load line increases significantly only when the crack is close to PM-FBG3 (Figure 6.16). In other cases (Figures 6.12(a)-(c)), the gradient remains almost the same. Hence, if there is damage in the side region (laterally) after the splicing point of PM-FBG3, it will be taken care of by wavelength characteristic of PM-FBG3. Similarly, if the crack is close to any other PM-FBG, the gradient of Bragg wavelength shift vs load line related to that PM-FBG will increase significantly. This is in fact providing local SHM, which normal FBGs provide. Thus, this design is not only giving information about the damage location in the plate through reduction in SOP cycles (FOPS action for global SHM), but also through the increase in the gradient of wavelength shift vs load line (FBG action for local SHM) if the damage is close to any of the PM-FBG. To sum up, this arrangement is capable of locating the damage in the entire plate irrespective of their distances from the PM-FBGs.

The precision in the damage location depends on the distance between the consecutive PM-FBGs. Precision can be improved (5-10 cm) by multiplexing more PM-FBGs in the same fashion and by reducing the distance between the consecutive PM-FBGs,

which depends on how close the two PM-FBGs can be spliced. The tendencies of the results obtained tell that more PM-FBGs could be multiplexed together to get improved damage information in a bigger and practical two dimensional structure. Based on the results obtained in this research work, this sensor design has a great scope to be investigated further for crack detection in real civil and mechanical structures.
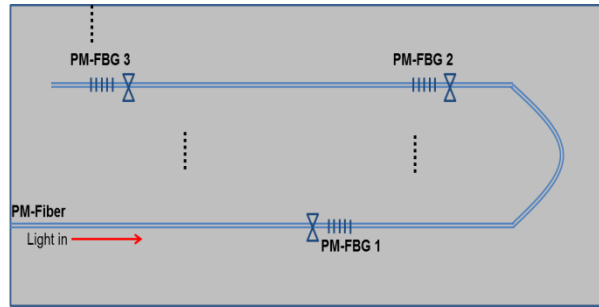
Figure 6.16: Aluminum plate with an additional crack after PM-FBG3.
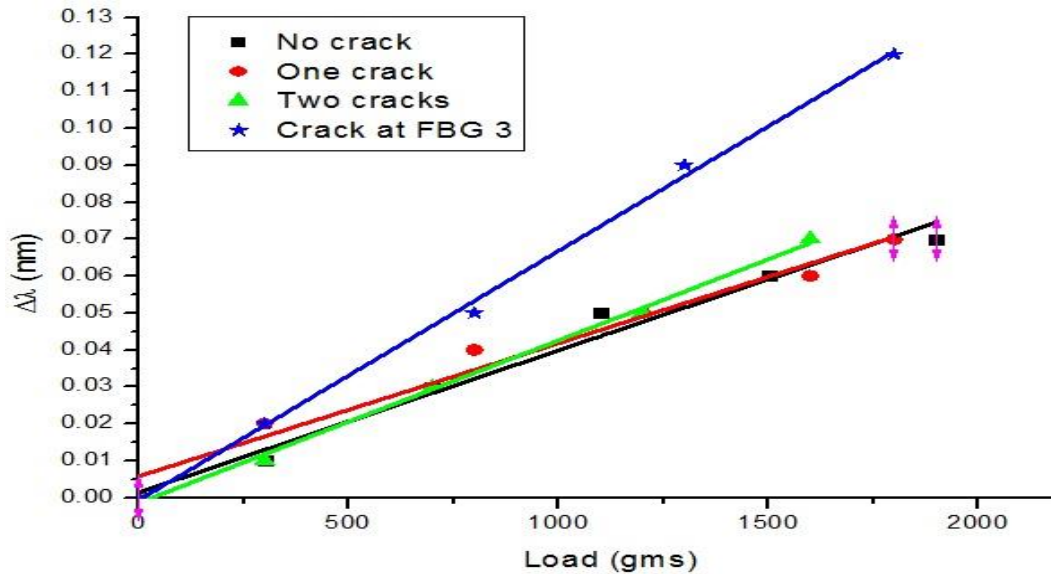
Figure 6.17: Change in the wavelength of PM-FBG3 vs load with different crack locations as shown in Figures 5.12(a)-(c) and Figure 5.16.

6.5 Summary

In this paper, the scope of the idea using PM-FBG for SHM has been extended to two dimensional structures. In the previous work it was limited to one dimensional structure only, like beams. This PM-FBG arrangement provides the combined

information of FBG and FOPS. This combined information facilitates local SHM through Bragg wavelength shift, and global SHM through SOP cycle variation. This PM-FBG sensor configuration not only marks the presence of damages in the plate but also locates them. From the results it can be concluded that this sensor design is suitable for locating damages in two dimensional structures. Since no boundary condition mathematics is involved in the working of this sensor design, it must work for all two dimensional structures with any configuration. It is noted that this design cannot provide any information about damage size. This sensor configuration can be extended by multiplexing more PM-FBGs together to find damage locations in large structures. The research work presented here leaves significant scope for this sensor design to be further investigated.

CHAPTER 7 Wavelength shifted chirped FBGs for combined FBG and FOPS action

In this chapter, a wavelength shifted chirped FBG (CFBG) sensing system has been demonstrated. This intensity based CFBG sensing system abrogates the need for optical spectrum analyzer (OSA) and presents a cost effective, compact and high resolution sensing module which can measure positive/negative strain and temperature simultaneously. This sensing module can perform dynamic FOPS measurement too, thus giving FBG + FOPS data. In other words, the FBG and FOPS can be realized on a single fiber in this sensing module.

7.1 Introduction

Fiber Bragg Grating (FBG) sensors are used in a variety of applications ranging from damage detection in composites [50] to dynamic structural strain monitoring on Hong Kong's Tsing Ma bridge [67] to long term strain monitoring in the construction industry [86, 87]. FBGs are also used as temperature sensors, pressure sensors etc. [95-97] with a very high measurement accuracy. The most genuine problem which FBGs face is the bulkiness and cost of its interrogation system which is an optical spectrum analyzer (OSA). These problems limit the application area of FBG.

Several FBG interrogation system designs have been proposed which rule out OSA, but they are only partially promising. A matched-filter interrogation was demonstrated for strain measurement. Identical gratings are used as notch filters in this system [98]. These notch filters are mounted on small stretching devices driven by piezoelectric (PZ) stacks. It makes this technique complicated and it limits the strain measurement range of the system to ±200με also. Mechanical strain amplification is needed to expand the range, which makes the system even more complicated. An FBG demodulation system utilizing tunable Fabry-Perot wavelength filter was developed [99]. Again, a piezoelectric transducer is used to adjust the cavity spacing in the Fabry-Perot wavelength filter. It makes this system intricate and dependent on the performance of an electrical component, like piezoelectric transducer. A passive wavelength demodulation system was demonstrated which uses a commercial infrared high pass filter [100]. The resolution of this system is very poor (around 400με). One

other reported system employs an asymmetric grating as a wavelength-to-amplitude converter for linear sensing structures [101]. The asymmetric grating employed in this technique is difficult to fabricate. In an another low cost FBG interrogation system, a long period grating (LPG) was used as an edge filter converting strain-induced wavelength variation into optical power measurement [102]. The problem with this interrogation system is that LPGs are extremely sensitive to external perturbations, like temperature, strain etc. Moreover, LPGs are known for their very high sensitivity to the refractive index of the surrounding medium.

An FBG demodulation method using UV-induced birefringence of optical fiber was presented. To interrogate the wavelength shift in the sensor FBG, the proposed demodulator uses the wavelength-dependent travel-length of the reflected light from a chirped fiber grating [103]. This method requires few other expensive optical components and the range of this demodulator is very limited (only up to 3000με). A multiplexed Bragg Grating Sensor Configuration utilizing Chirped Fiber Bragg Grating as interrogator was established [104]. This design is complicated and expensive as it employs Erbium doped fiber amplifier, RF generator, phase detector etc. In another complex FBG interrogation technique, a Chirped Fiber Grating based Sagnac Loop was introduced [105]. Though the resolution claimed is good (around ±5με), the strain measurement range is very limited (around ±250με). An interrogation technique using identical chirped FBG was proposed for strain sensing with a resolution of 5με [106]. In this technique, the strain measurement range could be as high as 15000-2000με, but it is not able to measure the compressive or negative strain.

Some of the FBG interrogation techniques presented so far can measure both the positive and negative strains, but they have at least one of the following issues; poor resolution, short measurement range or the system's performance being dependent on electrical components like, piezoelectric sensor/transducer. Also, most of these designs involve intricate experimental setup. Designs like, identical chirped FBG for interrogation [106] are simple and seem robust, but positive strain could be measured only. None of the designs offered so far seem to fulfil all the aspects. The sensor design presented in this chapter employs two pairs of wavelength shifted chirped FBGs (CFBGs). One pair of CFBGs measures strain and the other measures temperature. The spectra of both the pairs of CFBGs are kept apart (no overlapping)

from each other to avoid cross talking. This design is capable of measuring true strain (temperature independent) in both the positive and negative direction and also, the temperature at the same time. The response of this system is about 750pW/με (at input power of 2.5mW). A photodiode with a sensitivity of 0.3-0.4nW would very comfortably provide a strain resolution of less than 1με. Thus, this design is capable of providing a strain resolution of 1με. The resolution can be increased further just by taking these steps; by increasing the reflectivity of the CFBGs used and/or by increasing the power of the light source.

Since the information is interrogated in terms of change in the intensity of the output signal, this module can measure the frequency of fundamental modes of structures. Hence, dynamic test of FOPS can also be performed for global SHM by this sensor module. Thus, this cost effective and compact sensor module provides combined information of FGB and FOPS (local + global SHM).

7.2 Sensor design and technical details

The schematic diagram of the experiment is shown in the Figure 7.1. In the proposed sensor design, two pairs of wavelength shifted CFBGs are used. The first pair consists of CFBG1 & CFBG1' and second pair consists of CFBG2 & CFBG2' as shown in Figure 7.1. The reflectivity of these CFBGs is between 80-85%. CFBG1 & CFBG2 are working in reflection mode (sensing arms) and CFBG1' & CFBG2' are working in transmission mode as shown in Figure 7.1 (interrogation arms). In other words, CFBG1' & CFBG2' are acting as wavelength filters to CFBG1 & CFBG2, respectively. The transmission spectra of CFBG1 & CFBG1' are shown in Figure 7.2. Also, transmission spectra of CFBG2 & CFBG2' are shown in Figure 7.3. From Figure 7.2 it is clear that CFBG1 & CFBG1' are not identical and their spectra are shifted by about 1.7nm. Similarly, from Figure 7.3 it is clear that CFBG2 & CFBG2' are not identical and their spectra are shifted by about 0.4nm. From Figures 7.2 and 7.3 it can also be seen that both the pairs (CFBG1, CFBG1' and CFBG2, CFBG2') are completely in the different parts of the spectrum (i.e. non-overlapping region). A SLED light source is used in the experiment. The power of the SLED light source is variable. The spectrum of the SLED light source is shown in Figure 7.4. Two fiber couplers, one 2x2 (50:50) and another 1x2 (50:50), are also used as shown in Figure

7.1. The light intensities coming out of CFBG1' and CFBG2' were measured by photodiode1 and photodiode2, respectively.

In this sensor design, the first pair (CFBG1 & CFBG1') is used for strain measurement in both the directions (extensive and compressive) by bonding CFBG1 to the target point. Dynamic FOPS measurement is also done by the same pair of CFBGs. The second pair (CFBG2 & CFBG2') is used to measure the temperature of the target point. CFBG2 is kept free, but close to the CFBG1 so that it only picks up temperature not the strain.
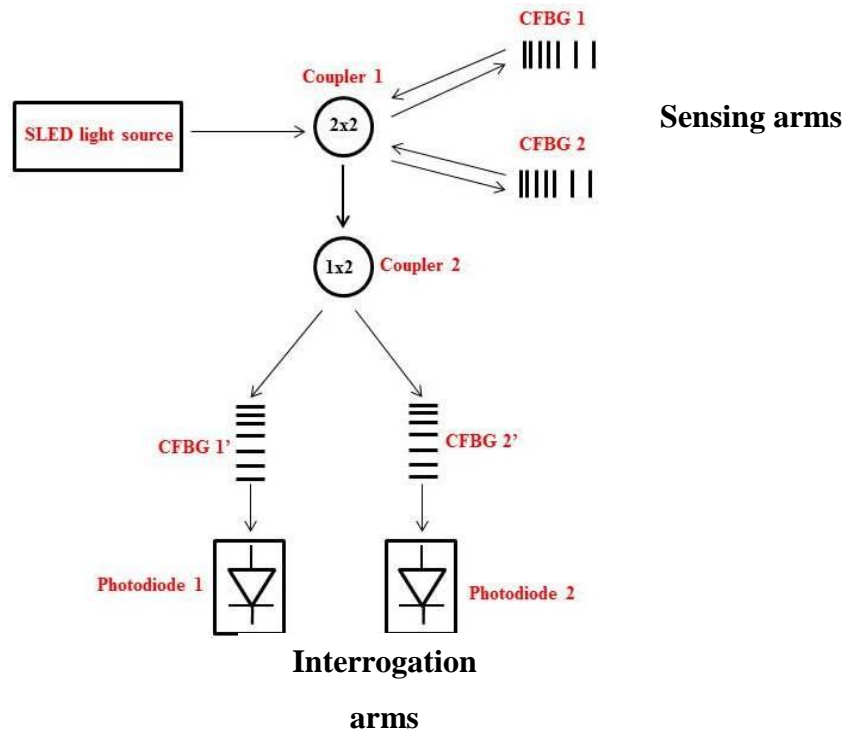
Figure 7.1: Schematic diagram of sensor design.
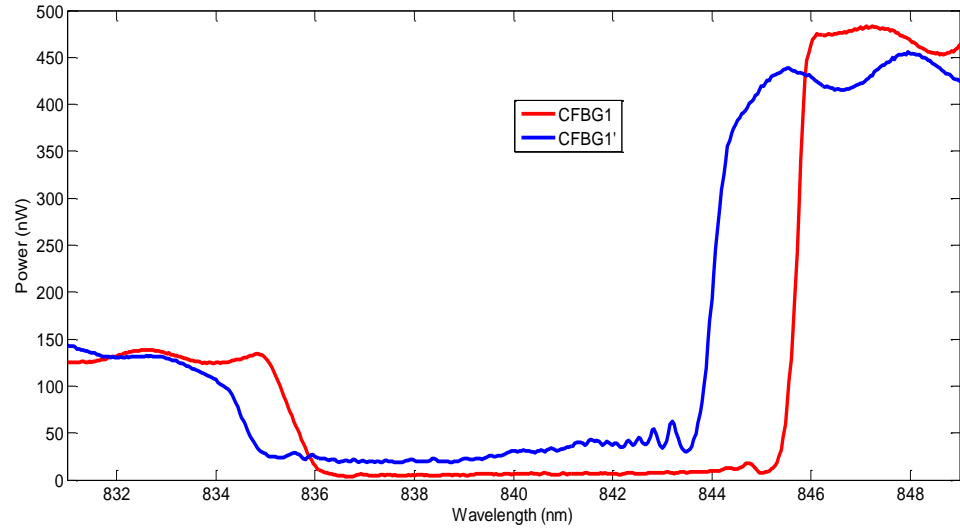
Figure 7.2: Transmission spectra of CFBG1 and CFBG1'.
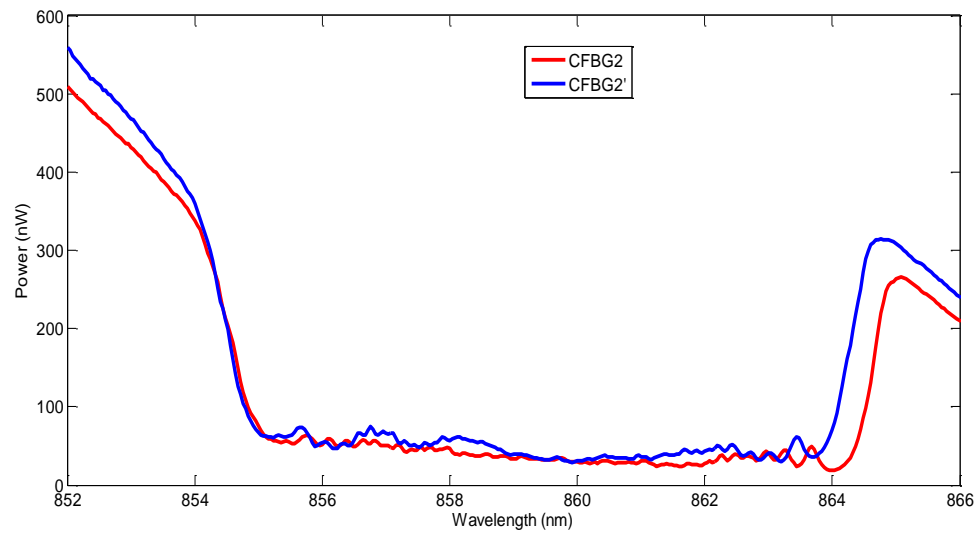
Figure 7.3: Transmission spectra of CFBG2 and CFBG2'.
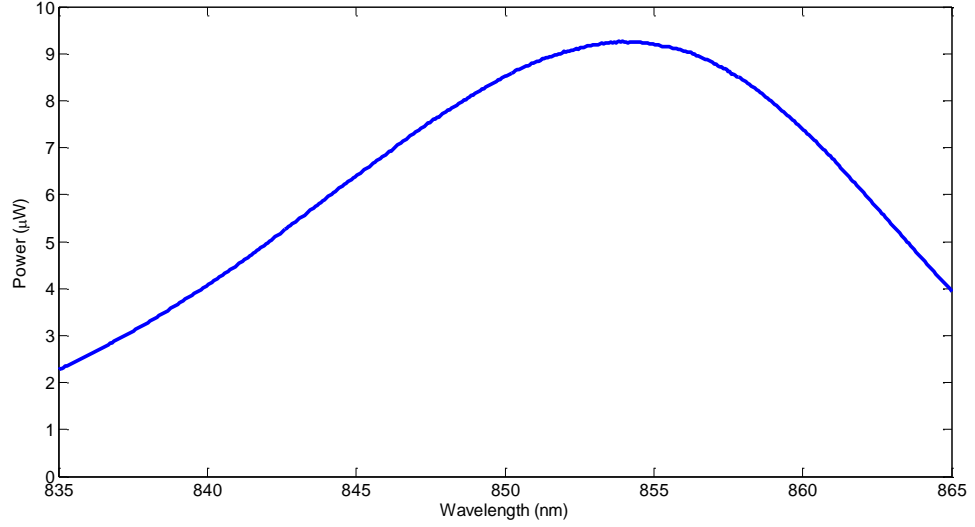
Figure 7.4: Spectrum of the SLED light source.

7.3 Principle

The light reflected by CFBG1 goes to the coupler 2 through the coupler 1 and there it gets divided into two parts which pass through both the interrogation arms (CFBG1' & CFBG2'). Since the spectrum of CFBG1 is far from the spectrum of CFBG2', the light reflected by CFBG1 goes through CFBG2' uninterruptedly. Therefore, if the strain is applied to CFBG1, the light intensity received at photodiode 2 does not change at all. On the other hand, when the light reflected by CFBG1 goes through CFBG1', it is blocked to a great extent. The non-overlapping region of the spectrum of CFBG1 only goes through CFBG1' and reaches the photodiode1. On the application of extensive (positive) strain on CFBG1, the spectrum of CFBG1 shifts right and therefore, the non-overlapping region increases. This results into the increase in the voltage measured by photodiode1. Similarly, when compressive (negative) strain is applied on CFBG1, the spectrum of CFBG1 shifts left resulting in the reduction of non-overlapping region. This will result into the decrease in the voltage measured by photodiode1.

Though the change in temperature will be sensed by both the pairs of CFBG, only second pair (CFBG2 & CFBG2') is used for temperature measurement at the target point. Only CFBG2' works as a wavelength filter for the light reflected by CFBG2. The non-overlapping region of the spectrum of CFBG2 only goes through CFBG2' and reaches the photodiode2. The rise or fall in the temperature moves the spectrum of

122

CFBG2 right or left respectively, resulting in increase or decrease the non-overlapping region. Subsequently, the voltage measured by the photodiode2 increases or decreases. The voltage measured by the photodiode1 will remain unaffected as the spectrum of CFBG1' is far from the spectrum of CFBG2.

Since temperature also shits the spectrum of CFBG1, combined effect of strain and temperature is obtained at photodiode1. The change in the voltage of both the photodiodes1&2 due to temperature variation can be correlated and then the temperature value can be subtracted/added accordingly from the combined value of photodiode1 to get the true strain value. Thus, this design gives true strain (extensive and compressive) and temperature at the same time. The range of strain measurement can be increased by increasing the default mismatch (or the distance between the centers of both the spectra) between the spectra of CFBG1 & CFBG1'. Similarly, the range of temperature measurement can be increased by increasing the default mismatch between the spectra of CFBG2 & CFBG2'.

7.4 Experiments and results

7.4.1 Strain measurement

As mentioned earlier, strain is measured using the first pair of CFBGs (CFBG1 & CFBG1'). CFBG1 was glued close to the fixed end of a cantilever as shown in the Figure 7.5. The size of the cantilever was 280X19X3.3mm^3. The power of SLED light source in this experiment was kept about 2.5mW.
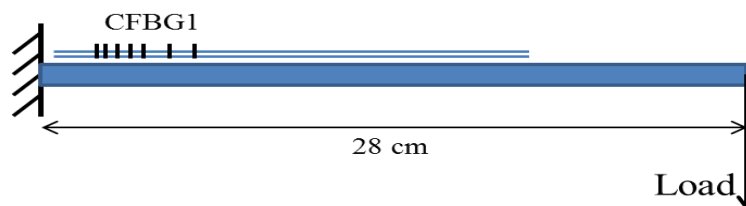
Figure 7.5: Cantilever experiment for strain measurement.

The cantilever is loaded at its free end as shown in the Figure 7.5. Since the CFBG1 is on the top side of the cantilever, it experiences extensional (positive) strain. Further, the cantilever was flipped upside down and loaded again in the same manner. This time CFBG1 being at the bottom of the cantilever experiences compressive (negative)

strain. The spectrum of light reflected by CFBG1 moves right or left on the application of positive and negative strain, resulting in an increase or decrease of non-overlapping area. The spectra of CFBG1 corresponding to different strain values are shown in Figure 7.6. The voltage measured by the photodiode1 is monitored continuously throughout this process. The positive and negative strains experienced by CFBG1 are plotted against the change in the voltage measured by the photodiode1 as shown in the Figure 7.7. From Figure 7.7 it is clear that strain vs voltage is almost linear. Thus, by looking at the change in the photodiode1's response, the strain values can be articulated.
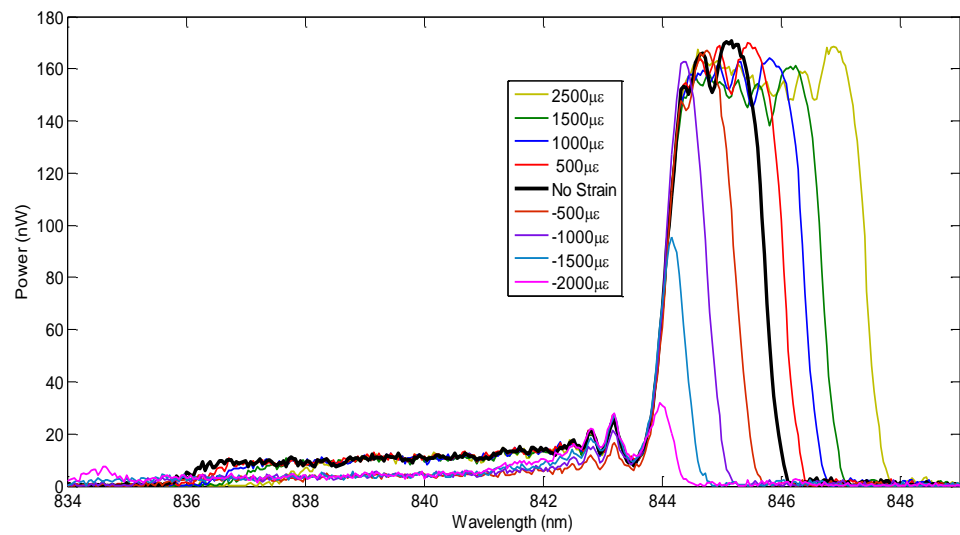
Figure 7.6: Spectra of CFBG1 at different strain values.
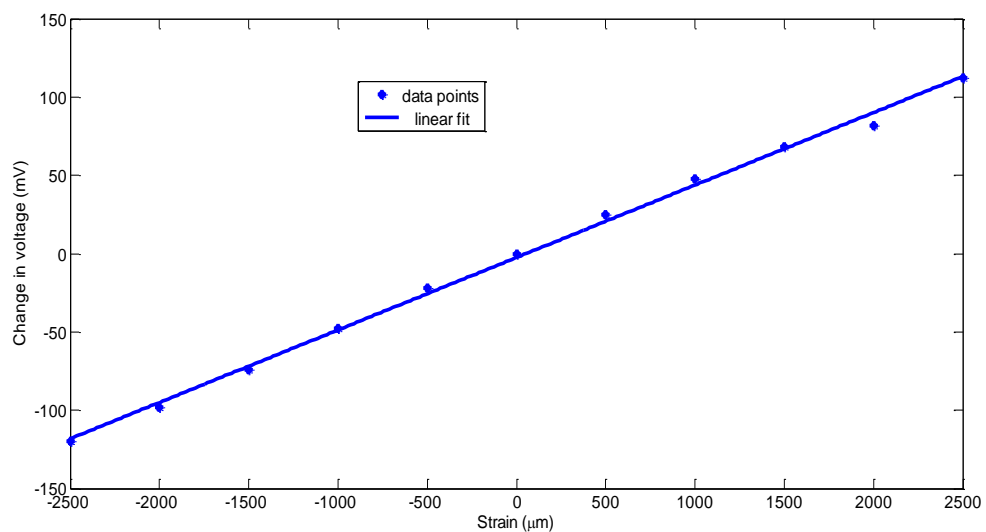
Figure 7.7: Strain vs change in voltage measured by photodiode1.

It has already been stated that the strain resolution of this sensing system can be increased either by increasing the reflectivity of the CFBGs used or by increasing the input power (the power of SLED light source). The strain vs voltage (measured by photodiode1) plots at various input powers is shown in the Figure 7.8. Upon increasing the input power from 1mW to 3mW, the strain resolution increases by a factor of 2.7. Again, if the input power is increased to 5mW, the resolution increases by a factor of 4.3. Thus, in conclusion the strain resolution of this sensing system can be adjusted to a desired value just by changing the input power.
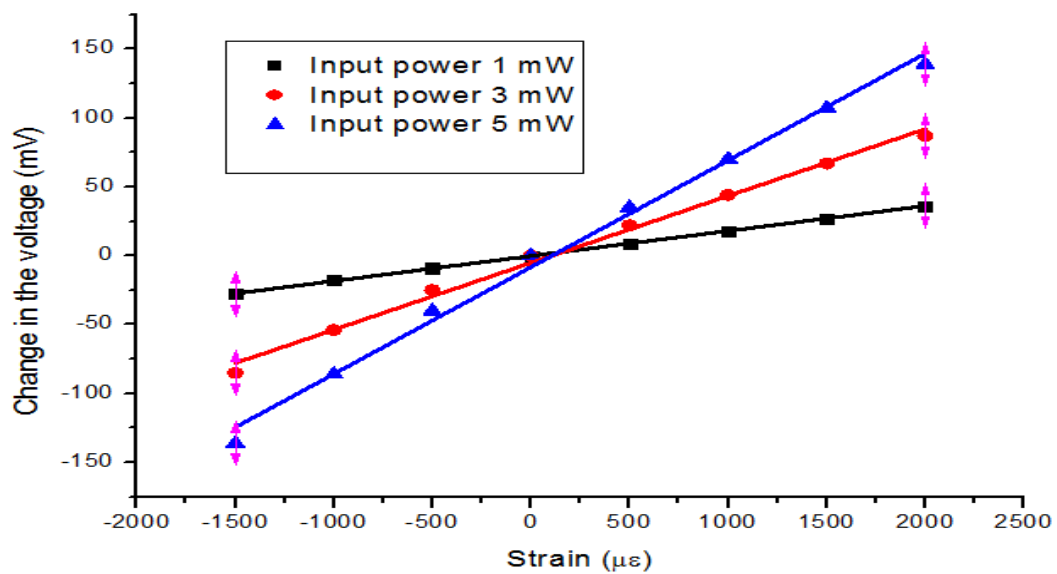
Figure 7.8: Strain vs voltage (measured by photodiode1) plots at various input powers.

7.4.2 Temperature measurement

Both the pairs of CFBGs behave exactly the same on rise or fall in temperature as both CFBG1 and CFBG2 are placed close to each other. However, only the second pair (CFBG2 & CFBG2') is used for temperature measurement. Both CFBG1 and CFBG2 are put close to each other in an oven to simulate a real condition. When the oven is turned on and the temperature rises from room temperature (25^oC) onwards, the spectra of both CFBG1 and CFBG2 shifts right. In this case, the voltage measured by both the photodiode1 and photodiode2 increase. The temperature was reduced below the room temperature to 10^oC by mixing the hot and cold water and putting CFBG1 and CFBG2 in that water. On lowering the temperature the spectra of both CFBG1 and CFBG2 shift left. In this case, the voltages measured by both the photodiode1 and

photodiode2 decrease. The spectra of CFBG2 reaching photodiode2 at different temperature values are shown in Figure 7.9. The temperature values and the change in the voltages measured by both photodiode1 and photodiode2 are plotted in Figure 7.10. It can be observed that both the graphs are almost linear.

In a practical situation where strain and temperature both might vary, photodiode1 gives the combined response, while on the other hand photodiode2 gives the temperature values only. In Figure 7.9, the voltage change (due to temperature) in photodiode2 can be correlated to the voltage change (due to temperature) in photodiode1. This value can then be subtracted or added accordingly to the voltage measured at photodiode1 to get the true strain value. Thus, second pair (CFBG2 & CFBG2') measures the temperature and works as a temperature compensator to pair 1 (CFBG1 & CFBG1').
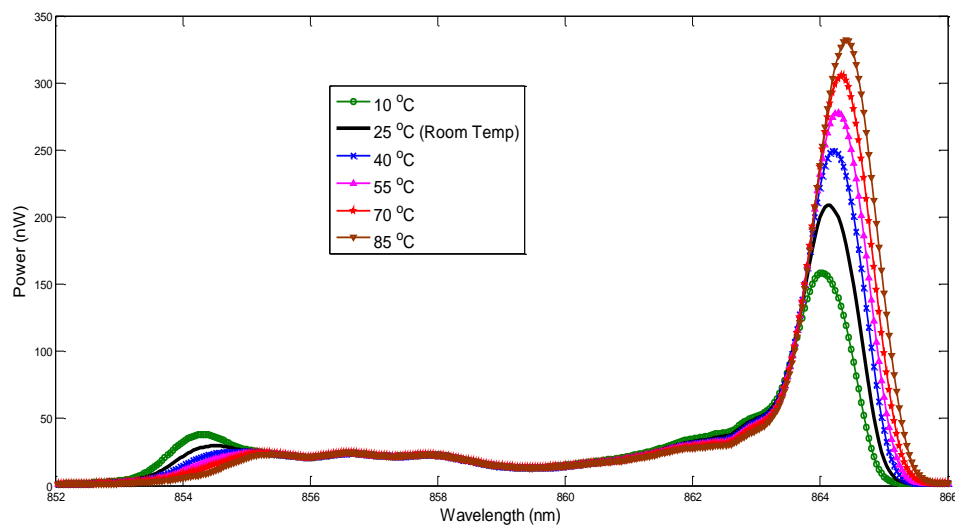
Figure 7.9: Spectra of CFBG1 at different temperature values.
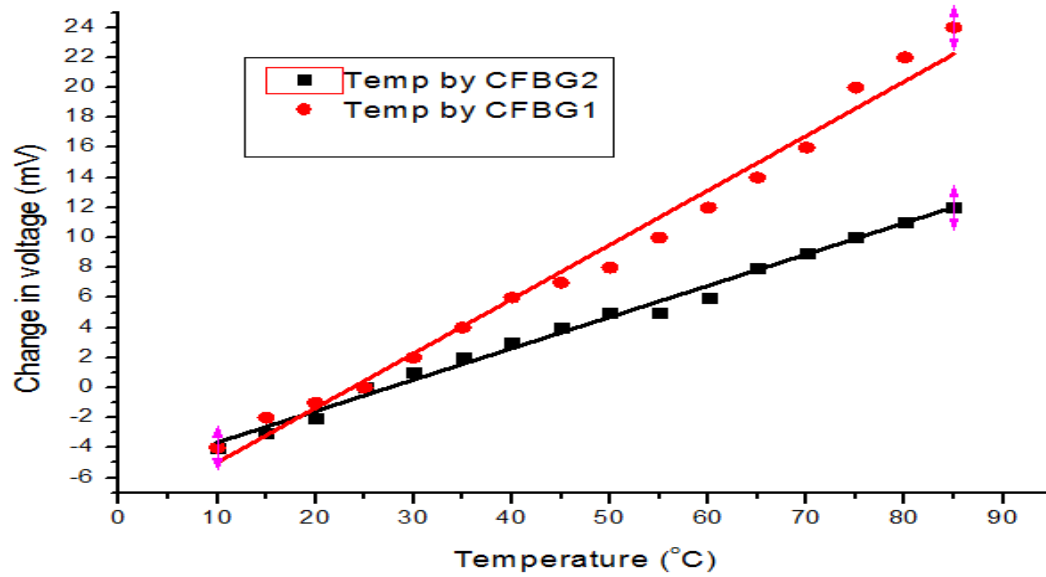
Figure 7.10: Temperature vs change in voltage measured by photodiode1 and photodiode2.

Temperature variation at the interrogation arms could be an issue as far as the application of this chirped FBG sensing module is concerned. The temperature variations at the interrogation arms might disturb the proper functioning of the CFBG sensing module. The interrogation arms should be kept away from the actual site (where the sensing arms are placed) of monitoring. To avoid this problem even further, the interrogation arms will have to be packaged in such a way that they can be made thermally isolated from their surroundings.

7.4.3 Damage monitoring by static and dynamic tests

The proposed CFBG sensor module was further used for damage monitoring in a cantilever beam by static and dynamic loading tests. The chirped grating CFBG1 was bonded to close to the fixed end of the cantilever as shown in the Figure 7.5. Cracks were made at different places in the beam as shown in the Figure 7.11.

7.4.3.1 Static loading test (FBG action)

The proposed sensor module was further used for damage monitoring in a cantilever beam. The chirped grating CFBG1 was bonded to close to the fixed end of the cantilever as shown in the Figure 7.5. Cracks were made at different places in the beam as shown in the Figure 7.11. The static loading test was performed for every crack scenario presented in Figure 7.11. The static load vs voltage measured by

photodiode1 plots, corresponding to every crack scenario, are shown in Figure 7.12. Clearly from Figure 7.12, the gradient of the line increases significantly only if the crack is close to CFBG leading to local SHM of the cantilever. This action can be attributed as normal FBG action.
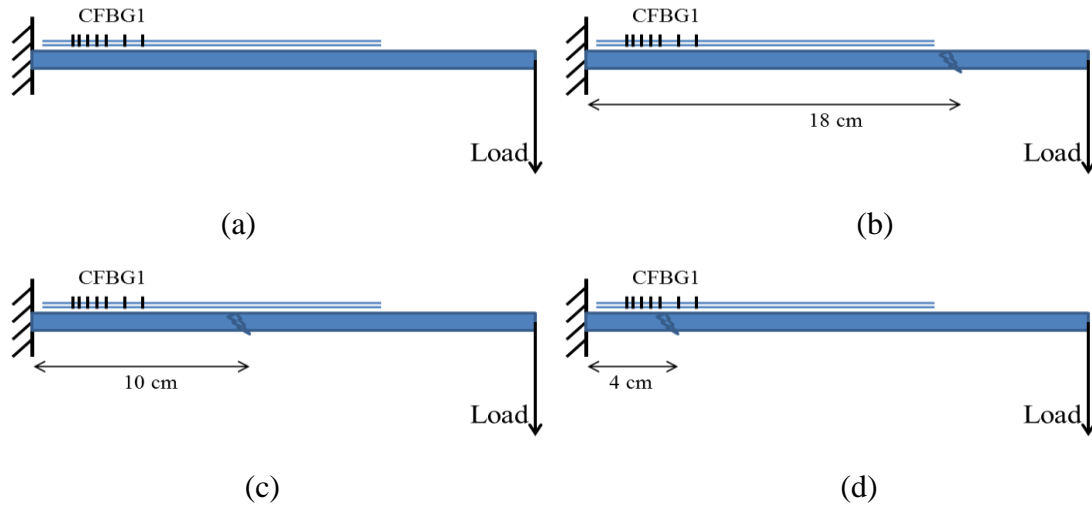
Figure 7.11: Different crack scenario in the cantilever beam.
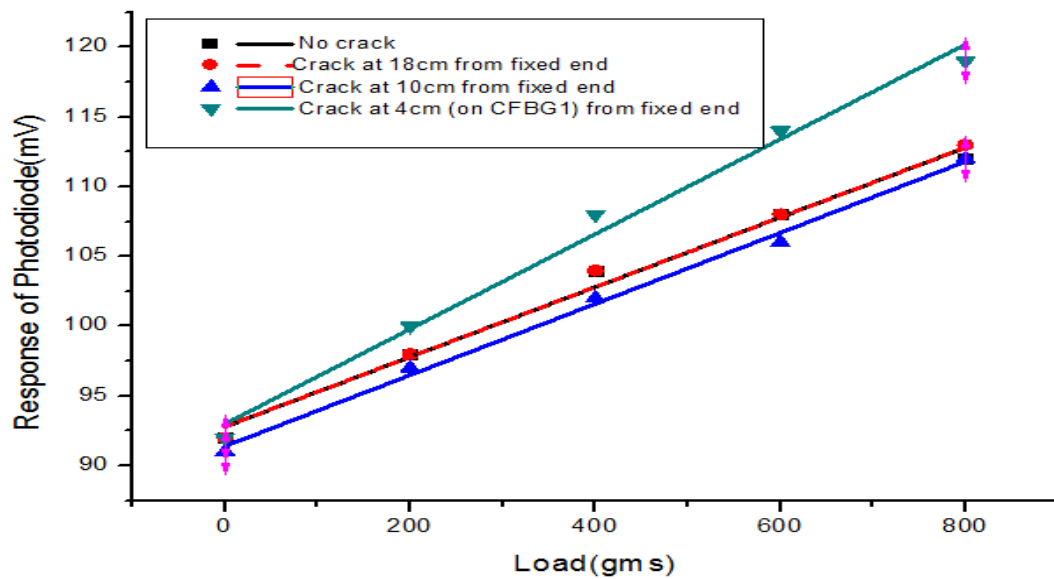
Figure 7.12: Load vs photodiode1 response for different crack scenarios presented in Figure 7.11.

7.4.3.2 Dynamic test (FOPS action)

This sensor module is intensity based. If the structure (cantilever in this case) vibrates with its fundamental frequency, it will create fluctuations in the signal of photodiode1

with the same frequency. The frequency of these fluctuations in the signal of photodiode1 can easily be read through an oscilloscope. The oscilloscope snapshots showing the first fundamental frequency and first harmonic of cantilever for different crack scenarios displayed in Figure 7.11 are presented Figure 7.13. The frequency decreases in every case because the stiffness decreases due to damage in the structures as established by equation (1.2). Such dynamic test is quantified in terms of a damage factor called dynamic damage factor (DDF) [35]. DDF is defined as

$$DDF = [\frac{(\omega_1)_{damaged}}{(\omega_1)_{undamaged}}]^2 \tag{7.1}$$

where $(\omega_1)_{undamaged}$ is the first fundamental frequency of undamaged cantilever and $(\omega_1)_{damaged}$ is the first fundamental frequency of damaged cantilever. Earlier this DDF was used to be calculated through fiber optic polarimetric sensor (FOPS). The DDF values for every crack case (Figure 7.11) are presented in table 7.1. Clearly, the value of DDF keeps reducing as the crack moves towards the fixed end of the cantilever because the stiffness of the cantilever increases as we move from the free end to the fixed end of a cantilever. Though this test may not tell the exact location of the damage, it indicates the presence of damage irrespective of the location of the damage unlike FBG. This leads to global SHM of the cantilever. Thus, this sensor module provides combined (FBG + FOPS) information.

(a)

(b)

(c)

(d)
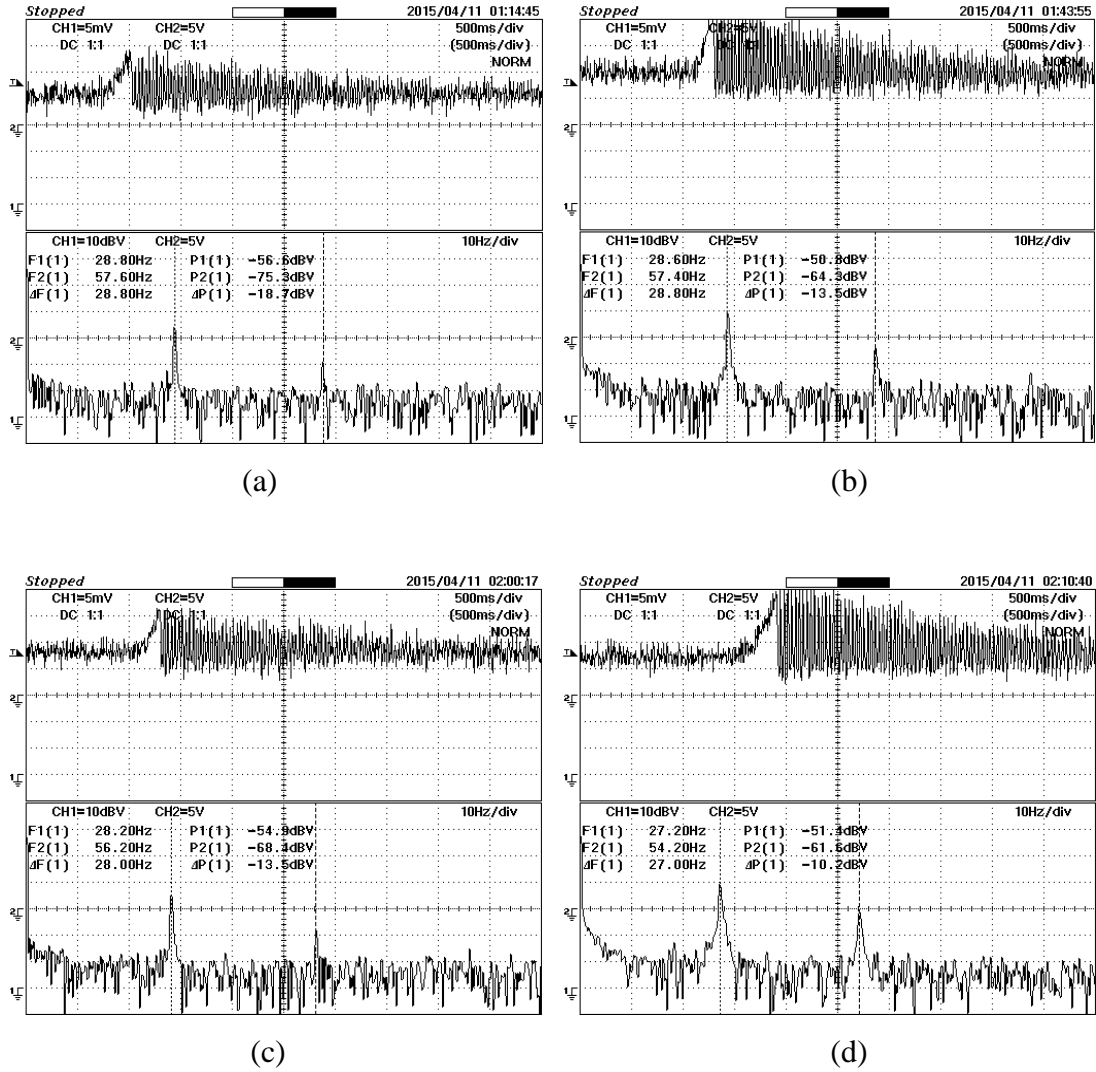
Figure 7.13: The oscilloscope snapshots showing the first fundamental frequency and first harmonic of cantilever for crack scenario presented in (a) Figure 7.11(a), (b) Figure 7.11(b), (c) Figure 7.11(c) and (d) Figure 7.11(d).

130

Table 7.1: DDF for different crack scenarios presented in Figure 7.11.

Crack scenario	F1 (Hz)	F2 (Hz)	Dynamic damage factor (DDF)
Figure 7.11(a) (No crack)	28.8	57.6	1
Figure 7.11(b)	28.6	57.2	0.986
Figure 7.11(c)	28.2	56.2	0.958
Figure 7.11(d)	27.2	54.2	0.892

7.5 Competence and commercial viability of the presented sensor module

FBGs have already been researched a lot in the last 2-3 decades. FBGs have been implemented as strain, temperature of pressure sensors for structural health monitoring of different civil and mechanical structures. Still the sentiment of the sensor market is little skeptical about the implementation of FBGs. The reasons for this sentiment are simply the cost and the bulkiness of the interrogation system, namely, optical spectrum analyzer (OSA). Few companies have managed to bring down the size of the system, but the cost is still very high and size is not as small as it should be for field applications.

This sensor module abrogates the need for OSA. It also allows the use of simple LEDs as light source. Altogether, this design substantially brings down the cost as it does not require OSA or any expensive light source. No bulky component has been used in this design, which makes it compact and lightweight. The sensor's strain resolution can be as good as 1με. Its strain measurement range could be as good as ±7000με or even more. Also, this sensor design is capable of measuring of strain and temperature simultaneously. Moreover, sensor module can additionally perform dynamic FOPS measurement, enabling it for global SHM of different structures. Thus, it provides FBG + FOPS information from a single system.

The photodiodes response can be easily transmitted wirelessly. Thus, it allows making the system Wi-Fi for remote sensing purposes. Sensor modules can be installed at several locations and response of each sensor module can be transmitted to a central reception unit which then transfers the signal to internet as shown in Figure 6.14. Thus, the signals from different sensor modules can be received at any point in the world. All these advantages of this sensor design make it suitable for the following applications:

1. Energy industry

Strain/temperature monitoring of different units in energy industry demands remote sensing capability. This sensor design would be the best for this purpose, because it has the capability of remote sensing. These target application areas may be blades of floating wind turbines, power generators, transformers etc.

2. Transportation industry

Strain monitoring of different parts of heavy vehicles is important. Some of the parts like, railway overhead contact line, railway pantographs, railway tracks etc. require an electromagnetically insulated sensing system. This design is independent of any electromagnetic interference and capable of performing structural health monitoring of these parts with high accuracy.

3. Aerospace industry

Every aircraft is monitored structurally by measuring the strain in its various parts. Wings, hulls etc. are some of the important parts to monitor. Dynamic FOPS measurement would be additional information on global health of these parts of an aircraft. Here in this case the sensors must have the quality of embedment. These sensors can be embedded during the manufacturing itself.

4. Civil structures

To avoid catastrophic failure of different civil structures like, tall building, bridges, flyovers etc., different structural health monitoring techniques are used. Usually, strain at crucial points of the structures is monitored. These sensors can provide a better

alternative to the conventional sensors. Moreover, structural vibrations can be monitored using dynamic FOPS aspect of this sensor module.

5. *Oil and gas industry*

Oil and gas industry is facing a challenge on how to monitor their pipelines. Since this sensor design has the potential to be wireless, it can provide a solution to their problem.
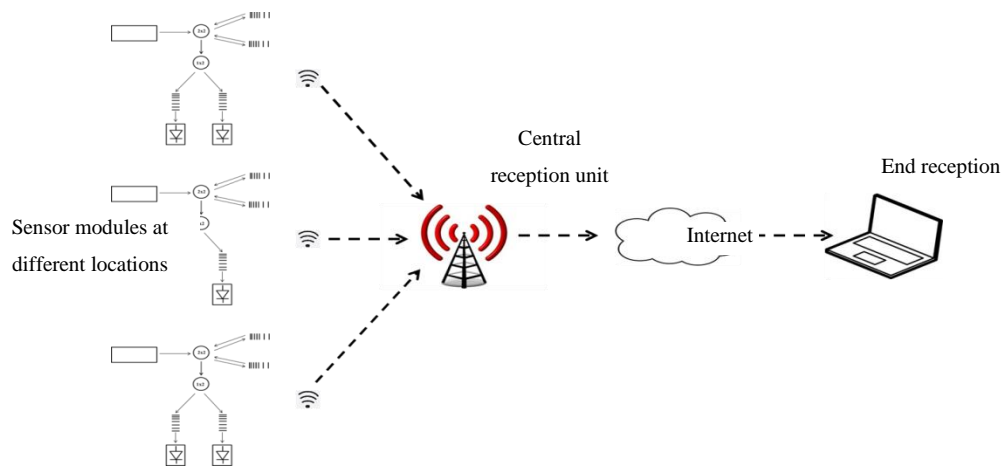
Figure 7.14: Wi-Fi scheme for signal transmission at a remote location.

CHAPTER 8 Conclusions and recommendations for future work

All the work that was done has been concluded in this chapter. The future work based on the experience of work done for this thesis has also been recommended.

8.1 Conclusions

In the literature review of this research thesis, different fiber optic sensors for structural health monitoring (SHM) of different mechanical and civil structures have been talked about. Among all the fiber optic sensors, fiber optic polarimetric sensor (FOPS) and fiber Bragg grating (FBG) sensors were chosen to be investigated further for SHM. These two fiber optic sensors (FOPS and FBG) were chosen out of the simplicity of their experimental setup, repeatability & accuracy in measurement and applicability as far as the SHM of different structures is concerned. FOPS provide important information for global SHM while FBG is suitable for local SHM. Only global or local SHM data is not enough to give a significant picture of the damage state in structures. Implementation of multiple fiber optic sensors to get sufficient information on SHM becomes very complicated and expensive. In this research thesis different ways are explored in which sufficient information on SHM of different mechanical and civil structures can be retrieved with minimum instrumental cost. The following contributions are made through my research presented in this thesis.

➢ Random fluctuations in the output signal of FOPS were one of the main concerns. A new design of FOPS is proposed whose output is very stable and SHM tests can be performed effectively and accurately. This design of FOPS is then implemented for dynamic test through frequency analysis of first and second fundamental modes of a cantilever beam to find out the actual damage state in the cantilever beam. This analysis was only qualitative in the past. Finally, it is proved that the detection of the location and size of a crack is possible with FOPS in cantilever shape structures like, wings of aircrafts, blades of wind turbine etc. Further, a frequency analysis of first fundamental mode of a Fixed-fixed beam is also presented. Although the results give important

information about the damage state in the fixed-fixed beam, the exact location of the cracks could not be found as the second fundamental mode could not be excited in the fixed-fixed beam.

➢ As per the literature available, FBGs can perform SHM of different structures by measuring strain, temperature or pressure in a very localized area of that structure around them. FBGs are completely unaware of the events happening at some distance. A concept is developed in which a spliced PM-FBG can be used for damage detection globally as well as locally. This concept incorporates the FOPS also. Thus this spliced PM-FBG method provides combined information of normal FBG system and FOPS system.

A sensor design based on this spliced PM-FBG concept is proposed for the SHM of one dimensional structures. This sensor design is demonstrated for SHM of aluminum beams. It is found that this design not only marks the presence of damage in the beam, but gives a very strong idea of damage location in the beam also. Thus, this design is capable of giving a very improved picture of the damage state in real one dimensional structures. Moreover, this design will work with every beam configuration as no boundary condition based mathematics is involved in the working of this sensor model. Simultaneous information about damage location and size is difficult to get with this method, but a high precision in damage location can be achieved with multiple PM-FBG splicing.

Further, the scope of the idea using PM-FBG for SHM has been extended to two dimensional structures. To demonstrate this, the proposed sensor design is implemented for SHM of aluminum plates. It is found that this sensor design is suitable for locating damages in two dimensional structures also. Again, since no boundary condition mathematics is involved in the working of this sensor design, it must work for all two dimensional structures with any configuration. This sensor configuration can be extended by multiplexing more PM-FBGs together to find damage locations in practical civil and mechanical structures.

➢ FBGs are already working as strain/temperature/pressure sensors for structural health monitoring of different civil and mechanical structures. Still the sentiment

of the sensor market is a little skeptical about the implementation of FBGs on a larger scale. The cost and the bulkiness of the interrogation systems (OSA) are the prime reasons for this. A wavelength shifted chirped FBG sensor module is developed in this research which abrogates the need for OSA. It also allows the use of simple LEDs as light source. The presented sensor module is compact, lightweight and very cost effective. The presented sensor modules measures strain and temperature simultaneously. Moreover, it performs dynamic FOPS measurement enabling it for global SHM of different structures. Thus, it provides local & global (FBG + FOPS) information on the damages in a structure.

➤ Sometimes pressure is equally important parameter to access the health of a structure. A cost effective special purpose FBG sensor with needle tubing is fabricated to measure pressure change in liquids. This special purpose FBG sensor is designed in such a way that it yields a sensitivity of $1.636 \times 10^{-2} MPa^{-1}$ which is higher than the sensitivity of any other FBG sensor design available for liquid pressure measurement. The reliability of the proposed FBG sensor is confirmed through repeated experiments. It is further used to measure the hydrostatic resin pressure at a certain point of a high temperature and low compaction pressure curing prepreg composite laminates. The numerical validation of the resin pressured measured by the proposed FBG sensor is also presented. Several such FBG sensors can be used simultaneously to measure the resin pressure at various locations to find out the resin pressure distribution across the entire curing laminate while it cures. The resin pressure measurement in a curing laminate is important to control the strength, stiffness and void nucleation in the cured composites. In other words, the SHM of curing composites can be performed using FBG sensors proposed in this work.

8.2 Recommendations for future work

The work done in this thesis has a great future scope. The following are the directions for the future work

➤ The proposed design of FOPS that is produced in this research work has only been implemented for cantilevers where first and second fundamental modes of

vibrations are excited. This leads to the knowledge of damage size and location in cantilevers. In case of a fixed-fixed beam second mode of vibration could not be excited and it leads to a very vague picture of damage in fixed-fixed beams. Exciting second mode of vibration in the fixed-fixed beam would give a very decisive picture of the damage state in fixed-fixed beams. Other beam structures like, simply supported beams should also be experimented with this new design of FOPS for damage size and location.

➢ The proposed FOPS sensor is sensitive only in the region of interest and signal can be carried to a remote location without jeopardizing the stability and purity of the signal. Thus, this FOPS sensor can be implemented for the SHM of real civil structures through static or dynamic tests from a remote location (say few hundred meters).

➢ The concept of spliced PM-FBG looks good in finding damage locations in one dimensional and two dimensional lab specimens. The real mechanical and civil structures are much bigger than the lab specimen; therefore, more PM-FBGs should be spliced together to make a large sensor network for these real structures. This spliced PM-FBG sensor network should be implemented in real structures to study damage location in them.

➢ The proposed wavelength shifted chirped FBG sensor module is a cost effective and compact system. It has high resolution and very good strain/temperature measurement range. The strain and temperature measurements are independent of each other. The photodiodes response can be easily transmitted wirelessly. Thus, it allows making the system Wi-Fi for remote sensing purposes. Sensor modules can be installed at several locations and response of each sensor module can be transmitted to a central reception unit which then transfers the signal to the internet. This whole scheme is depicted in Figure 8.1. This wireless sensor module will provide with reliable and low cost remote SHM, which important industries like, oil and gas, civil industry etc. are struggling with.
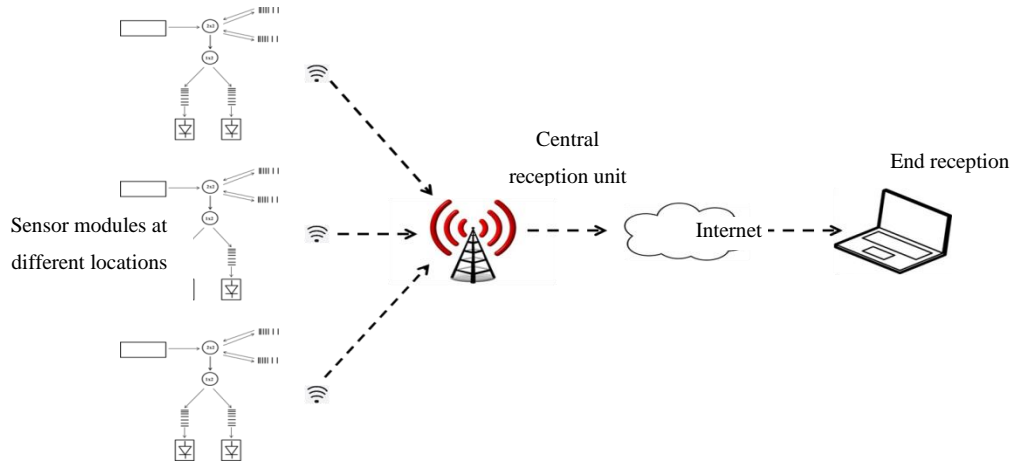
Figure 8.1: Wi-Fi scheme for signal transmission at a remote location.

➢ The special purpose FBG sensor is implemented to know the resin pressure of a curing composite at only one point. Resin pressure measurement at one point is not enough to create a map of resin pressure distribution across the entire curing laminate. Several such special purpose FBG sensors must be used at various locations in the curing laminate to achieve this.

➢ This special purpose FBG sensor is suitable for liquid pressure measurement at places where accessibility is difficult. Hence, this FBG sensor must be tested at sites like, geothermal wells, deep oil pipes etc.

List of Publications

Journal papers published:

1. **M. Maheshwari**, S. C. Tjin, W. W. Ching, and A. Asundi, "FBG and FOPS for local and global structural health monitoring on a single fiber", *Smart Materials and Structures* **24**(4), 1-11 (2015).

2. **M. Maheshwari**, S. C. Tjin, and A. Asundi, "Efficient design of Fiber Optic Polarimetric Sensors for crack location and sizing", *Optics & Laser Technology* **68**, 182-190 (2014).

3. **M. Maheshwari**, S. C. Tjin, and A. Asundi, "Damage investigation in beam structures using fiber optic polarimetric sensors", *Journal of Multifunctional Composites* **2**(1), (2014).

Journal papers under review:

1. **M. Maheshwari**, S. C. Tjin, W. W. Ching, and A. Asundi, "Combined FBG and FOPS on a single fiber for structural health monitoring of two-dimensional structures", Submitted in *Structural Health Monitring*.

2. **M. Maheshwari**, S. C. Tjin, and A. Asundi, "A chirped-FBG based FBG interrogation system for static and dynamic structural health monitoring", Submitted in *Smart Materials and Structures.*

3. **M. Maheshwari**, V. G. M. Annamdas, J. H. L. Pang, S. C. Tjin, and A. Asundi, "Crack monitoring using multiple smart materials; fiber optic sensors & piezo sensors", Submitted in *Smart Structures and Systems*.

4. A. S. Ganapathi, **M. Maheshwari**, S. C. Joshi, Z. Chen, A. Asundi, and S. C. Tjin, "In-situ measurement and numerical simulation of resin pressure during prepreg composite manufacturing", Submitted in *Measurements*.

Conference papers:

1. **M. Maheshwari**, V. G. M. Annamdas, J. H. L. Pang, S. C. Tjin and A. Asundi, "Fibre optic sensors for load-displacement measurements and comparisons to piezo sensor based electromechanical admittance signatures", *Proc. SPIE* **9437**, 1-12 (2015).

2. A. S. Ganapathi, **M. Maheshwari**, S. C. Joshi, Z. Chen, A. Asundi, S. C. Tjin, "Fibre Bragg grating sensors for in-situ measurement of resin pressure in curing composites", *Proc. SPIE* **9302** (2015).

3. V. Dikshit, O. L. Seng, **M. Maheshwari**, A. Asundi, "Failure assessment of aluminum liner based filament-wound hybrid riser subjected to internal hydrostatic pressure", *Proc. SPIE* **9302** (2015).

4. **M. Maheshwari**, A. K. Asundi, Swee Chuan Tjin, "Effect of the location and size of a single crack on first fundamental frequency of a cantilever beam using Fiber Optic Polarimetric sensors and characterisation of FBG sensors", *Proc. SPIE* **8793** (2013).

References

[1] T. Takagi, "A Concept of Intelligent Materials", Proc. U.S.-Japan Workshop on Smart/Intelligent Materials and Systems, 3-10 (1990).

[2] V. G. M. Annamdas and K. K. Annamdas, "Active and passive interaction mechanism of smart materials for health monitoring of engineering structures", Proc. SPIE **7292**, G1-G11 (2009).

[3] J. A. Fairweather, "Designing with Active Materials: An Impedance Based Approach", Ph.D. Thesis, Rensselaer Polytechnic Institute, New York, (1998).

[4] Y Yang, V. G. M. Annamdas, C. Wang and Y Zhou, "Application of multiplexed FBG and PZT impedance sensors for health monitoring of rocks", Sensors **8**(1), 271-289 (2008).

[5] S. Park, S. Ahmad, C. B. Yun, and Y. Roh, "Multiple Crack Detection of Concrete Structures Using Impedance-based Structural Health Monitoring Techniques", Experimental Mechanics **46**(5), 609-618 (2006).

[6] V. G. M. Annamdas, Y. Chew, J. H. L. Pang, H. J. Hoh, K. Zhou and B. Song, "Fatigue growth analysis of interacting and merging surface defects using PZT transducer based impedance method and digital image correlation system", Journal of Nondestructive Evaluation **33**(3), 413-426 (2014).

[7] M. Maheshwari, V. G. M. Annamdas, J. H. L. Pang, S. C. Tjin and A. Asundi, "Fibre optic sensors for load-displacement measurements and comparisons to piezo sensor based electromechanical admittance signatures", Proc. SPIE **9437**, 1-12 (2015).

[8] Harris, D. O. and H. L. Dunegan, "Continuous monitoring of fatigue-crack growth by acoustic-emission techniques", Experimental Mechanics **14**(2), 71-81 (1974).

[9] I. Colombo, I. G. Main and M. C. Forde, "Assessing Damage of Reinforced Concrete Beam Using "b-value" Analysis of Acoustic Emission Signals", Journal of Materials in Civil Engineering **15**(3), 280-286 (2003).

[10] Roberts, T. M. and M. Talebzadeh, "Acoustic emission monitoring of fatigue crack propagation", Journal of Constructional Steel Research **59**(6), 695-712 (2003).

[11] I. Bartoli, "Structural health monitoring by ultrasonic guided waves", Ph.D. Thesis, University of California, San Diego, (2007).

143

[12] A. Srivastava, and F. L. di Scalea, "Quantitative Structural Health Monitoring by Ultrasonic Guided Waves", Journal of Engineering Mechanics **136**(8), 937-944 (2010).

[13] Z. Wu, K. Liu, Y. Wang and Y. Zheng, "Validation and evaluation of damage identification using probability-based diagnostic imaging on a stiffened composite panel ", Journal of Intelligent Material Systems and Structures **26**(16), 2181-2195 (2015).

[14] X. P. Zhu, P. Rizzo, A. Marzani and J. Bruck, "Ultrasonic guided waves for nondestructive evaluation/structural health monitoring of trusses", Measurement Science and Technology **21**(4), 1-12 (2010).

[15] Eric Udd, Fibre Optic Sensors: An introduction for Engineers and Scientists, Wiley Series in Pure and Applied Optics, (1990).

[16] Eric Udd, Fibre Optic Smart Structures, Wiley Series in Pure and Applied Optics, (1995).

[17] D. A. Krohn, Fibre Optic Sensor: Fundamentals and Applications, Instruments Society of America, (1998).

[18] R. M. Measures, Structural Monitoring with fibre optic technology, Academic Press, (2001).

[19] K. T. Grattan and V. B. T. Meggitt, Optical Fibre Sensor Technology, Kluwer academic publishers, (1999).

[20] A Selvarajan and A Asundi, "Photonics fiber optics sensors and their applications in smart structures non-destructive evaluation", J. Non-Destr. Eval. **15**, 41–56 (1995).

[21] T. Yoshino, K. Kurosawa, K. Itoh and T. Ose, "Fiber-Optic Fabry-Perot Interferometer and its Sensor Applications", Microwave Theory and Techniques **30**(10), 1612-1621 (1982).

[22] K. A. Murphy, M. F. Gunther, A. M. Vengsarkar, and R. O. Claus, "Quadrature phase-shifted, extrinsic Fabry–Perot optical fiber sensors", Optics Letters **16**(4), 273-275 (1991).

[23] Y.J. Rao, "Recent progress in fiber-optic extrinsic Fabry–Perot interferometric sensors", Optical Fiber Technology **12**(3), 227-237 (2006).

[24] A. W. Domanski, T. R. Wolinski and W. J. Bock, "Polarimetric fiber optic sensors: state of the art and future", Proc. SPIE **2341,** (1994).

[25] Y. Verbandt, B. Verwilghen, P. Cloetens, L. V. Kempen, H. Thienpont, I. Veretennicoff, G. V. Vinckenroy, W. P. De Wilde and M. R. H. Voet, "Polarimetric

optical fiber sensors: aspects of sensitivity and practical implementation", Optical Review **4**(1), A75-A79 (1997).

[26] T. R. Woliński, "Polarimetric optical fibers and sensors", Progress in Optics. E. Wolf, Elsevier **40**, 1-75 (2000).

[27] D. S. Kwon and K. B. Lee, "Optical fiber curvature sensor for measuring body motion and its adhesive method", Google Patents (2005).

[28] H. Di, "Sensing principle of fiber-optic curvature sensor", Optics & Laser Technology **62**(0), 44-48 (2014).

[29] J. R. Guzman-Sepulveda, R. Dominguez-Cruz, J. J. Sánchez-Mondragón and D. A. May-Arrioja, "Curvature Sensor based on a Two-Core Optical Fiber", Conference on Lasers and Electro-Optics 2012, San Jose, California, Optical Society of America, (2012).

[30] W. Zhou, Y. Zhou, X. Dong, Li-Yang Shao, J. Cheng and J. Albert, "Fiber-Optic Curvature Sensor Based on Cladding-Mode Bragg Grating Excited by Fiber Multimode Interferometer", Photonics Journal IEEE **4**(3), 1051-1057 (2012).

[31] W. W. Morey, G. Meltz and W. H. Glenn, "Fiber Optic Bragg Grating Sensors", Proc. SPIE **1169**, 98-107 (1990).

[32] C. R. Giles, "Lightwave applications of fiber Bragg gratings", Lightwave Technology **15**(8), 1391-1404 (1997).

[33] A. Othonos, "Fiber Bragg gratings", Review of Scientific Instruments **68**(12), 4309-4341 (1997).

[34] R. Yun-Jiang, "In-fibre Bragg grating sensors", Measurement Science and Technology **8**(4), 355-375 (1997).

[35] J. Ma, and A. Asundi, "Structural health monitoring using a fiber optic polarimetric sensor and a fiber optic curvature sensor - static and dynamic test", Smart Materials and Structures **10**(2), 181-188 (2001).

[36] V. M. Murukeshan, P. Y. Chan, O. L. Seng and A. Asundi, "On-line health monitoring of smart composite structures using fiber polarimetric sensor", Smart Mater. Struct. **8**, 544–548 (1999).

[37] L. Kin-tak, Y. Libo, Z. Li-min, W. Jingshen and W. Chung-ho, "Strain monitoring in FRP laminates and concrete beams using FBG sensors", Composite Structures **51**, 9–20 (2001).

[38] R. A. Peura and J. G. Webster, Basic Sensors and Principles, Ch. 2, 45 (2008).

[39] B. Morten, G. De Cicco and M. Prudenziati, "Resonant pressure sensor based on piezoelectric properties of ferroelectric thick films", Sensors and Actuators A: Physical **31**(1–3), 153-158 (1992).

[40] J. J. Dosch, Daniel J. Inman and Ephrahim Garcia, "A Self-Sensing Piezoelectric Actuator for Collocated Control", Journal of Intelligent Material Systems and Structures **3**(1), 166-185 (1992).

[41] J. F. Tressler, S. Alkoyand R. E. Newnham, "Piezoelectric Sensors and Sensor Materials", Journal of Electroceramics **2**(4), 257-272 (1998).

[42] J. Sirohi and I. Chopra, "Fundamental Understanding of Piezoelectric Strain Sensors", Journal of Intelligent Material Systems and Structures **11**(4), 246-257 (2000).

[43] G. Gautschi, Piezoelectric Sensors, Piezoelectric Sensorics, Springer Berlin Heidelberg**,** 73-91 (2002).

[44] X. Zhao, H. Gao, G. Zhang, B. Ayhan, F. Yan, C. Kwan and J. L. Rose, "Active health monitoring of an aircraft wing with embedded piezoelectric sensor/actuator network: I. Defect detection, localization and growth monitoring", Smart Mater. Struct. **16**, 1208–1217 (2007).

[45] J. S. Sirkis, Interpretation of embedded optical fiber sensor signals. Applications of Optical Fiber Sensors in Engineering Mechanics, Am. Soc. Civ. Eng., 85–99 (1993).

[46] A. Asundi and P. J. Masalkar, "Fiber optic strain sensor, comparison of Hi-Bi fibers", Proc. SPIE **2574**, 119–22 (1995).

[47] T. Yoshino, "Fiber Fabry-Perot interferometers," in Proc. 3rd Int. Conf. on Integrated Optics and Optical Fiber Commun., San Francisco, CA, 1981.

[48] S. J. Petuchowski, T. G. Giallorenzi, and S. K. Sheem, "A sensitive fiber-optic Fabry-Perot interferometer", IEEE J. Quantum Electronics **17**, 2168-2170 (1981).

[49] J. S. Leng and A. Asundi, "Real time cure monitoring of smart composite materials using extrinsic Fabry–Perot interferometer and fiber Bragg grating sensors", Smart Mater. Struct. **11,** 249–255 (2002).

[50] J. S. Leng and A. Asundi, "Non-destructive evaluation of smart materials by using extrinsic Fabry-Perot interferometric and fiber Bragg grating sensors", NDT & E International **35**, 273-276 (2002).

[51] D. H. Kim, B. Y. Koo, C. G. Kim and C. S. Hong, "Damage detection of composite structures using a stabilized extrinsic Fabry–Perot interferometric sensor system", Smart Materials and Structures **13**(3), 593-598 (2004).

[52] E. J. Hearn, Mechanics of Materials vol 1, Oxford: Pergamon, ch 4, 57 (1982).

[53] C. Davis, A. Mazzolini, J. Mills and P. Dargaville, "A new sensor for monitoring chest wall motion during high frequency oscillatory ventilation", Med Eng Phys **21**, 619–23 (1999).

[54] C. Davis, A. Mazzolini and D. A. Murphy, "New fibre optic sensor for respiratory monitoring Australasian", Phys Eng Sci Med **20**, 214–9 (1997).

[55] N. Meir, B. Anatoly and T. Sergei, "Assessment of breathing effort by means of a fiber optic sensor", Proc. SPIE **2977**, 89–93 (1997).

[56] S. Silva, O. Frazão, J. Viegas, L. A. Ferreira, F. M. Araújo, F. X. Malcata and J. L. Santos, "Temperature and strain-independent curvature sensor based on a single mode/multimode fiber optic structure", Measurement Science and Technology **22**(8), 1-6 (2011).

[57] P. J. Masalkar, S. K. Malhotra, R. S. Sirohi and A. Asundi, "Use of optical fiber strain sensor for damage detection in composite structures", Proc. SPIE **2443**, 230–5 (1995).

[58] E. J. Hearn, Mechanics of Materials vol 1, Oxford: Pergamon ch 4, p 57 (1982).

[59] C. M. Harris and C. E. Crede, Shock and Vibration Hand Book 2nd edn, New York: McGraw-Hill, pp 7–12 (1976).

[60] W. J. Bock, T. R. Wolinski and A. Barwicz, "Development of a polarimetric optical fiber sensor for electronic measurement of high pressure", Instrumentation and Measurement, IEEE Transactions on **39**(5), 715-721 (1990).

[61] K. O. Hill, Y. Fujii, D. C. Johnson, and B. S. Kawasaki, "Photosensitivity in Optical Fibre Waveguides: Application to Reflection Filter Fabrication", Applied Physics Letters **32**, 647-649 (1978).

[62] G. Meltz, W. W. Morey, and W. H. Glenn, "Formation of Bragg Gratings in Optical Fibres by a Transverse Holographic Method", Optics Letters **14**(15), 823-825 (1989).

[63] R. Maaskant, A. T. Alaie, R. M. Measures, G. Tadros, S. H. Rizkalls and G. Thakurta, "A. Fibre-Optic Bragg Grating Sensors for Bridge Monitoring", Cement and Concrete Composites **19**, 21-33 (1997).

[64] M. D. Todd, G. A. Johnson and S. T. Vohra, "Deployment of Fibre Bragg Grating-Based Measurement System in a Structural Health Monitoring Application", Smart Materials and Structures **10**, 534-539 (2001).

[65] P. Moyo, J. M. W. Brownjohn, R. Suresh, and S. C. Tjin, "Development of Fibre Bragg Grating Sensors for Monitoring Civil Infrastructure", Engineering Structures **27**, 1828-1834 (2005).

[66] M. Maheshwari, A. K. Asundi and S. C. Tjin, "Effect of the location and size of a single crack on first fundamental frequency of a cantilever beam using Fiber Optic Polarimetric sensors and characterisation of FBG sensors", Proc. of SPIE **8793**, G1-G8, (2013).

[67] T. H. T. Chan, L. Yu, H. Y. Tam, Y. Q. Ni, S. Y. Liu, W. H. Chung and L. K. Cheng, "Fiber Bragg grating sensors for structural health monitoring of Tsing Ma Bridge: Background and experimental observation", Engineering Structures **28**, 648–659 (2006).

[68] L. K. Cheng, J. J. M. G. Schaarsberg and B. W. Oostdijk, "Multi-channel FBG sensor system for static and dynamic measurement up to 10 kHz", First European workshop on structural health monitoring, pp 560–7 (2004).

[69] M. P. Whelan, D. Albrecht and A. Capsoni, "Remote structural monitoring of the Cathedral of Como using an optical fiber Bragg sensor system", Proc SPIE **4694**, 1-11 (2002).

[70] L. Ren, G. Song, M. Conditt, P. C. Noble, and H. Li, "Fiber Bragg grating displacement sensor for movement measurement of tendons and ligaments", Applied Optics **46**(28), 6867-6871 (2007).

[71] L. Mohanty and S. C. Tjin, "Pressure mapping at orthopaedic joint interfaces with fiber Bragg gratings", Applied Physics Letters **88**, 1-3 (2006).

[72] L. Mohanty, S. C. Tjin, D. T. T. Lie, S. E. C. Panganiban and P. K. H. Chow, "Fiber grating sensor for pressure mapping during total knee arthroplasty", Sensors and Actuators A **135**, 323–328 (2007).

[73] J. R. Casas and P. J. S. Cruz, "Fiber Optic Sensors for Bridge Monitoring", Journal of Bridge Engineering **8** (6), 362-373 (2003).

[74] C. Leung and N. Elvin, ''Micromechanics based design of optical fiber crack sensor", Proc. Intelligent Civil Engineering Materials and Structures, 150–163 (1997).

[75] R. M. Measures, N. D. W. Glossop, J. Lymer, M. Leblanc, J. West, S. Duhois, W. Tsaw and R. C. Tennyson, "Structurally integrated fiber optic damage assessment system for composite materials", Appl. Opt. **28**, 2626–33 (1989).

[76] S. Timoshenko and J. N. Goodier, Theory of Elasticity. 2nd ed., New York: McGraw-Hill (1951).

[77] R. M. Silva, M. S. Ferreira and O. Frazao, "Temperature independent torsion sensor using a high-birefringent Sagnac loop interferometer", Optics Communications **285**(6), 1167-1170 (2011).

[78] D. Lesnik and D. Donlagic, "In-line, fiber-optic polarimetric twist/torsion sensor", Optics Letters **39**(9), 1494-1496 (2013).

[79] T. D. Cooper, "Specialist comments: applied point of view", Proc. AGARD **462**, R1.1–1.6 (1990).

[80] T. G. Chondros and A. D. Dimarogonas, "Identification of Cracks in Welded Joints of Complex Structures", Journal of Sound and Vibration **69**(4), 531-538 (1980).

[81] F. B. Sayyad and B. Kumar, "Approximate Analytical Method for Damage Detection in Beam", International Journal of Damage Mechanics **21**, 1064-1075 (2012).

[82] P. F. Rizos and N. Aspragathos, "Identification of Crack Location and Magnitude in a Cantilever Beam from the Vibration Modes", Journal of Sound and Vibration **138**(3), 381-388 (1990).

[83] T. Kortenski and T. Eftimov, "A Muller-Stokes description of polarization-mode transformation in uniformly perturbed optical fibers", Journal of Modern Optics **37**(9), 1413-1437 (1990).

[84] A. D. Dimarogonas, S. A. Paipetis and T. G. Chondros, Analytical Methods in Rotor Dynamics. 2nd ed., London: Springer (2013).

[85] R. M. Measures, Fiber optic strain sensing Fiber Optic Smart Structures, E Udd, New York: Wiley (1995).

[86] Y. Wang, S. C. Tjin, J. Z. Hao, T. K. Lim, B. K. Tan, K.M. Chan, J. M. W. Brownjohn, and P. Moyo, "Determination of stress-Strain characteristics of concrete slabs using embedded fiber Bragg grating sensors", SPIE Proc. **4073,** 297-304 (2000).

[87] S. C. Tjin, J. M. W. Brownjohn, Y. Wang and P. Moyo, "Structural performance monitoring with fiber Bragg grating sensor arrays", Conspectus Tech. Jour. Struct. Engg. Dept., 104-111 (2001).

[88] T. Guo, L. Shang, F. Liu, C. Wu, Bai-Ou Guan, Hwa-Yaw Tam and J. Albert, "Polarization-maintaining fiber-optic-grating vector vibroscope", Optics Letters **38**(4), 531-533 (2013).

[89] M. LeBlanc, S. T. Vohra, T. E. Tsai, E. J. Friebele, "Transverse load sensing by use of pi-phase-shifted fiber Bragg gratings", Optics Letters **24**(16), 1091-1093 (1999).

[90] F. Bosia, P. Giaccari, J. Botsis, M. Facchini, H. G. Limberger and R. P. Salathe, "Characterization of the response of fibre Bragg grating sensors subjected to a two-dimensional strain field", Smart Mater. and Structures **12**, 925-934 (2003).

[91] J. F. Botero-Cadavid, J. D. Causado-Buelvas and P. Torres, "Spectral Properties of Locally Pressed Fiber Bragg Gratings Written in Polarization Maintaining Fibers", Journal of Light Wave Tech. **28**(9), 1291-1297 (2010).

[92] C. Lawrence, D. Nelson and E. Udd, "Measurement of transverse strains with fiber Bragg gratings", Proc. of SPIE **3042**, 218–28 (1997).

[93] C. R. Farrar, G. Park, D. W. Allen and M. D. Todd, "Sensor Network Paradigms for Structural Health Monitoring", Journal of Structural Control and Health Monitoring **13**(1), 210-225 (2006).

[94] M. Sun, W. J. Staszewski, and R. N. Swamy, "Smart Sensing Technologies for Structural Health Monitoring of Civil Engineering Structures", Advances in Civil Engineering **2010**, 1-13 (2010).

[95] F. Farahi, D. J. Webb, J. D. C. Jones and D. A. Jackson, "Simultaneous measurement of strain and temperature: cross-sensitivity considerations", J. Lightwave Technol. **8**,138–42 (1990).

[96] G. B. Hocker, "Fibre-optic sensing of pressure and temperature", Appl. Opt. **18**, 1445-1448 (1979).

[97] M. G. Xu, H. Geiger and J. P. Dakin, "Optical in-fibre grating high pressure sensor", Electron. Lett. **29**, 398-9 (1993).

[98] M. A. Davis and A. D. Kersey, "Matched-filter interrogation technique for fibre Bragg grating arrays", Electronics Letters **31**(10), 822-823 (1995).

[99] A. D. Kersey, T. A. Berkoff and W. W. Morey, "Multiplexed fiber Bragg grating strain-sensor system with a fiber Fabry-Perot wavelength filter", Optics Letters **18**(16), 1370-72 (1993).

[100] S. M. Melle, K. Liu, and R. M. Measures, "A Passive Wavelength Demodulation System for Guided-Wave Bragg Grating Sensors", IEEE Photonics Technology Letters **4**(5), 516-18 (1992).

[101] R. W. Fallon, L. A. Everall, L. Zhang and I. Bennion, "Multiplestrain-sensor interrogation with an asymmetric grating", Conf. on Lasers and Electro-Optics, San Francisco, California, Technical digest **6**, 423-4 (1998).

[102] R. W. Fallon, L. Zhang, L. A. Everall, J. A. R. Williams and I. Bennion All-fibre optical sensing system: Bragg grating sensor interrogated by a long-period grating", Meas. Sci. Technol. **9**, 1969-73 (1998).

[103] Sungchul Kim, Seungwoo Kim, Jaejoong Kwon and Byoungho Lee, "Fiber Bragg Grating Strain Sensor Demodulator Using a Chirped Fiber Grating", IEEE Photonics Technology Letters **13**(8), 839-41 (2001).

[104] A. A. Chtcherbakov and P. L. Swart, "Chirped Fiber-Optic Bragg Grating Interrogator in a Multiplexed Bragg Grating Sensor Configuration", Journal of Lightwave Technology **22**(6), 1543-47 (2004).

[105] Donghui Zhao, Xuewen Shu, Yicheng Lai, Lin Zhang and Ian Bennion, "Fiber Bragg Grating Sensor Interrogation Using Chirped Fiber Grating-Based Sagnac Loop", IEEE Sensors Journal **3**(6), 734-38 (2003).

[106] R. W. Fallon, L. Zhang, A. Gloag and I. Bennion, "Identical broadband chirped grating interrogation technique for temperature and strain sensing", Electronics Letters **33**(8), 705-7 (1997).

[107] Hyun-Kyu Kang, Dong-Hoon Kang, Hyung-Joon Bang, Chang-Sun Hong and Chun-Gon Kim, "Cure monitoring of composite laminates using fiber optic sensors", Smart Materials and Structures **11**, 279-87 (2002).

[108] E Chehura, A. A. Skordos, C. C. Ye, S. W. James, I. K. Partridge, R. P. Tatam, "Strain development in curing epoxy resin and glass fiber/epoxy composites monitored by fiber Bragg grating sensors in birefringent optical fiber", Smart Materials and Structures **14**(2), 354-62 (2005).

[109] R. de Oliveira, S. Lavanchy, R. Chatton, D. Costantini, V. Michaud, R. Salathé, and J. A. E. Manson, "Experimental investigation of the effect of the mould thermal expansion on the development of internal stresses during carbon fiber composite processing", Composites Part A: Applied Science and Manufacturing **39**(7), 1083-90 (2008).

[110] A. M. Grande, L. Di Landro, P. Bettini, A. Baldi, G. Sala, "RTM process monitoring and strain acquisition by fiber optics", Procedia Engineering **10,** 3497-502 (2011).

[111] L. Khoun, Rd. Oliveira, V. Michaud, P. Hubert, "Investigation of process-induced strains development by fiber Bragg grating sensors in resin transfer moulded composites", Composites Part A: Applied Science and Manufacturing **42**(3), 274-82 (2011).

[112] S. Minakuchi, T. Umehara, K. Takagaki, Y. Ito, N. Takeda, "Life cycle monitoring and advanced quality assurance of L-shaped composite corner part using embedded fiber-optic sensor", Composites Part A: Applied Science and Manufacturing **48**, 153-61 (2013).

[113] E. Schmachtenberg, H. J. Schulte zur, J. Töpker, "Application of ultrasonics for the process control of Resin Transfer Moulding (RTM)", Polymer Testing **24**(3), 330-8 (2005).

[114] B. Yenilmez, E. Murat Sozer, "A grid of dielectric sensors to monitor mold filling and resin cure in resin transfer molding", Composites Part A: Applied Science and Manufacturing **40**(4), 476-89 (2009).

[115] S. T. Lim, Woo II Lee, "An analysis of the three-dimensional resin-transfer mold filling process", Composites Science and Technology **60**, 961-75 (2000).

[116] G. D Smith, Modelling and experimental issuese in the processing of composite laminates, Thesis (M. A. Sc.) University of British Columbia, Vanouver, Canada (1992).

[117] K. lynch, P. Hubert, A. Poursartip, "Use of a simple, inexpensive pressure sensor to measure hydrosatatic resin pressure during processing of composite laminates", Polymer composites **20**(4), 581-593 (1999).

[118] S. Hao-Jan, F. Ming-Yue, C. Tzu-Chiang, L. Wen-Fung, and Bor. Sheau-Shong, "A Lateral Pressure Sensor Using a Fiber Bragg Grating", IEEE Photonics Technology Letters **16**(4), 1146-8 (2004).

[119] K.Bremer, E. Lewis, G. Leen, B. Moss, S. Lochmann, I. Mueller, T. Reinsch, J. Schroetter, "Fiber Optic Pressure and Temperature Sensor for Geothermal Wells", IEEE Sensors 2010 Conference, Hilton Waikoloa Village Waikoloa, Kona HI, USA (2010).

[120] D. Sengupta, M. S. Shankar, P. S. Reddy, R. L. N. S. Prasad, K. Srimannarayana, "An FBG based hydrostatic pressure sensor for liquid level measurements", Proc. SPIE **8426**, 84260C (2012).

[121] D. Sengupta, P. Kishore, "Continuous liquid level monitoring sensor system using fiber Bragg grating", Optical Engineering **53**(1), 1-8 (2014).

[122] C. Xin, Y. Gu, M. Li, Y. Li, and Z. Zhang, "Online monitoring and analysis of resin pressure inside composite laminate during zero-bleeding autoclave process", Polymer Composites **32**(2), 314-23 (2011).

[123] F. C. Campbell, A. R. Mallow and C. E. Browning, "Porosity in carbon fiber composites: an overview of causes", J. Adv. Mater. **26**(4), 18-33 (1995).

[124] Y. Gu, Z. Zhang and M. Li, "Resin pressure measuring system for hot pressing of composites", Acta Mater. Compos. Sin. **24**(2), 23-27 (2007).

[125] W. Ecke, I. Latka, R. Willsch A. Reutlinger and R. Graue, "Fibre optic sensor network for spacecraft health monitoring", Measurement Science and Technology **12**(7), 974 (2001).

[126] H. Ohno, H. Naruse, M. Kihara, A. Shimada, "Industrial Applications of the BOTDR Optical Fiber Strain Sensor", Optical Fiber Technology **7**(1), 45-64 (2001).

Appendix A

Amplitude cycles of the fast component at different input polarization angle (θ)

The PM fiber (length l_1) is spliced to the PM-FBG at an angle of 45° as shown in the Figure A1. An angle of 45° between the principal axes of both the PM fiber and PM-FBG during splicing will cause uneven sinusoidal variation of peak amplitudes. l_1 is the length of the first section of the PM fiber and l_2 is the distance of the FBG from the splice point. In this case, the final modified Mueller Stokes matrix for the fast component received at the OSA can be written as the product of all the Mueller matrices corresponding to every action shown in Figure A1:

Figure A1: Cross sectional layout of a PM fiber spliced to a PM-FBG at an angle of 45°.

$$[S_{out}] = [M_{PM,l_1,ref}][R_{45}][M_{PM,l_2,ref.}][M_f][M_{PM,l_2}][R_{45}][M_{PM,l_1}][M_\theta][S_{in}] \quad (1)$$

where $[S_{in}]$ and $[S_{out}]$ are the Stokes vectors of the input and output light respectively. $[M_\theta]$ is the Mueller matrix of the light, linearly polarized at an angle θ from the fast axis of the PM fiber. $[M_{PM,l_1}]$ and $[M_{PM,l_2}]$ are the Mueller matrices which describe the change in the Stokes vector due to the propagation of light into the PM fiber of length l_1 and l_2 respectively. $[M_f]$ is to select the fast component. $[R_{45}]$ are the rotation matrix. Finally, $[M_{PM,l_1,ref}]$ and $[M_{PM,l_2,ref.}]$ are the matrices for the light reflected from the FBG, which travels the lengths l_1 and l_2 again.

$$\begin{bmatrix} S_0^{out} \\ S_1^{out} \\ S_2^{out} \\ S_3^{out} \end{bmatrix} = \begin{bmatrix} \frac{1}{2}\left[\begin{array}{c} \left(S_0^{in} + S_1^{in}cos2\theta + S_2^{in}sin2\theta\right) \\ -\{S_0^{in}sin2\theta + S_1^{in}cos2\theta.sin2\theta + S_2^{in}sin^2 2\theta\}cos\left(\frac{2\pi l_1}{l_b}\right) \end{array} \right] \\ 0 \\ \frac{1}{2}\left[\begin{array}{c} \left(S_0^{in} + S_1^{in}cos2\theta + S_2^{in}sin2\theta\right) \\ -\{S_0^{in}sin2\theta + S_1^{in}cos2\theta.sin2\theta + S_2^{in}sin^2 2\theta\}cos\left(\frac{2\pi l_1}{l_b}\right) \end{array} \right]cos\left(\frac{2\pi l_1}{l_b}\right) \\ -\frac{1}{2}\left[\begin{array}{c} \left(S_0^{in} + S_1^{in}cos2\theta + S_2^{in}sin2\theta\right) \\ -\{S_0^{in}sin2\theta + S_1^{in}cos2\theta.sin2\theta + S_2^{in}sin^2 2\theta\}cos\left(\frac{2\pi l_1}{l_b}\right) \end{array} \right]cos\left(\frac{2\pi l_1}{l_b}\right) \end{bmatrix} \quad (2)$$

From equation (2) it is clear that the intensity of the fast component varies sinusoidally with the strain produced in the first section (l_1) of the PM fiber. The amplitude of the intensity cycle (or SOP cycle) is determined by the input polarization angle (θ). The amplitude of the intensity cycle (or SOP cycle) changes with the change in θ as shown in the Figure A. However the period of the cycle is completely independent of θ. The period of the intensity cycle (or SOP cycle) reduces only when there is damage in this section of the PM fiber (Figure A2).
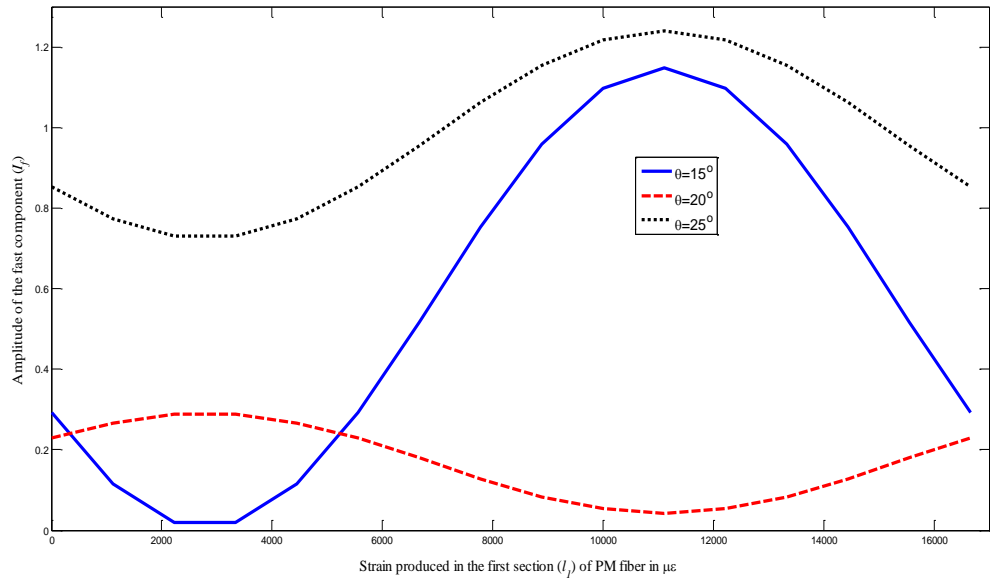

Figure A2: Amplitude cycles of the fast component at different input polarization angle (θ).